Dissertation

TECHNISCHE UNIVERSITÄT WIEN

Ion space-charge effects in multi-GEM detectors:

challenges and possible solutions for future applications

Zur Erlangung des akademischen Grades

Doktor der technischen Wissenschaften

unter der Leitung von

Ao.Univ.Prof. Dipl.-Ing. Dr.techn. Christina Streli

E141 - Atominstitut

eingereicht an der Fakultät für Physik

der Technischen Universität Wien

von

Dipl.-Ing. Patrik Thuiner

Matrikelnummer 0525388

247, Rue Lucie Aubrac
01630 Saint-Genis-Pouilly
France

und begutachtet von

Dipl.-Ing. Dr. Werner Riegler

CERN, European Organization for Nuclear Research, EP-AIO

<div style="text-align:center">

_____
Ao.Univ.Prof. Dipl.-Ing. Dr.techn.
Christina Streli

_____
Dipl.-Ing. Dr. Werner Riegler

</div>

Saint-Genis-Pouilly, 10. Oktober 2016

_____
Dipl.-Ing. Patrik Thuiner

Dissertation

Ion space-charge effects in multi-GEM detectors: challenges and possible solutions for future applications

submitted in partial fulfillment of the requirements for the degree of

Doktor der technischen Wissenschaften

under supervision of

Ao.Univ.Prof. Dipl.-Ing. Dr.techn. Christina Streli

E141 - Atominstitut

to the Faculty of Physics

at the Vienna University of Technology

by

Dipl.-Ing. Patrik Thuiner

Registration number 0525388

247, Rue Lucie Aubrac
01630 Saint-Genis-Pouilly
France

and reviewed by

Dipl.-Ing. Dr. Werner Riegler

CERN, European Organization for Nuclear Research, EP-AIO

<div style="display:flex;">

Ao.Univ.Prof. Dipl.-Ing. Dr.techn.
Christina Streli

Dipl.-Ing. Dr. Werner Riegler

</div>

Saint-Genis-Pouilly, 10. October 2016

Dipl.-Ing. Patrik Thuiner

Abstract

Gaseous Electron Multiplier (GEM) detectors are well known both for stable operation under irradiation with high particle fluxes and high achievable effective gains. The aim of this thesis is two-fold: to investigate the limits of GEM detector operation due to space-charge effects, and to develop a means to reduce the magnitude of the observed effects and thus extend those limitations.

The first part of the thesis presents a comprehensive study of the intrinsic limits of triple-GEM detectors under exposure to very high fluxes of soft X-rays or operation at very large effective gains. The behaviour of the effective gain, ion back-flow and the pulse-height spectra is explained in terms of the movement and accumulation of positive ions throughout the detector volume, resulting in distortions of the transfer and amplification fields. Numerical computations, and measurements on double-stage and single-stage detectors confirm the model describing the observed effects. Discussions on ways to extend the limits of gaseous detectors conclude the first part.

In the second part of the thesis the use of graphene to eliminate the ion back-flow into the conversion volumes of gaseous detectors is investigated. Graphene is a single layer of carbon atoms arranged in a honeycomb lattice, with a reported strong asymmetry in transmission of low energetic electrons and ions. The techniques to achieve graphene layers, freely suspended in holes of several tens of micrometres diameter, are described, as well as the methods to measure the charge transfer properties through the graphene samples. Results on the electron and ion transparency of graphene in gaseous detectors are presented, with special attention to the challenges arising from detects in the graphene layers. Discussions on ways to improve the layer quality and an outlook on further studies are found at the end of this work.

Kurzfassung

Gas-Elektronen-Verfielfacher-Detektoren (*engl.* Gaseous Electron Multiplier, GEM) können selbst während der Bestrahlung mit hohen Teilchenflüssen und mit hoher Signalverstärkung stabil betrieben werden. Mit dieser Arbeit werden zwei Ziele verfolgt: die operativen Limitierungen der Detektoren durch Raumladungseffekte wurden untersucht, sowie Möglichkeiten entwickelt, um das Ausmaß dieser Effekte zu reduzieren und damit diese Limitierungen zu erhöhen.

Der erste Teil der Arbeit befasst sich mit einer ausführlichen Studie über die operativen Limitierungen von Triple-GEM-Detektoren unter Bestrahlung mit hohen Flüssen weicher Röntgenstrahlung oder im Betrieb mit hoher Signalverstärkung. Das Verhalten der effektiven Signalverstärkung, des Ionen-Rückflusses und der Impulshöhenspektren wird durch die Bewegung und Ansammlung positiver Ionen im Detektorvolumen erklärt, welches zu einer Verzerrung der Transfer- und Verstärkungsfelder führt. Numerische Berechnungen sowie Messungen an einstufigen und zweistufigen Detektoren bestätigen die Modellierung der beobachteten Effekte. Eine Diskussion über verschiedene Möglichkeiten, um diese Limitierungen zu umgehen, schließt den ersten Teil der Arbeit ab.

Im zweiten Teil der Arbeit wird die Verwendung von Graphen zur Unterdrückung des Ionenrückflusses in gasgefüllten Detektoren untersucht. Graphen besteht aus einer monoatomaren Lage von Kohlenstoffatomen, die in einer wabenförmigen Struktur angeordnet sind. Eine starke Asymmetrie im Transport von Elektronen und Ionen durch Graphen wurde bereits in zahlreichen Publikation nachgewiesen. Es werden Techniken zur Produktion der in Löchern von mehreren zehn Mikrometern Durchmesser aufgespannten Schichten aus freitragendem Graphen vorgestellt, sowie Methoden zur Messungen der Transporteigenschaften von Elektronen und Ionen durch die Graphenproben erläutert. Die erzielten Resultate werden mit Augenmerk auf die Probleme durch Mikrofrakturen in den Graphenproben präsentiert. Diskussionen über Möglichkeiten zur Verbesserung der Probenqualität und ein Ausblick auf weitere Studien finden sich am Ende der Arbeit.

iv

Results of this thesis were presented at

P. Thuiner et al., Charge transfer properties through graphene layers in gas detectors, RD51 mini week, 16 - 19 June 2014, CERN, Geneva, Switzerland

P. Thuiner et al., Update on Charge Transfer Properties Through Graphene Layers in Gas Detectors, International Workshop on Advanced Detectors (IWAD) and the 14th RD51 Collaboration Meeting, 27 - 31 October 2014, Kolkata, India

P. Thuiner et al., Charge transfer properties through graphene layers in gas detectors, IEEE Nuclear Science Symposium and Medical Imaging Conference (NSS/MIC), 8 - 15 November 2014, Seattle, WA, USA

S. Franchino et al., Charge transfer properties through graphene for applications in gaseous detectors, 13th Pisa Meeting on Advanced Detectors, 24 - 30 May, La Biodola, Isola d'Elba, Italy - *presented by F. Resnati*

F. Resnati et al., Effects of High Charge Densities in Multi-GEM Detectors, IEEE Nuclear Science Symposium and Medical Imaging Conference (NSS/MIC), 1 - 6 November 2015, San Diego, CA, USA - *presented by F. Resnati*

S. Franchino et al., Effects of High Charge Densities in Multi-GEM Detectors, 4th International Conference on Micro Pattern Gaseous Detectors, 12 - 14 October 2015, Trieste, Italy

S. Franchino etl al., Charge Transfer Properties Through Graphene for Applications in Gaseous Detectors , 4th International Conference on Micro Pattern Gaseous Detectors, 12 - 14 October 2015, Trieste, Italy - *presented by F. Resnati*

P. Thuiner et al., Ion space-charge effects in multi-GEM detectors: challenges and possible solutions for future applications, 14th Vienna Conference on Instrumentation, 15 - 19 February 2016, Vienna, Austria

P. Thuiner, Graphene in MPGDs, MPGD Applications Beyond Fundamental Science Workshop and the 18th RD51 Collaboration Meeting, 12 - 16 September 2016, Aveiro, Portugal

P. Thuiner, Charge transfer properties through graphene for applications in gaseous detectors, AIME Nanotechnology & High-energy physics - From Material to Innovation, 20 - 21 Oct 2016, Darmstadt, Germany

and were partly published in

P. Thuiner et al., Charge transfer properties through graphene layers in gas detectors, Nuclear Science Symposium and Medical Imaging Conference (NSS/MIC), 2014 IEEE

vi

S. Franchino et al., Charge transfer properties through graphene for applications in gaseous detectors, Nucl. Instr. Meth. A, 824 (2016) 571-574

P. Thuiner et al., Multi-GEM Detectors in High Particle Fluxes, EPJ Web of Conferences, accepted for publication

Contents

Glossary

CVD	Chemical vapour deposition
DL	Double layer graphene
IBF	Ion back-flow
GEM	Gaseous Electron Multiplier
gGEM	GEM with graphene layer(s) on top or bottom electrode
MSGC	Micro-Strip Gas Counter
MPGD	Micro Pattern Gaseous Detector
MWPC	Multi-Wire Proportional Counter
PCB	Printed Circuit Board
PMMA	Polymethyl methacrylate
SEM	Scanning Electron Microscope
SL	Single layer graphene
SWPC	Single-Wire Proportional Counter
TEM	Transfer Electron Microscope
TL	Triple layer grapehe
TL*	Damaged triple layer graphene
TPC	Time Projection Chamber

Chapter 1

Interaction of particles with matter

This chapter gives an overview of the interaction of charged particles or highly energetic photons with matter. The detection of particles and the charge transport through the detector volume are explained in chapter 2. Section 1.1 describes the physical effects involved when charged particles traverse the gas-filled detector volume. In section 1.2 the interaction of photons with the detection medium are explained.

The section summarizes the relevant theory needed for this thesis found for example in [1], [2] or [3]. Further sources are explicitly cited.

1.1 Interaction of charged particles with matter

When a charged particle traverses the detector, interactions with the atoms or molecules of the detector volume can lead to primary charges being released within the detector. While all types of interaction between the charged particle and the medium occur in gaseous detectors, the contributions from, e.g. strong or weak interactions are negligible compared to the electromagnetic interaction. Coulomb interactions lead to either excitation or ionization, resulting in a track or cluster of primary charge, as will be discussed in section 1.1.2.

1.1.1 Energy loss and the Bethe-Bloch-Formula

Charged particles lose their energy in a large number of discrete interactions with the detection medium. While both charged and uncharged particles lose their energy by interaction with matter when passing through it, for charged particles the linear stopping power $S(E) = -dE/dx$ is defined as the loss of energy E per unit length dx due to excitation and ionization.

The average differential energy loss per unit length is described by the *Bethe* formula

$$-\frac{dE}{dx} = \frac{4\pi e^4 z^2}{m_0 v^2} NZ \left[\ln \frac{2m_0 v^2}{I} - \ln\left(1 - \beta^2\right) - \beta^2 \right] \tag{1.1}$$

where e and m_e are the electron charge and rest mass, c is the speed of light and $\beta = v/c$. The incoming primary particle has a velocity v and charge ze. The absorbing atoms have an atomic number Z and its number density N is given by $N = \rho_m N_A / M$ defined by its mass density ρ_m, the Avogadro constant N_A and molar mass M. I is the mean excitation ionization potential of the absorber, which is determined empirically. A good approximation is $I = I_0 Z$, with $I_0 \approx 12\,\text{eV}$. Values for typical gas mixtures used can be found in table 1.1. Formula 1.1 is only valid for charged particles with a velocity significantly larger than the one of the orbiting electrons in the absorbing atoms. At low and very high particle velocities corrections to 1.1 need to be taken into account.

1.1.2   Primary and total ionization

When the charged particle traverses the detector volume, a number of ionizing interactions take place, resulting in the creation of *primary* electron-ion pairs. The electrons ejected from the shell of the interacting atom or molecule can sometimes hold enough energy to surpass the ionisation potentials of further elements in the gas mixture, thus creating further electron-ion pairs before their energy is fully absorbed. These additionally created electrons are called *secondary* electrons. The total ionization is calculated by adding the number of primary electrons and secondary electrons created by the traversing charged particle. To do so, the average energy W_i to produce an electron-ion pair in the gas mixture used is needed. Example values of W_i for commonly used gases are given in table 1.1. For molecules and gas mixtures average values of W_i have to be calculated. The total number of primary electrons created is $n_t = \Delta E / W_i$, with the energy ΔE of the particle.

Gas	Z	A	δ (g/cm^3)	I_0 (eV)	W_i (eV)	$1/\rho \cdot dE/dx$ (MeV/g cm^{-2})	dE/dx (keV/cm)	n_p (cm^{-1})	n_t (cm^{-1})
H_2	2	2	8.38×10^{-5}	15.4	37	4.03	0.34	5.2	9.2
He	2	4	1.66×10^{-4}	24.6	41	1.94	0.32	5.9	7.8
N_2	14	28	1.17×10^{-3}	15.5	35	1.68	1.96	(10)	56
O_2	16	32	1.33×10^{-3}	12.2	31	1.69	2.26	22	73
Ne	10	20.2	8.39×10^{-4}	21.6	36	1.68	1.41	12	39
Ar	18	39.9	1.66×10^{-3}	15.8	26	1.47	2.44	29.4	94
Kr	36	83.8	3.49×10^{-3}	14.0	24	1.32	4.60	(22)	192
Xe	54	131.3	5.49×10^{-3}	12.1	22	1.23	6.76	44	307
CO_2	22	44	1.86×10^{-3}	13.7	33	1.62	3.01	(34)	91
CH_4	10	16	6.7×10^{-4}	13.1	28	2.21	1.48	16	53
C_4H_10	34	58	2.42×10^{-3}	10.8	23	1.86	4.50	(46)	195

Table 1.1: Properties of several gases used in proportional counters: atomic number Z, atomic weight A, density ρ, mean excitation potential I_0, average energy W_i to produce an eletron-ion pair, energy loss E/dx, and number of primary and total electron-ion pairs n_p and n_t per unit length. Energy loss $\Delta E/dx$, and numbers of electron-ion pairs are given at atmospheric pressure for minimum ionizing particles. Values of n_p shown in brackets are estimated from the linear dependence of n_p on the atomic number Z. Table modified from [1].

1.2 Interaction of photons with matter

Contrary to the interaction of charged particles with matter, which deposit their energy gradually through continuous interactions with many absorber atoms and are slowed down in the process, photons deposit their energy fully or partly to an electron of an absorber atom and are either fully absorbed or scattered under a significantly changed angle. Consequently, the deposited energy is usually well localized within the detector volume. Photons interact with matter in a number of processes, of which three are commonly used for the detection of particles: photoelectric absorption (section 1.2.1), Compton scattering (section 1.2.2) and pair production (section 1.2.3).
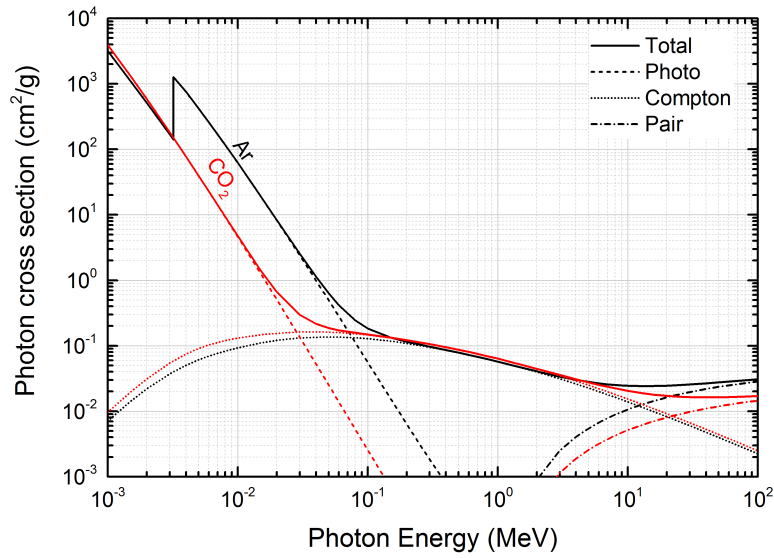

Figure 1.1: Photon cross sections for Ar and CO_2 [4].

The dominance of the effect involved is defined by the energy of the incident photon and the absorbing medium. Figure 1.1 shows the energy-dependent cross sections for argon and carbon dioxide. For argon, at energies smaller than $100 \, \text{keV}$ the photoelectric effect dominates, for energies larger than $10 \, \text{MeV}$ pair production has the highest influence, and in the intermediate energy range Compton scattering is the dominant effect.

Mono-energetic photons get absorbed by a uniform layer of material with thickness x following the *Beer-Lambert law*

$$I = I_0 e^{-\mu \rho x} = I_0 e^{-\alpha x} \; , \tag{1.2}$$

with the photon fluxes I_0 and I before and after interaction within the layer, the mass attenuation coefficient μ, and the density of the material ρ, or the linear absorption coefficient $\alpha = \mu \rho$. Knowing the absorption coefficient allows the calculation of the mean free path λ between interactions as

$$\lambda = \frac{1}{\mu \rho} \; . \tag{1.3}$$
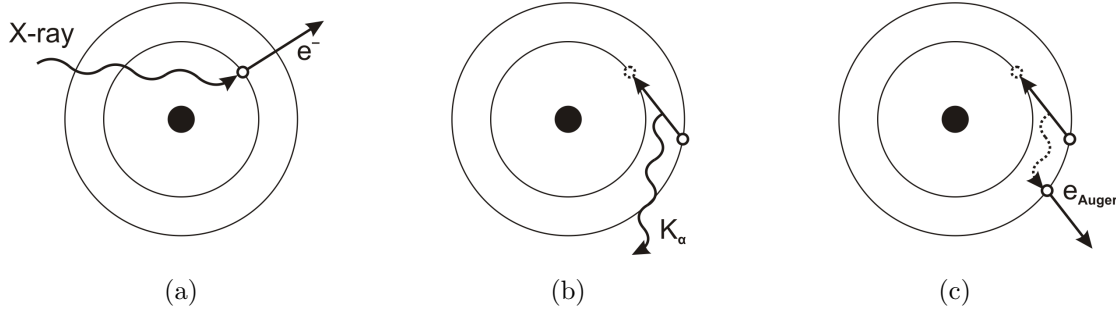
1.2.1   The photoelectric effect

Figure 1.2: Absorption of X-ray by an electron in a shell (a), followed either by emission of a fluorescence X-ray (b) or the emission of an Auger-electron (c).

In the photoelectric effect an incoming photon is fully absorbed during the interaction with the target atom. The photoelectric effect can only occur with bound electrons of an atom, not with a single free electron. A photo-electron with an energy of

$$E_e = h\nu - E_b \tag{1.4}$$

is released from the shell of the atom (figure 1.2 (a)), which equals the energy of the incoming photon $h\nu$ reduced by the binding energy of the electron E_b. The vacancy left by the emitted photo-electron is quickly filled with an electron from a higher shell. In this process the excess energy of the re-arrangement is emitted as a fluorescence photon (figure 1.2 (b)). The effect can lead to a cascade of re-arrangements and photon emissions. The photons are then usually absorbed close to the initial interaction point through photoelectric absorption by less tightly bound electrons of neighbouring atoms. A competing effect to the emission of fluorescence photons is the Auger effect, in which the transition energy of the electron filling the vacancy is transferred to a weaker bound electron of the same atom, which is emitted from its shell (figure 1.2 (c)).
For the Fe-55 sources with an energy of 5.9 keV and the Cu X-ray tube with an energy of 8 keV used within the scope of this thesis the photoelectric effect dominates. As can be seen in figure 1.3 (a) the cross section for photon absorption is depending on the gas used.

For small detectors (as compared to the mean free path of the fluorescence photons) or events taking place close to the surface of the detector there is a probability of some of the photons escaping the detector volume. As an example for an argon-filled detector, the incoming 5.9 keV photon of an Fe-55 source will mostly be absorbed by an electron from the K-shell (96%) or the L-shell (less than 4%). The L-shell absorption leads to the release of a 5.6 keV photo-electron and a characteristic X-ray with 0.3 keV energy. The K-shell absorption on the other hand always yields a photo-electron with an energy of 2.7 keV, followed by either
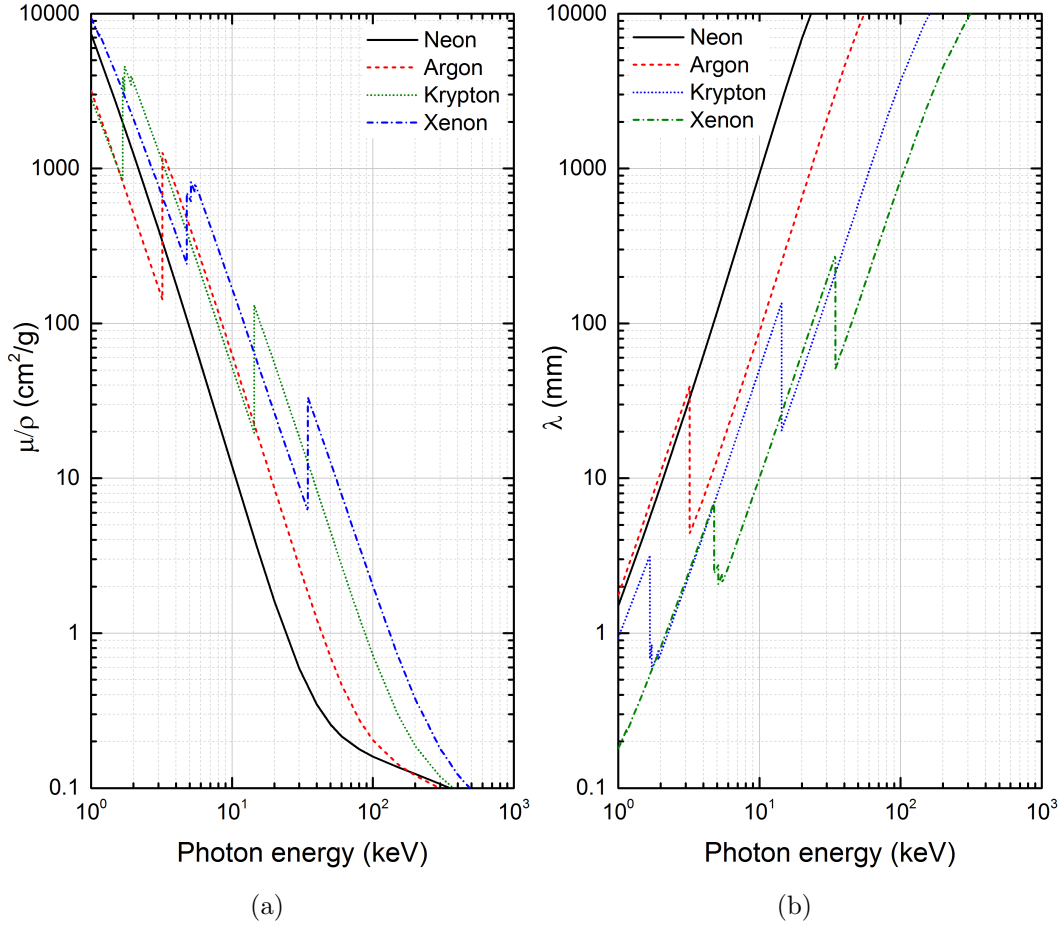
Figure 1.3: Absorption coefficients depending on the photon energy for different gases (a) [5], and mean free path for absorption of photons in the same gases at standard temperature and pressure (b) calculated with (1.3).

an additional (Auger) electron of $3.2\,\mathrm{keV}$ or the emission of characteristic X-rays. An X-ray with an energy of $0.3\,\mathrm{keV}$ as a result of the re-arrangement between the M and L shells is fully confined within the detector volume. The fluorescence X-ray of an electron moving from the L to the K shell has an energy of $2.9\,\mathrm{keV}$ and a mean free path of about $20\,\mathrm{cm}$ in argon at $1\,\mathrm{bar}$ (figure 1.3(b)). It therefore escapes common detectors such as the ones used within this thesis, resulting in the appearance of a second peak at reduced energy.

1.2.2 Compton scattering

The process of Compton scattering is one occurring between the incident photon and an electron of the absorbing material. As shown in figure 1.4 the incoming photon is scattered on the electron, transferring parts of its energy to the electron and subsequently deviating
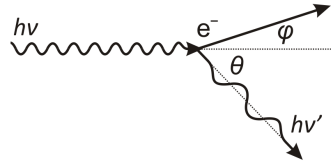
Figure 1.4: Compton effect

from its original angle by an angle θ, leading to a reduced energy of

$$h\nu' = \frac{h\nu}{1 + h\nu\left(1 - cos\theta\right)/(m_0c^2)} \, , \tag{1.5}$$

with m_0 being the rest-mass of the electron. The interacting *recoil* electron is scattered under the angle ϕ and left with an energy of

$$E_e = h\nu - h\nu' \, . \tag{1.6}$$

As can be seen in 1.5 the transferred energy depends on the scattering angle θ. For a forward scattering at $\theta = 0°$ no energy is transferred, and for the photon being back-scattered at $\theta = 180°$ most but not all of the energy is transferred. Independent of the scattering angle, there is always a transfer of less than 100% of the photon's energy onto the electron. Every other angle yields a percentage of energy transferred between those two extremes [6]. The angular distribution of the scattered photons for a differential scattering cross section is given by the *Klein-Nishina-formula*

$$\frac{d\sigma}{d\Omega} = Zr_0^2 \left(\frac{1}{1 + \alpha(1 - cos\theta)}\right)^2 \left(\frac{1 + cos^2\theta}{2}\right) \left(1 + \frac{\alpha^2(1 - cos\theta)^2}{(1 + cos^2\theta)[1 + \alpha(1 - cos\alpha)]}\right) \tag{1.7}$$

with $\alpha = h\nu/(m_0c^2)$ and the classical electron radius r_0.

1.2.3   Pair production
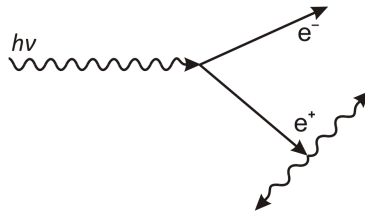
Figure 1.5: Electron-positron pair production

Once the photon energy exceeds twice the rest mass $m_0c = 511\,keV$ of an electron, pair production might occur. For the energies in the range of keV used within this thesis this

process is not possible, as can be seen in figure 1.1, but is included here nonetheless for sake of completeness.

The photon interacting with the coulomb field of the target atom's nucleus disappears and an electron-positron pair appears. The energy of the photon is converted into the kinetic energies and masses of the electron and positron. Two photons are usually emitted shortly after the pair production process due to the positron being annihilated within the medium. A depiction of the process can be seen in figure 1.5.

Chapter 2

Gaseous Detectors

This chapter discusses the transport and amplification of charge within gaseous detectors. The transport of the primary ionization charge in an applied electric field is described in section 2.1. The amplification of the charge is described in section 2.2. The theoretical framework of these sections is mostly taken from [1] and [2], with additional references cited in specific paragraphs. A short history of gaseous detectors and early micro-pattern gaseous detectors in section 2.3 leads to the introduction of the Gaseous Electron Multiplier in section 2.4. A short introduction to field focussing effects, and collection and extraction efficiencies, necessary for understanding the effects in chapters 3 and 4, is found in sections 2.5.4 and onward. A more comprehensive view on gaseous detectors can be found in [1] and [2], with current trends for Gaseous Electron Multipliers additionally reviewed in [7].

2.1 Charge transport

The secondary electrons created as a result of the primary ionisation rapidly loose their energy during multiple collisions with the molecules of the gas mixture. As a result they reach thermal equilibrium with the gas and therefore behave as described in the kinetic gas theory. In absence of external electric or magnetic fields the probability to find an electron or ion with a certain energy E is given by the *Maxwell-Boltzmann law*:

$$F(E) = 2\sqrt{\frac{E}{\pi(kT)^3}} e^{-\frac{E}{kT}} \ ,$$
(2.1)

with the Boltzmann constant k and temperature T, yielding a velocity distribution of

$$F(v) = 4\pi \sqrt[3]{\frac{m}{2\pi kT}} v^2 e^{-\frac{mv^2}{2kT}} \ ,$$
(2.2)

for different particle masses m. While for light noble gases the mean velocity is already of the order 10^4 cm/s, due to their smaller mass the velocity of electrons is about 10^7 cm/s.

2.1.1 Drift

In presence of an electric field, both electrons and ions move along the field lines, with the ions moving in the direction of the field vector, and the electrons moving in opposite direction.

The ions slowly move along the direction of field lines with a certain drift velocity

$$w^+ = \mu E \tag{2.3}$$

which is linearly proportional to the electric field up to very high values of E. The ion mobility μ for each species of ions is dependent on the gas mixture used within the detector and not depending on the field E. The ion mobility μ_i of an ion G_i^+ in a mixture of gases $G_1, G_2, \ldots, G_N$ is described by *Blanc's law*

$$\frac{1}{\mu_i} = \sum_{j=1}^{n} \frac{p_j}{\mu_{ij}} \ , \tag{2.4}$$

with the volume concentration p_j of the gas j and the ion mobility μ_{ij} for the ion G_i^+ in the pure gas G_j.
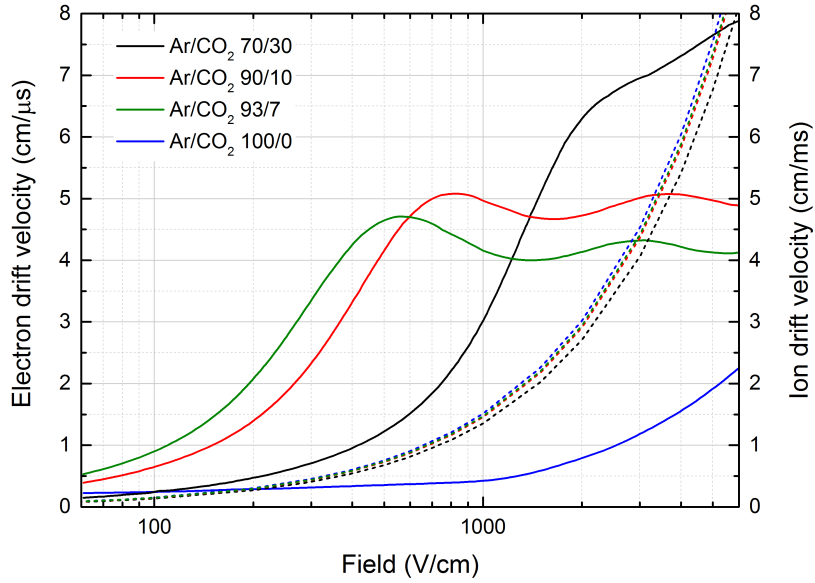
Figure 2.1: Dependence of drift velocities on the electric field for different Ar/CO_2 gas mixtures. Solid lines show electron velocities [8]. Dashed lines depict ion velocities calculated with (2.3) with ion mobilities from [9].

While the mobility of ions in a given gas mixture is constant, the one of electrons is strongly dependent on the applied field. The electrons lose energy between collisions with gas molecules, but due to their small mass their velocity can be considerably increased before the next collision. This leads to a non-linear behaviour of the electron drift velocity, which

can be described by

$$w^- = k\frac{eE}{m}\tau \ ,$$

(2.5)

with the mean time τ between collisions. Examples for electron drift velocities in different gas mixtures and at different fields are shown in figure 2.1.
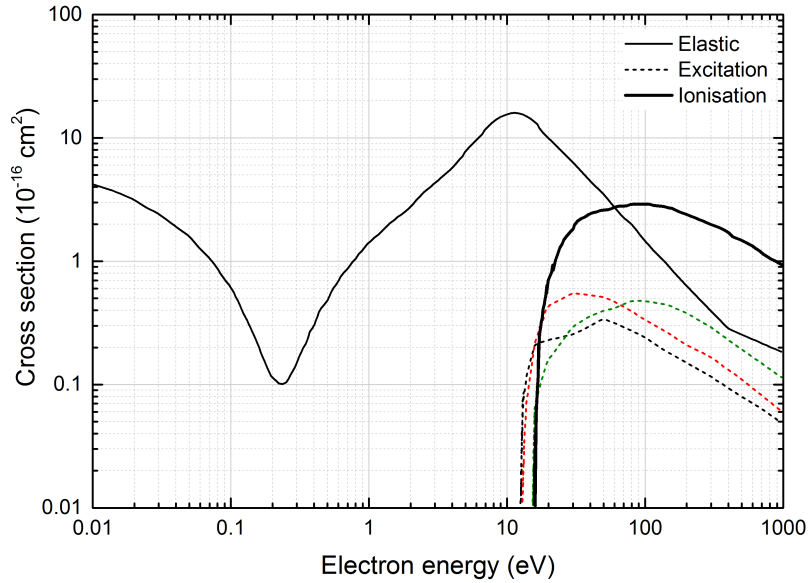

Figure 2.2: Electron cross sections for Argon [8].

The explanation for the strong dependence of the drift velocity on the gas mixture is found in figures 2.2 and 2.3. As shown in figure 2.2, electrons moving in a noble gas can lose their energy only through elastic scattering, excitation or ionization. With increasing drift velocity and resulting higher electron energy the probability for elastic scattering increases significantly. The electrons scattering on the gas molecules are therefore slowed down again before reaching the necessary energies to excite or ionize the gas molecules, as will be discussed in section 2.2.

As seen in figure 2.3, adding small amounts of poly-atomic molecules increases the probability for electrons to interact with these molecules by other means than elastic scattering. Therefore, for a given electric field, the average electron energy is decreased. The total cross section in the relevant energy range is reduced. With the mean free path inversely proportional to the electron cross sections the electrons are less likely to scatter on the molecules and their velocity is increased considerably between each interaction when compared to pure noble gases.
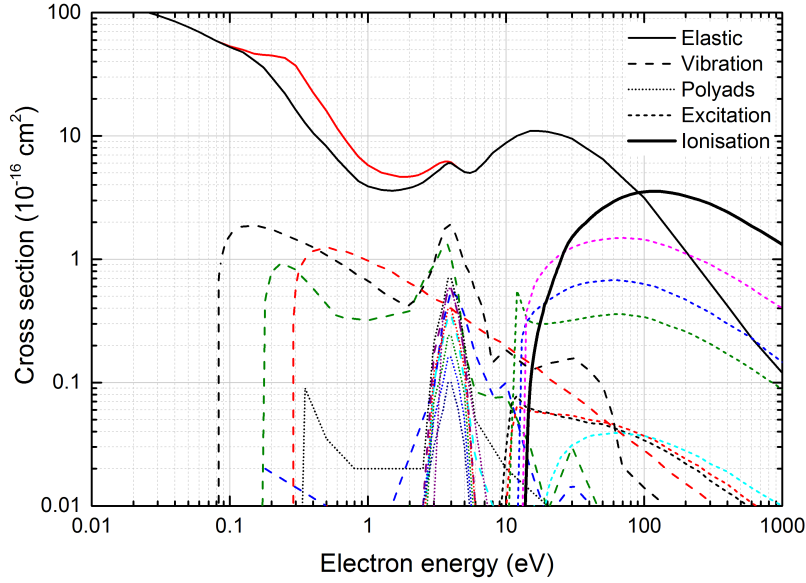
Figure 2.3: Electron cross sections for Carbon dioxide [8].

2.1.2   Diffusion

As mentioned before, the electrons and ions undergo multiple collisions with the gas molecules. This leads to a symmetric diffusion from their original position, which follow a Gaussian law and can be described by

$$\frac{dN}{N} = \frac{1}{\sqrt{4\pi Dt}} e^{-\frac{x^2}{4Dt}} dx \; ,$$
(2.6)

with dN/N as the fraction of particles found in dx at a distance x from their original position and after a time t. The standard deviation of the diffusion in one direction is given by

$$\sigma_x = \sqrt{2Dt} \; .$$
(2.7)

The diffusion coefficient D is dependent on the gas mixture used and the temperature and pressure inside the detector. Within an applied electric field the *ions* diffuse along their drift direction, with the probability distribution given in 2.6 and the linear standard deviation

$$\sigma_x = \sqrt{\frac{2kT}{e}\frac{x}{E}}$$
(2.8)

depending only on the field E applied but not on the type of ion in the gas mixture.

During the drift in the electric field the *electrons* undergo multiple collisions with molecules, changing both their direction and speed. The diffusion therefore strongly depends on the electric field E applied. With the relation between diffusion and mobility as
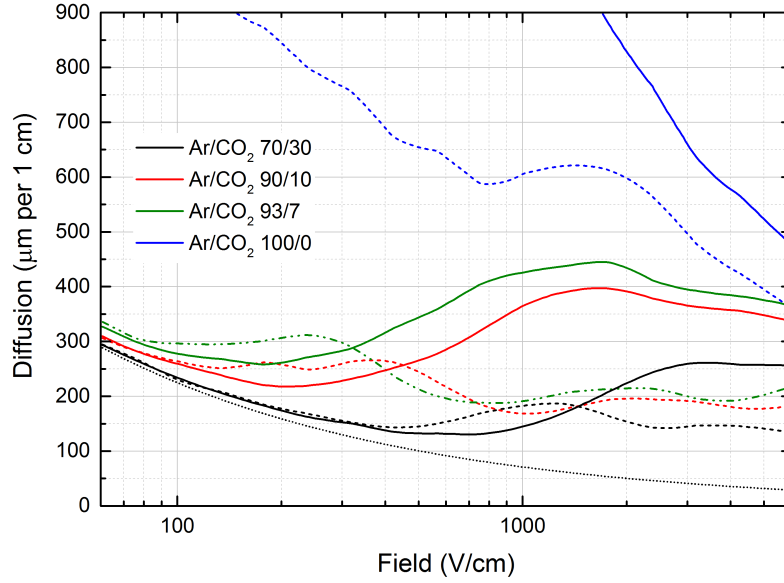
Figure 2.4: Dependence of transverse diffusion (solid) and longitudinal diffusion (dashed) on the electric field for different Ar/CO_2 gas mixtures [8] compared to ion diffusion (dotted).

$$\frac{D}{\mu} = \frac{\epsilon_k}{e} \; , \tag{2.9}$$

using the characteristic energy

$$\epsilon_k = \frac{e \; E \; D(E)}{w(e)} \tag{2.10}$$

with both the drift electron velocity $w(E)$ and diffusion coefficent $D(E)$ depending on the electric field, the diffusion equation for ions 2.8 is changed for electrons to

$$\sigma_x = \sqrt{\frac{2\epsilon_k}{e} \frac{x}{E}} \; . \tag{2.11}$$

The diffusion under the influence of an electric field differs for electrons moving in the direction of the field and those moving perpendicular to it. This can be explained by taking into account that, after a collision with the gas molecules, electrons move into different directions, with their movement in the longitudinal direction being additionally influenced by the applied field. Referring to the direction of the diffusion, the diffusion perpendicular to the drift is named transverse diffusion, the one in the direction of the drift is called longitudinal diffusion. Figure 2.4 shows the diffusion of electrons at different fields for the gas mixtures used within the scope of this thesis. Since the electron diffusion depends on several parameters, most importantly the field applied and the mean free path length in the gas mixture used, the calculation of the diffusion can only be done by numerical methods, as used for example in [8].

2.2   Charge amplification

2.2.1   Ionization

With increasing electric field the drifting electrons gain enough energy between collisions to increase the probability of inelastic phenomena, excitation or ionization, as shown in figures 2.2 and 2.3. For high enough fields the electrons might ionize a gas molecule, creating an electron-ion pair in the process. Both the original electron and the one created soon afterwards acquire enough energy to again ionize other molecules, leading to an exponential growth of a so-called electron-ion avalanche. Using the mean free path λ between ionizing collisions, one can define the first Townsend coefficient

$$\alpha = \lambda^{-1} = N\sigma_i \tag{2.12}$$

as the number of electron-ion pairs produced by a single electron per unit length of drift, with N as the number of molecules per unit volume and the ionization cross section σ_i. The exponential growth of charge can be calculated by assuming an increase $dn = n\alpha dx$ of a number n of electrons after a path dx. Integration over a path length x leads to the charge multiplication factor

$$M = \frac{n}{n_0} = e^{\alpha x} \text{ or } M = e^{\int_{x_1}^{x_2} \alpha(x)dx} \tag{2.13}$$

for uniform and non-uniform electric field. The Townsend coefficient can be computed for different field geometries, as will be shown in section 3.2.11 on page 48.

Noble gases, excited by electron impact, can only de-excite through radiative processes. For a detector operated at standard ambient temperature and pressure in pure argon the energy of an emitted photon is approximately $9.65\,\mathrm{eV}$ [10]. The photon's energy is higher than the ionization potential of copper (about $7.7\,\mathrm{eV}$) constituting the cathode of the detector. This leads to the extraction of photo-electrons from the cathode. Additionally, argon ions are neutralized by the extraction of an electron from the cathode, leading to the emission of either a photon, or secondary emission of an electron from the cathode surface. Both effects will result in a delayed spurious avalanche and might lead to continuous discharges even at moderate gains of the detector.

Using noble gases requires lower operational voltages due to their lack of many non-ionizing energy dissipation modes available in polyatomic molecules. Adding small quantities of different elements and especially polyatomic molecules to pure noble gases leads to some important changes in behaviour. Additionally to the previously discussed influence on the electron drift velocity, noble gas excitation can be passed to poly-atomic molecules. These quenchers have a larger probability to de-excite through elastic collisions or dissociation into simpler radicals, rather than radiatively. This effectively quenches the typical UV-scintillation of noble gases.

Additionally, choosing a quencher with a lower ionization threshold than the one of the gas used will also enable noble gas ions to transfer their charge to the quencher molecules. The mean free path between those interactions is several orders of magnitude smaller than the typical scale of gaseous detectors. Therefore only the species of ions with the lowest ionization threshold will remain to be neutralized at the cathode. The excess energy is then dissipated again through the same processes as before. The probability of secondary photon emission from the cathode is dramatically reduced.

The addition of electro-negative impurities leads to an increased probability of electron capture and formation of negative ions, which drift towards the anode of the detector but don't undergo charge amplification for the fields typically used. While small amounts of these impurities are unavoidable, large amounts of contaminants in the gas, e.g. oxygen or water, might lead to a great loss of primary charge and poor detector performance.

2.2.2 Charge amplification modes

Depending on the voltage applied between the anode and the cathode of a gaseous detector, there are five different modes of operation, of which only the third one, the proportional mode, will be used within the scope of this thesis.
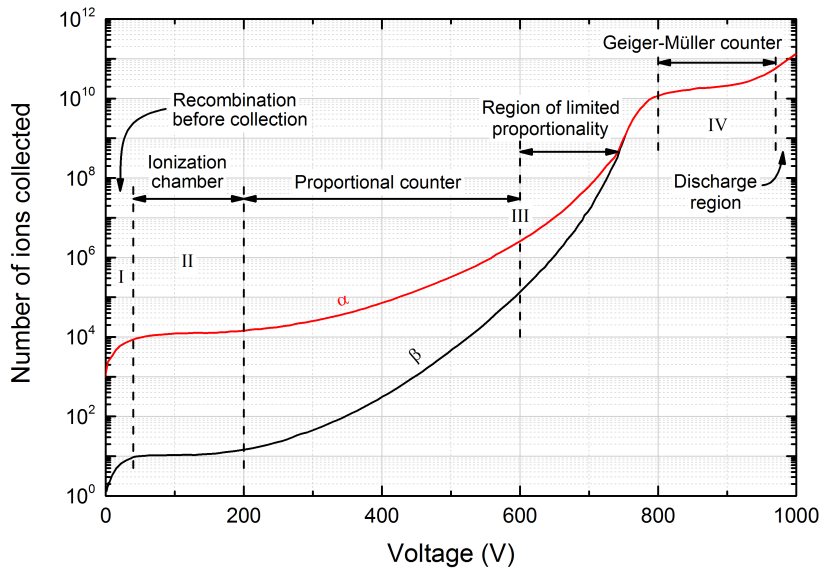
Figure 2.5: Overview of the charge amplification modes depending on the voltage applied between anode and cathode of a wire chamber [1].

Figure 2.5 shows the amplification modes in terms of ions collected on the cathode of a wire chamber. While this figure only shows the case for one detector type, the number of ions collected is proportional to the effective gain and is applicable to any kind of gaseous detector. Depending on the type of gaseous detector and the gas mixture used, the voltages for the different operation regimes have to be adapted accordingly.

In the *recombination mode* (I) the fields are so low that the primary charge will not be collected fully due to the electrons being lost during recombination with ions. Once the voltage is high enough that all the primary charge is collected, the detector is running in *ionization mode* (II). Only after applying a higher voltage, the fields get high enough to allow charge multiplication. The charge collected is proportional to the initial charge. In this *proportional mode* (III) it is possible to measure the energy of the ionizing particle if the calibration of the detector is known. If the voltage is further increased, the fields are high enough for photons emitted during the charge amplification to create further electron-ion pairs at a different position inside the detector, which are again multiplied in an avalanche. This process is only stopped once the number of ions gets large enough to reduce the electric field below the threshold value needed for charge amplification. Independent of the primary charge, the signal in this *Geiger-Müller mode* (IV) is defined by the total amount of charge before breakdown of the avalanche and will therefore always have the same amplitude. For further increased voltage the *streamer or discharge mode* (V) is reached, in which an avalanche triggers another avalanche and so on, until a continuous discharge or conductive channel appears, effectively shorting anode and cathode.

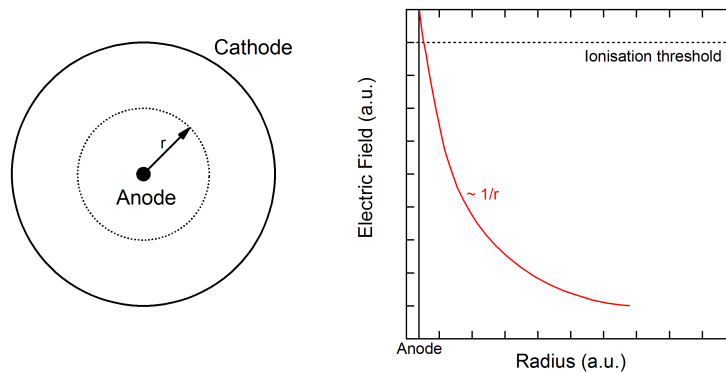## 2.3   History of Micro-Pattern Gaseous Detectors

Figure 2.6: Schematic view of a SWPC (left), and dependence of the electric field on the distance from the cathode axis (right). Modified from [1].

A single-wire proportional counter (SWPC) consists of a cylindrical cathode and an anode, several micrometres thin, mounted along the axis of the cathode, and electrically insulated from it. Cathode and anode are enclosed in a gas-tight volume, which is filled with a counting gas. A potential difference is applied between anode and cathode, with positive polarity on the anode with respect to the cathode. A schematic view of an SWPC is shown in figure 2.6, along with the electric field in dependence of the distance from the cathode axis.
Electrons and ions created in the detector volume by photons or charged particles are drifting towards the anode and cathode in the electric field, as described previously. The electric field

is only strong enough for the electrons to overcome the ionization threshold close to the anode wire. Any primary charge deposited within the detector will therefore first drift into the region of high field surrounding the anode wire and is then amplified equally. The read-out charge is therefore proportional to the deposited charge, as opposed to e.g. parallel plate amplification, where the magnitude of amplification depends on the length of the avalanche, i.e. the position of the first interaction within the detector volume.

The multi-wire proportional counter (MWPC) [11] uses the principles of a SWPC, with a series of equally spaced anode wires arranged on a plane, enclosed by two planar cathodes on the top and bottom of the plane. The MWPC allowed planar detectors with previously unattainable spatial resolution, achievable with only a single detector. For his invention George Charpak was awarded the Nobel Prize in Physics in 1992 [12]. One of the greatest limitations to the use of MWPC is its limited rate capability due to ion space-charge effects.
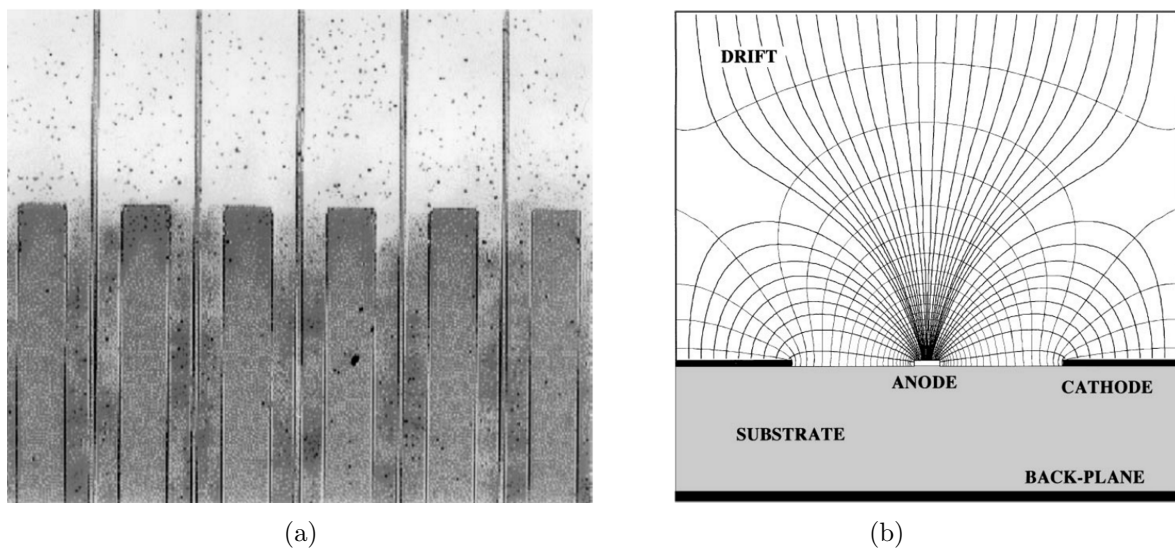

(a)   (b)

Figure 2.7: Detail of the first microstrip plate (left) and schematic drawing with field lines (right) [13].

The micro-strip gas counter (MSGC) [14] was the first development to replace the wires of gaseous detectors with strips produced in photo-lithographic processes. Instead of using the high fields in close vicinity to the anode wires, the read-out stage of the MSGC consists of alternating thin anode and thick cathode strips engraved on a thin insulating support, some hundred micrometres apart. With a potential difference applied between the alternating strips and sizes of the order of hundreds of micrometres, the fields are high enough only close to the microstrip plate to allow for electron multiplication. A close-up image of the microstrips is shown in figure 2.7 (a), a schematic cross section and the applied field is found in figure 2.7 (b).

The MSGC considerably improved position resolution and rate capabilities. It also was
the first of a new type of gaseous detectors, the so-called micro-pattern gaseous detect-
ors (MPGD), in which patterned amplification and read-out stages with sizes in the sub-
millimetre range were introduced. A large number of different devices was developed, which
are summarized in [13] and references therein. One type of detector, the Gaseous Electron
Multiplier (GEM), was used within this thesis and will be explained in further detail in the
next sections.

2.4   The Gaseous Electron Multiplier

In this section the Gaseous Electron Multiplier (GEM) [7][15] will be presented. The steps
involved in the production of this type of detector, its assembly, and considerations about
powering and reading of the charge are explained at the end of the section.

The parameters of the GEMs and their arrangement in a detector presented in this section
can be adapted to the specific needs of many individual applications. The values listed below
- and used within this thesis - are adopted from the tracking detector of the COMPASS
experiment [16]. They continue to be used as what is referred to as a *standard* GEM at the
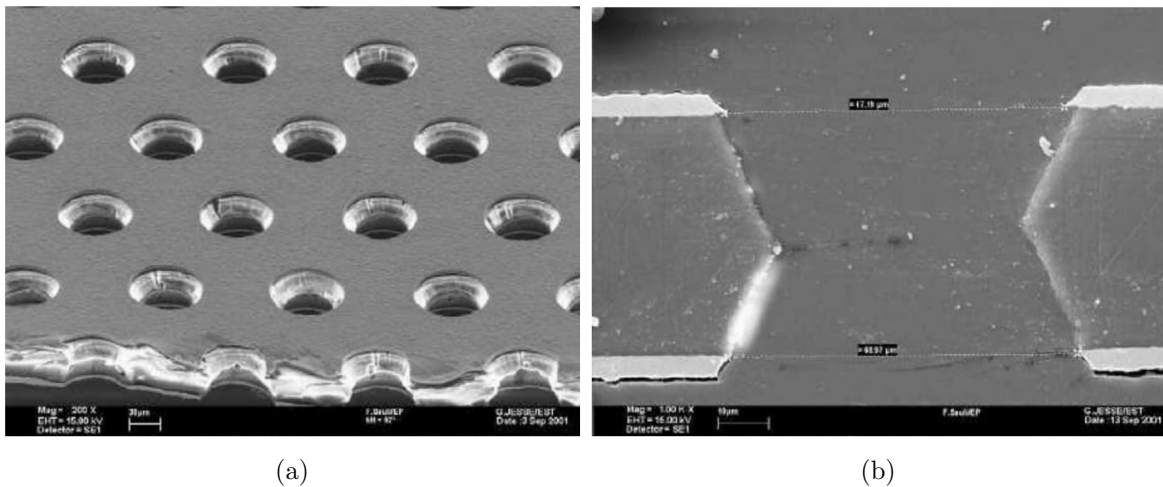CERN gaseous detector development group.

(a)   (b)

Figure 2.8: SEM image of a GEM foil and cross-section of a foil with $70 \, \mu$m and $50 \, \mu$m outer
and inner hole diameter and a pitch of $140 \, \mu$m [16].

A *standard* GEM consists of a polyimide foil (usually Kapton$^{\text{TM}}$) of 50 μm thickness
covered with 5 μm of copper on both sides. Double-conical holes with $70 \, \mu$m and $50 \, \mu$m
outer and inner diameter are etched into the *active area* of the foil in a honeycomb pattern
of $140 \, \mu$ pitch. An SEM picture of a GEM and its cross section can be seen in figure 2.8.
The double-conical shape of the holes originates from the chemical etching involved in the
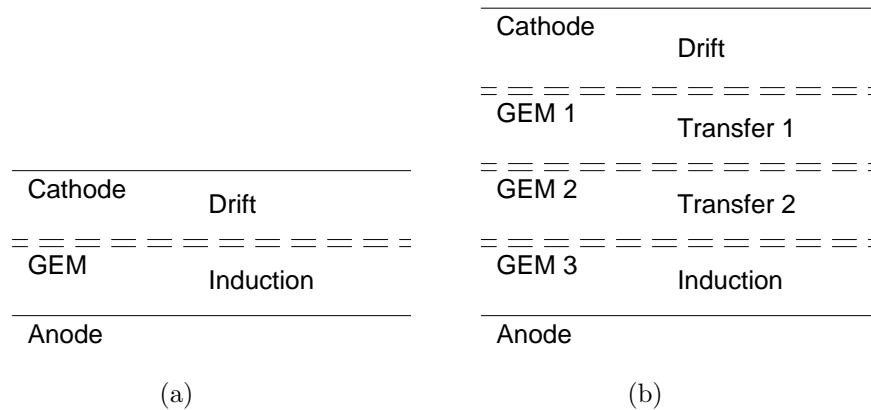production of the GEM foils.

Figure 2.9: Schematic drawing of a single-GEM (a) and a triple-GEM (b).

The GEM is introduced between the cathode and anode of the detector, as shown in figure 2.9 (a). The *top electrode* of the GEM faces the cathode, and the *bottom electrode* faces the anode. The anode is kept at ground potential. The bottom electrode of the GEM is supplied with high voltage. The potential difference between the bottom electrode and the anode is high enough to allow fields of the order of a few kV/cm. The potential of the top electrode is typically of the order of 300 V to 500 V above the bottom electrode to allow fields large enough for amplification. The cathode is again supplied with a higher potential than the top electrode, allowing for fields in the order of several hundred V/cm to a few kV/cm. A GEM detector thus consists of two cathodes (detector cathode and top electrode) and two anodes (bottom electrode and read-out anode), each operated at different potentials. The charge of a traversing particle is converted into a number of primary electrons within the gas-filled volume of the detector. The primary electrons released in the *Drift* or conversion volume drift towards the GEM. They are collected in the GEM holes, where they undergo charge amplification. The magnitude of amplification is governed by the field between the top and bottom electrode of the GEM. The electrons are then extracted from the GEM holes and drift within the *Induction* volume towards the anode. The induced electron signal is read out at the anode.

The GEM was initially invented to be used in combination with other gaseous detectors, with the GEM being "inserted in a gas detector on the path of drifting electrons ... to pre-amplify the charge drifting through the channels ... to obtain higher gains, or to operate in less critical conditions." [15]. It was already envisioned to work as a stand-alone detector "with a much simpler, cheaper and more reliable stripped printed circuit." [17]. A GEM detector with a printed circuit read-out board was realized and found to reach gains of the order of one hundred, or gains exceeding one thousand for two gaseous electron multipliers stacked one on top of the other [18].

This already shows some of the main advantages of GEM-based detectors: the amplification stage is fully separated from the read-out anode. The read-out anode can therefore be optimized to the specific requirements of the detector. Additionally, several GEMs can be stacked on top of each other to achieve higher gains at significantly reduced discharge probabilities.

A double-GEM detector introduces a second GEM between the first GEM and the anode. The potentials of the first GEM's electrodes and the cathode are increased accordingly. The *Transfer* field between the bottom electrode of the first GEM and top electrode of the second GEM is again typically in the order of a few kV/cm. Electrons extracted from the holes of the first GEM therefore only drift towards the second GEM and are multiplied in the high fields of the second GEM's holes.

For a triple-GEM detector a third GEM is added between the second GEM and the read-out anode. A triple-GEM detector then consists of a drift cathode, three GEMs and a read-out anode, as shown in figure 2.9 (b). The *Drift* gap is defined by the cathode and the top electrode of the first GEM. The *Transfer 1* gap is determined by the bottom electrode of the first GEM and the top electrode of the second GEM. The *Transfer 2* gap is enclosed by the bottom electrode of the second GEM and top electrode of the third GEM. The *Induction* gap is defined by the bottom electrode of the third GEM and the read-out anode.

2.5   The standard triple-GEM detector

As explained in section 2.4, a *standard* triple-GEM detector comprises three individual GEMs, each consisting of a 50 μm thick Kapton$^{\text{TM}}$ foil covered with 5 μm of copper on both sides. Double-conical holes of 70 μm and 50 μm outer and inner diameter are etched into the foil in a honeycomb pattern of 140 μm pitch in what is considered the detector's *active area* of $10 \times 10 \, \text{cm}^2$. The copper surface protrudes the active area by several millimetres on each side to prevent field distortions on its borders. The foil is then stretched and glued between two fibreglass frames of 0.5 mm thickness each, with strips for each face of the GEM fed through the frame for high voltage connection. The drift cathode consists of a Kapton$^{\text{TM}}$ foil with equal dimensions. It is copper-clad only on the bottom side but otherwise stretched and framed as a GEM, with only one connector for high voltage and a continuous surface in the active area.

The 2D readout anode used within the framework of this thesis consists of the same material as GEM foils and cathode and is also manufactured by chemical etching. It has two axes, aligned perpendicular to each other, with one on top of the other. Each axis consists of 256 parallel strips with a pitch of 400 μm. The top axis' strips have a width of 80 μm, the bottom axis' strips are 350 μm wide to allow equal sharing of charge between both axes. The two axes

are $5\,\mu$m thick and separated by a Kapton$^{\text{TM}}$ ridge of $50\,\mu$m height. The read-out anode is glued onto a printed circuit board (PCB) with the strips connected to Panasonic connectors in batches of 128 each, with the possibility to bundle all strips and read the charge induced to the whole anode or read each strip individually with a suitable read-out system [19].
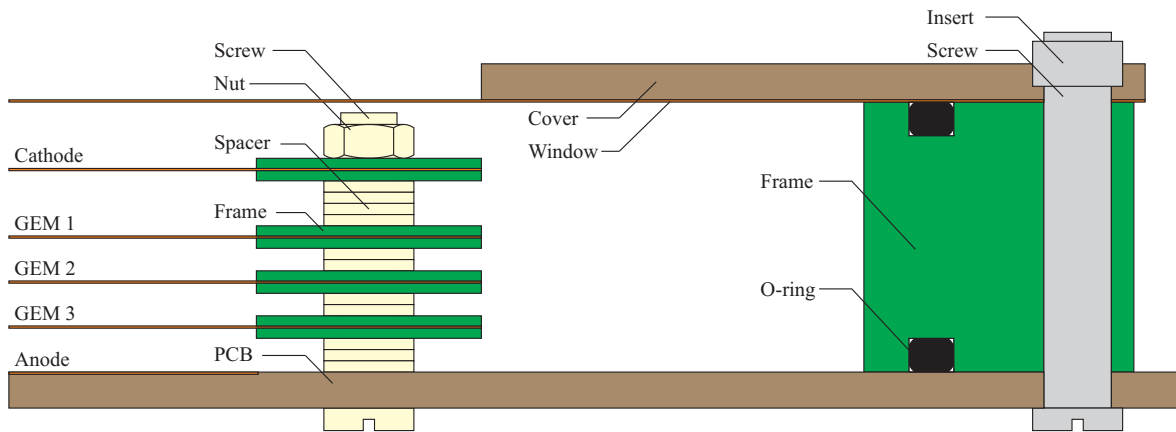
2.5.1 Assembly

Figure 2.10: Assembly scheme of a GEM detector. For explanations see text.

The assembly starts with the PCB read-out board, which comes fully assembled with the desired read-out anode and suitable connectors on two sides of the board (top and right), and five high-voltage feed-throughs on the other two sides (bottom and left). Four nylon screws are pushed through the corresponding holes close to the corners of the anode. They are fixed onto the board from the bottom-side of the detector with non-outgassing glue.
A number of nylon washers are placed on the screws to define the distance between the anode and the third GEM. The nylon washers have a thickness of 0.5 mm each. The thickness of the frame below the GEM foil of 0.5 mm has to be taken into account when putting the right number of washers. The distance between each GEM is defined in the same way.
The gap lengths for a *standard* triple-GEM detector are 3 mm for the *Drift* gap and 2 mm for each of the other gaps. The frames are then fixed onto the screws with nylon nuts. The screws might be cut at the top of the nut to reduce the overall detector height. An assembly scheme of the detector is shown in figure 2.10.
The connectors of each GEM and the drift cathode are soldered to the high voltage feed-throughs embedded into the read-out PCB.
The detector is then enclosed in a gas-tight chamber. The read-out board acts as the bottom cover of the chamber. A square frame of 12 mm height and about 15 cm edge length is used to define the walls of the chamber. The frame features grooves on the top and bottom side,

into which o-rings are placed. A cover is then tightly screwed onto the top of the chamber, consisting of a thin Kapton^TM foil and a fibreglass shield. The Kapton^TM foil spans the whole area of the detector. The fibreglass shield has an opening of approximately the active area of the detector to serve as a window for soft X-rays. Two sides of the chamber walls feature holes with threads in them, into which connectors for the gas input and output are screwed. For setups surpassing the height of one chamber frame one or more additional frames are mounted between the first frame and the cover. These frames only feature grooves on the top side into which an o-ring is placed.

The high voltage feed-throughs are then connected as required by the setup, and as is described in section 2.5.3.
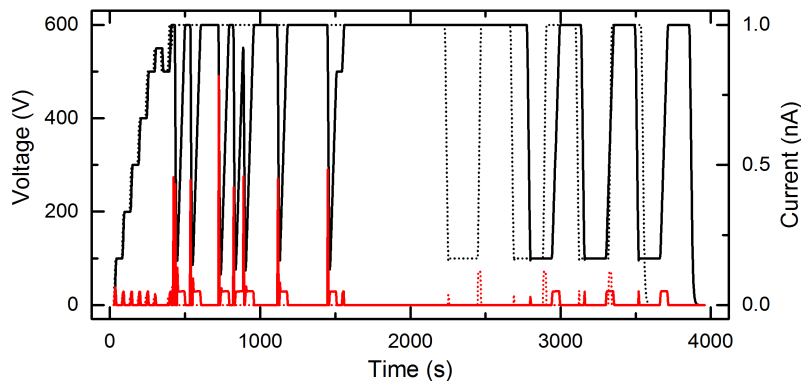
2.5.2 Quality assurance

Figure 2.11: Voltages (black) and currents (red) of a GEM foil test. The first foil (solid) shows several discharges, the second one (dotted) is in perfect condition. Both foils passed the test and were mounted in a detector.

All GEM foils are tested outside the detector before assembly. They are mounted in a transparent and gas-tight box equipped with feed-throughs for high voltage. The box is flushed with nitrogen to reduce the relative humidity to less than 30%.

The foils are then tested by checking the leakage current between the two electrodes. The bottom electrode is kept on ground while 600 V are supplied to the top electrode. The current drawn from the power supply is then monitored. After the voltage is stable at 600 V the current should go down to less than 2 nA to pass the test. This method is also used to remove dust particles and other small impurities from the GEM electrodes. The current limit of the high voltage power supply is set to about $4\,\mu$A, allowing enough current supplied to the electrode to burn off dust particles attached, resulting in a clearly visible spark on the electrode. The position and number of any sparks is monitored. For a GEM foil in mint condition only a few sparks appear, with a stable supply of voltage and current afterwards. If however the frequency of sparks is not decreasing or the sparks are localized in one spot,

i.e. a possible defect is contained within a single GEM hole, the foil has to be returned to the manufacturer.

After checking the leakage current an additional test is conducted to check if the foil is working properly when changing the potential difference between the electrodes. The bottom electrode is kept at ground potential during the whole test, while the voltage on the top electrode is increased in several steps up to a limit of 600 V, as with the previous test. During every step first the voltage is changed and then kept at the given value until the current on the electrode reaches a stable value. Should no discharges occur until the current is stable, the voltage is ramped to the next value, otherwise the voltage of the previous step is applied and the test continued from there. After the voltage reaches the final step of 600 V, with a stable current and only a limited number of discharges, the voltage is reduced to 100 V and increased to 600 V several times to make sure that the foil withstands rapid changes in voltage. After this final steps are passed, the foil can be mounted in the detector. Examples of foil tests are shown in figure 2.11.
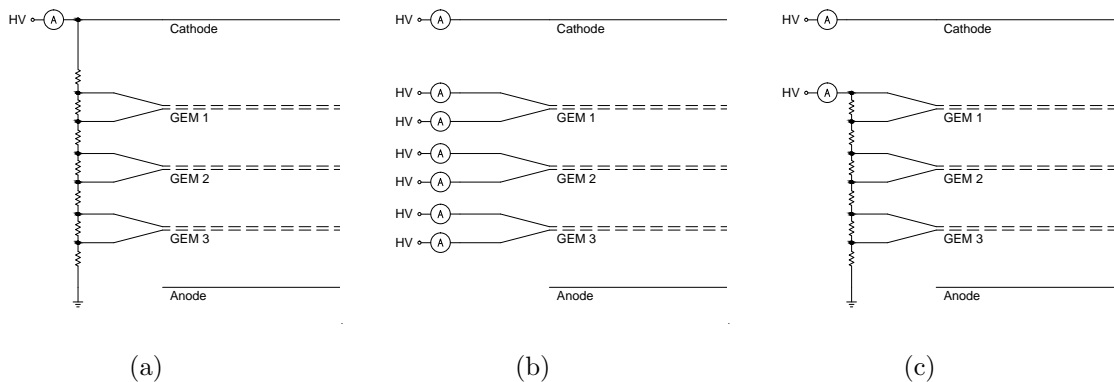
2.5.3 Powering schemes

Figure 2.12: Different powering schemes for a triple-GEM detector: resistor divider (a), each electrode powered individually (b), and resistor divider with the drift cathode powered individually (c)

There are several ways to power a GEM detector:

- **Powering all electrodes with a resistor divider** (figure 2.12 (a)). All stages of the detector use one common high voltage power supply, with the individual potentials supplied by a resistor divider. The fields across the GEM and between them can only be changed linearly by increasing or reducing the overall voltage supplied to the resistor divider. A power supply with a high current output is required.

- **Individually powering each electrode** (figure 2.12 (b)). All electrodes are powered individually. While being able to change each field individually is an advantage for

certain purposes, this methods may lead to failure or destruction of the GEM foils when no special attention is brought to discharge protection and fail-safe operation of one or more power supplies providing the voltages. Protection resistors are used to limit the current across a GEM foil in case of discharges. The power supply is operated in a way that if one channel fails all other channels are triggered to shut down immediately to reduce the possibility of large currents across the GEM foils. Even if one failing channel of one power supply shuts down all power supplies used it should be ensured that the electrodes of one GEM are not powered by two different power supplies.

An advantage of this method is the possibility of reading the current induced in all stages of the detector either by ammeters built into the power supplies or by adding ammeters in the high voltage line of each electrode.

- **Powering the GEMs with a resistor divider, powering the cathode individually** (figure 2.12 (c)). This method allows safety of operation for all stages of the GEM while at the same time being able to change the *Drift* field individually. When an ammeter is used in series with the high voltage power supply of the cathode, the ion back-flow into the conversion volume can be studied.

2.5.4   GEM gain and efficiencies

As explained in section 2.1, the electrons and ions follow the field lines within the detector volume. The fields above and below a GEM are typically in the order of a few kV/cm. The amplification field between the top and bottom electrode of a GEM is usually several tens of kV/cm. The field lines thus get focussed into the GEM holes, as can be seen for a few example values in figure 2.13. Depending on the magnitude of the fields above and below the GEM, some of the field lines end up on one of the electrodes, resulting in a loss of charge before or after amplification. The electron *collection efficiency* ε_C defines the fraction of electrons being collected into the GEM hole. For a fixed potential difference between the GEM electrodes it is only dependent on the field above the GEM, as can be seen in figures 2.13 (a) to (c). For lower fields above the GEM, the collection efficiency increases.

For a fixed potential difference applied between the GEM electrodes the electron *extraction efficiency* ε_E is defined by the field below the GEM. Figures 2.13 (d) to (f) show the field lines depending on the the field below the GEM. For higher fields the extraction efficiency is increased.

The *effective gain* is defined as the charge read from the anode per charge deposited in the detector volume and is calculated as

$$G_{eff} = \frac{I_A}{n_p R e} \; , \tag{2.14}$$

with the current I_A induced on the read-out anode during irradiation, the estimated interaction rate R, the number of primary electrons n_p (or ionization yield) created in the
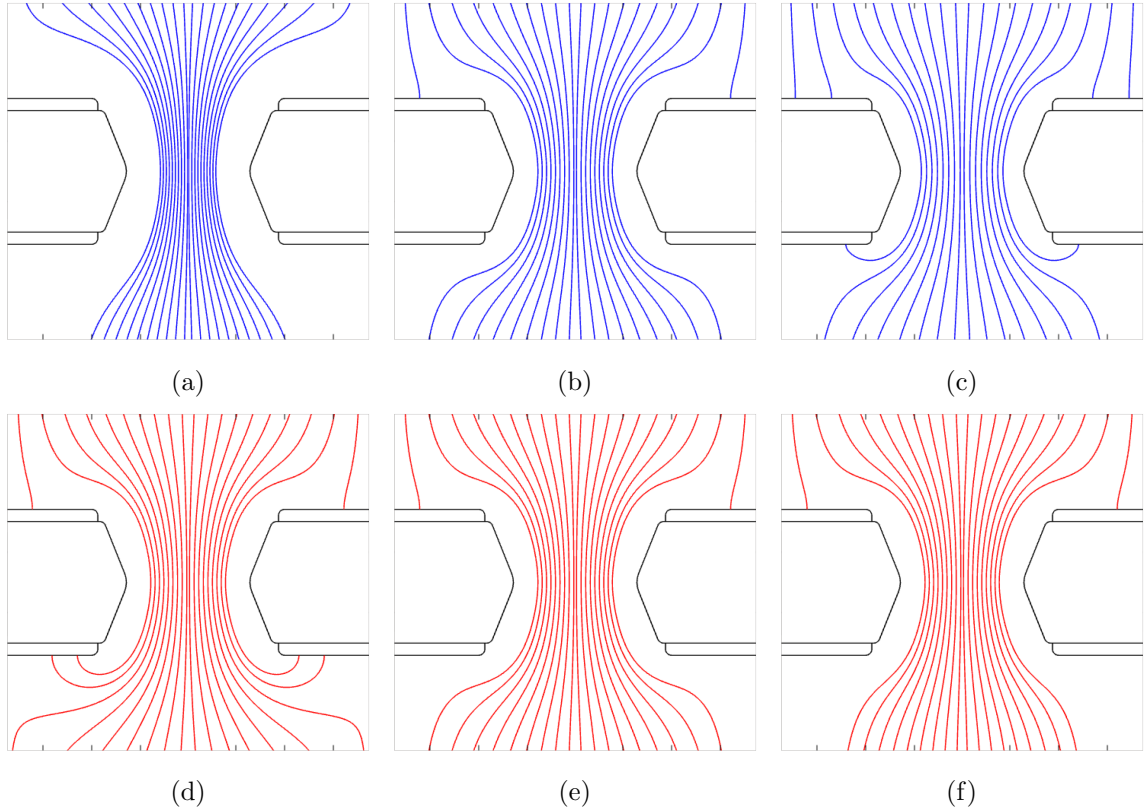
Figure 2.13: Field lines in the GEM holes for a field on the bottom ((a) to (c)) and the top ((d) to (f))of the GEM kept at $3.5\,\mathrm{kV/cm}$ and the other field at $1.5\,\mathrm{kV/cm}$, $3.5\,\mathrm{kV/cm}$ and $5.5\,\mathrm{kV/cm}$. The field inside the GEM is $75\,\mathrm{kV/cm}$. Simulations done with COMSOL Multiphysics® [20].

conversion volume, and the electron charge e. The current I_A is defined as

$$I_A = I_{on} - I_{off} \; , \tag{2.15}$$

with the current I_{on} read during irradiation and I_{off} when there is no irradiation. The non-continuous irradiation of the detector can be easily achieved by either physically removing the radiation source or inserting a sufficiently thick shielding between the source and the detector.

As previously explained, the gain depends on the fields within the GEM holes, which are defined by the voltages applied to the individual electrodes of the GEMs. Measuring the effective gain of a known configuration allows a calibration of the detector. An example of a gain calibration is shown in figure 2.14.
The effective gain of a single GEM depends on the collection and extraction efficiencies and the multiplication M within the GEM holes, thus $G_{eff} \propto \varepsilon_C \varepsilon_E M$.
For a double-GEM or triple-GEM detector the individual collection and extraction efficiencies
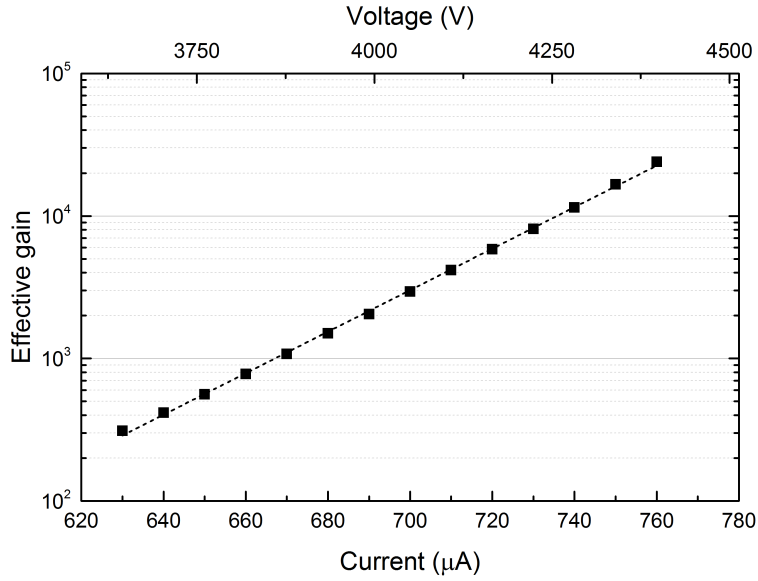
Figure 2.14: Example of a gain calibration for a *standard* triple-GEM detector powered with a resistor divider.

of each GEM have to be taken into account. The effective gain $G_{eff} \propto \prod_{i=1}^{j} \varepsilon_{C,i} \varepsilon_{E,i} M_i$ is proportional to the product of each individual amplification stage, with j as the number of stages.

For a fixed detector geometry the collection and extraction efficiencies, as well as the multiplication depend on the fields in each stage of the detector. Examples for the influence of the hole diameter and hole pitch of a GEM on the effective gain can be found in [21] or [22]. The manufacturing of the GEM foils might lead to geometrical variations of hole diameters or shapes. The assembly of the detector might result in variations of the gap lengths over the full area of the detector. Both geometrical variations lead to changed effective gain over the surface of the detector, as is pointed out in [23].

The *electron collection efficiency* can be studied with a single-GEM detector by variation of the *Drift* field E_D, with the induction field E_I kept constant. Alternatively, the collection efficiency can be studied with a triple-GEM detector with all fields except the *Drift* field kept constant. Figure 2.15 shows the effective gain of a triple-GEM detector depending on the *Drift* field. For *Drift* fields between 1 kV/cm to 3 kV/cm all of the primary charge gets collected into the GEM holes, as was shown in figure 2.13 (a). For higher fields the electrons end up on the top electrode of the GEM, as can be seen in the field lines of figure 2.13 (b) and (c) respectively. For *Drift* fields lower than 1 kV/cm all field lines end up in the holes of GEM. Here the effective gain is reduced because a part of the primary charge is lost on its way to the GEM. Electrons are getting attached to molecules within the gas volume, thus forming negative molecules which drift towards the holes but don't undergo Townsend multiplication. The dependence of the *electron extraction efficiency* on the *Induction* field is shown in fig-
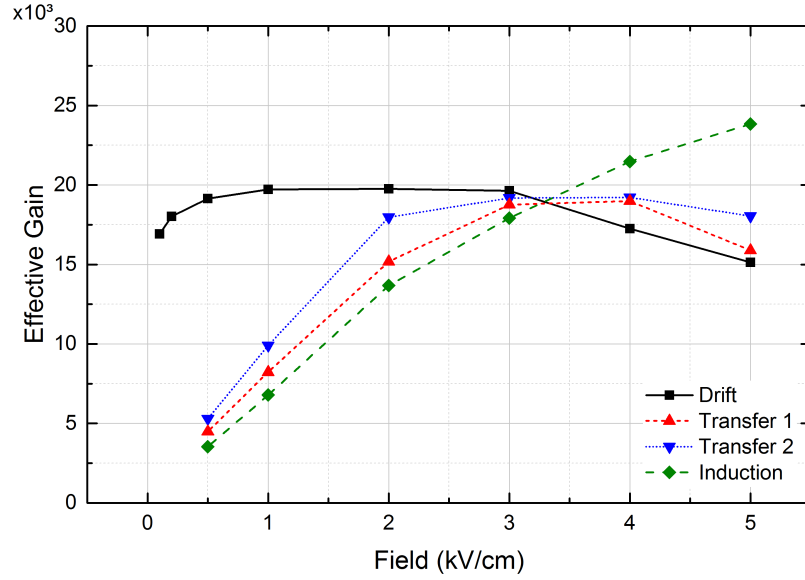
Figure 2.15: Effective gains of the detector depending on the applied fields. The field indicated in the legend of the graph is varied, with the other three fields kept at constant values of $E_D = 1.5\,\text{kV/cm}$, $E_{T1} = 3.6\,\text{kV/cm}$, $E_{T2} = 3.6\,\text{kV/cm}$ and $E_I = 3.6\,\text{kV/cm}$.

ure 2.15. As pointed out earlier, the extraction efficiency increases with higher induction field. Increasing the induction field further would lead to full extraction efficiency, before parallel plate amplification in the induction region would occur [21].

Figure 2.15 also shows the effective gain depending on the *Transfer 1* and *Transfer 2* fields. Increasing the *Transfer 1* field increases the extraction efficiency of the first GEM but at the same time reduces the collection efficiency of the second GEM. Reducing the field has the inverse effect. The same is true for variations of the *Transfer 2* field and the second and third GEM respectively.

For ions, the picture in figure 2.13 has to be inverted. The ions are drifting from the bottom of the GEM (above the GEM in the figure) to its top (below the GEM in the figure). For higher *Induction* fields, more ions end up on the bottom of the GEM electrode. For lower *Drift* fields, a larger number ends up on the top electrode of the GEM. The *ion collection efficiency* is therefore decreasing with increasing induction field. The *ion extraction efficiency* on the other hand is increasing with increasing *Drift* field.

Chapter 3

Effects of High Charge Densities in Multi-GEM Detectors

Gaseous Electron Multipliers are known to operate at stable gains when exposed to soft X-ray fluxes of up to 10^6 Hz/mm^2 for single stage devices used in combination with an MSGC [24] and up to 10^5 Hz/mm^2 for double stage devices [25]. For triple stage devices it was observed that at high fluxes of soft X-rays the effective gain as a function of the flux first increases and then decreases. The work concluded that the observed effective gain variations were "caused by a space-charge effect" [26] resulting in field distortions within the detector.
Considerable efforts have been made to reduce the back-flow of positive ions into the conversion volume of multi-GEM detectors to reduce space-charge induced field distortions within the conversion volume [22][27][28]. Further studies [29] show a decrease of the ion back-flow of a triple-GEM detector due to ion space-charge when exposed to high X-ray fluxes.
Both the behaviour of the effective gain and the ion back-flow were assumed to be induced by space-charge effects at very large particle fluxes and moderate effective gains. It was also shown [30] that triple-GEM detectors operated at large effective gains and irradiated with low X-ray fluxes show saturation effects.
The aim of this work is to investigate those effects and establish a link between them.
A theoretical framework for space-charge distortions of the transfer fields in multi-GEM detectors will be introduced in section 3.1. The response of a *standard* triple-GEM irradiated with large X-ray fluxes will be presented in section 3.2. The experimental setup and the methods are described in section 3.2.1 and 3.2.2. An example for the behaviour of triple-GEM detectors under irradiation with large X-ray fluxes in section 3.2.3 introduces the observations studied in detail in the following sections. The observed effects are described in section 3.2.4 for different effective gains of the detector. Systematic studies of the effect depending on individual transfer and amplification fields are presented in sections 3.2.5 to 3.2.10. Simulations shown in section 3.2.11 use the theoretical framework described in section 3.1, and help to achieve a deeper understanding of the observed effects.

The effects observed in single-GEM and double-GEM detectors are presented in section 3.3.1. The event-by-event measurements presented in section 3.4 show the impact on the energy resolution of the detector and complete the study of space-charge effects in GEM detectors under irradation with large fluxes of soft X-rays.

Effects due to high charge densities at very high effective gains and small X-ray fluxes are explained in section 3.5. A discussion and conclusive summary of the observed effects is found in sections 3.6 and 3.7 respectively.

3.1 Field distortions

For a fixed potential difference between the electrodes of a GEM, the electron collection and extraction efficiencies introduced in section 2.5.4 depend on the fields applied above and below each individual GEM. The curves shown in figure 2.13 were acquired with uniform fields across the surfaces of each electrode. Accumulation of charged particles within the detector volume can lead to local distortions of these fields.

To understand the measurements described within this chapter, a model of field distortions due to space-charge effects is presented in section 3.1.1, followed by a few examples in section 3.1.2 to better illustrate the behaviour of the detector.
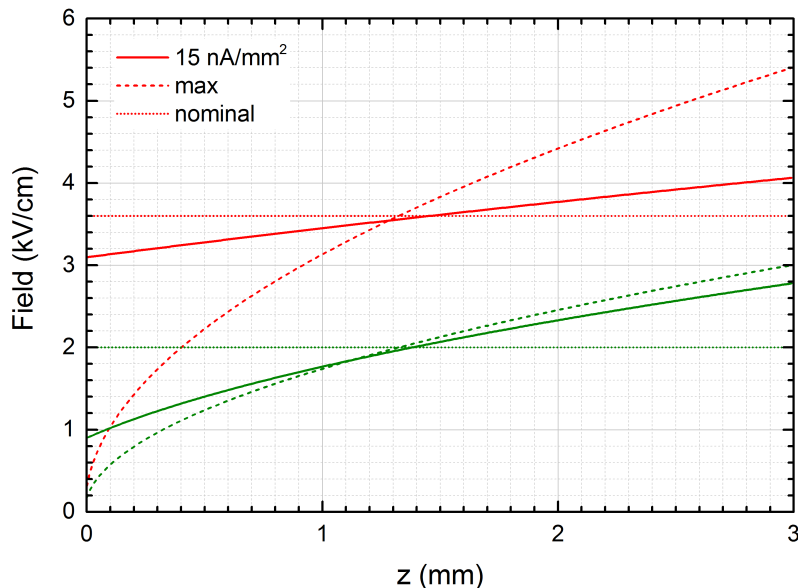
3.1.1 Model

Figure 3.1: Field distortions over a 3 mm gap for nominal fields of 2 kV/cm (green) and 3.6 kV/cm (red) for ion current densities of 15 nA/mm^2. The maximum applicable current densities effectively reducing the fields at the anode to zero are 19.47 nA/mm^2 and 63.07 nA/mm^2.

The effect of ion space-charge induced field distortions observed in each transfer gap of a triple-GEM detector can in first order be described by two infinite parallel planes, arranged within a distance L to each other. A voltage difference ΔV is applied between them, leading to a uniform electric field $E_0 = \Delta V/L$. The plane at position $z = 0$ acts as an *anode*, creating ions at a constant and uniform flux. The ions move towards the *cathode* at position $z = L$ with a speed of $w^+ = \mu E$ depending on the ion mobility μ and field E. The uniform electric field gets modified by the charge distribution of the drifting ions resulting in an electric field

$$E_z = \sqrt{2j(z + z_0)/(\epsilon\mu)} \tag{3.1}$$

with z_0 such that

$$\Delta V = \int_0^L E_z dz = \sqrt{8j/(9\epsilon\mu)} \left((L + z_0)^{3/2} - z_0^{3/2} \right) \ , \tag{3.2}$$

where ϵ is the permittivity of the gas, and j is the ion current density. The absolute value of the field decreases where the positive ions *enter* the volume and increases where the ions *exit*. The equivalent effect due to electrons can be neglected since they drift much faster than the ions.

Figure 3.1 shows examples of field distortions between two infinite parallel planes three millimetres apart. Nominal fields of $2\,\text{kV/cm}$ and $3.6\,\text{kV/cm}$ are shown as examples for transfer fields E_{T1} or E_{T2} in a *standard* GEM detectors operated at moderate and high effective gain. The nominal values are shown as dotted lines. The distorted fields due to an ion current density of $15\,nA/mm^2$ are shown as solid lines. The calculated values will be used within the next section to give the reader a better understanding of the effects described in this chapter. Following the field distortions described previously, for a given field E_0 there is a maximal applicable current density j_{max} at which the field on the *anode* will be reduced to $0\,\text{V/cm}$, thus stopping the movement of the ions and electrons:

$$j_{max} = \frac{9\epsilon\mu E_0^2}{8L} = \sqrt{\frac{9\epsilon\mu\Delta V^2}{(2L)^3}} \ . \tag{3.3}$$

The fields changed by the maximal applicable current densities are depicted as dashed lines in figure 3.1. On the other hand, for a given current density j there is a minimum field E_{min} to be applied to allow ions to move away from their initial position at $z = 0$:

$$E_{min} = \sqrt{\frac{8jL}{9\epsilon\mu}} \ . \tag{3.4}$$

3.1.2 Examples

This section intends to give the reader an understanding of the effect of field distortions on the collection and extraction efficiencies in a GEM detector. The changes for two examples

will be given: for a field of $2\,kV/cm$ and a field of $3.6\,kV/cm$ applied between two GEMs arranged three millimetres apart from each other.

The previously described model uses two infinite parallel planes, with the anode acting as an ion generator. In a GEM detector, electron-ion pairs are generated within the GEM holes during charge amplification. The positively charged ions now drift towards the cathode, but get partly collected on each GEM electrode they pass. While this leads to deviations from the ideal case previously described, to the first order the effects still apply. For the following explanations the ions are again assumed to be uniformly created on the top electrode of the second GEM. A realistic study of the ion-induced field distortions will be given in section 3.2.11.
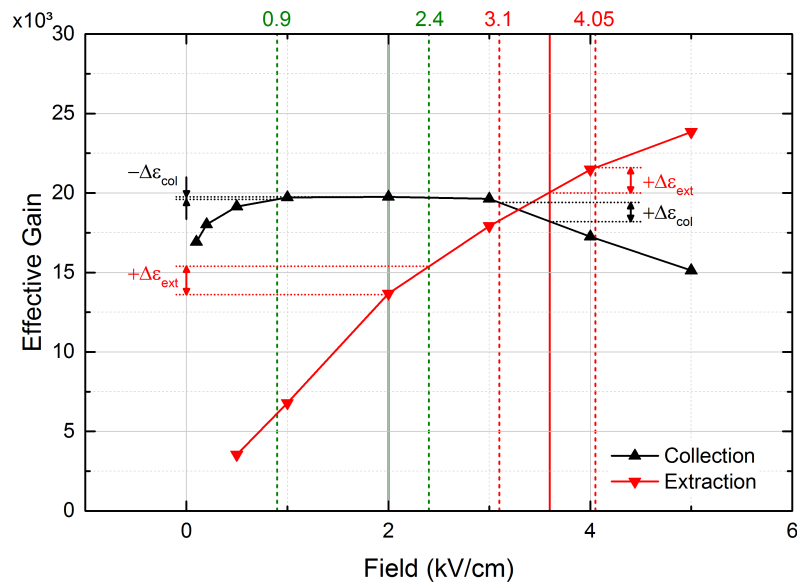

Figure 3.2: Qualitative explanation of the changes in collection and extraction efficiencies in the GEM detector. The field distortions of figure 3.1 are applied to the curves for varied *Drift* field (collection) and *Induction* field (extraction) of figure 2.15.

The solid lines in figure 3.1 show distortions for nominal fields of $2\,kV/cm$ (green) and $3.6\,kV/cm$ (red) for an ion current density of $15\,nA/mm^2$. Figure 3.2 shows the electron collection efficiency depending on the fields above and below the GEM (see also figure 2.15 in section 2.5.4). The nominal fields are shown as solid lines. The modified fields are shown as dashed lines, with their values on the top axis.

For a nominal field of $2\,kV/cm$ the field distortions give a value of $0.9\,kV/cm$ on the top electrode of the second GEM and $2.4\,kV/cm$ at the bottom electrode of the first GEM. Figure 3.2 shows that the collection efficiency of the second GEM is slightly reduced, but more than compensated by the increase of extraction efficiency of the first GEM.

At a nominal field of $3.6\,kV/cm$ the distorted field has a value of $3.1\,kV/cm$ on the top electrode of the second GEM and one of $4.05\,kV/cm$ on the bottom of the first GEM. This

leads to an increase of both the collection efficiency of the second GEM and the extraction efficiency of the first GEM.

While this is only a simplified approach, two things are to be kept in mind: the field distortions might lead to an increased electron extraction efficiency, and might or might not lead to a change in electron collection efficiency. The ion collection and extraction efficiencies behave in the opposite way.

3.2 Dependence of the effective gain on the X-ray flux
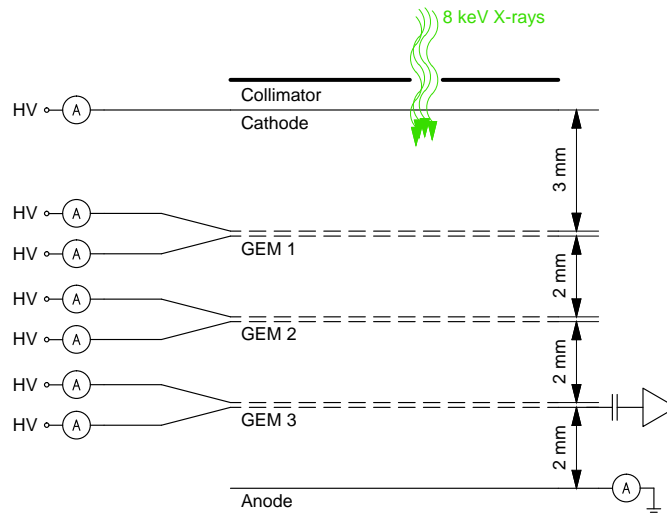
3.2.1 Experimental setup

Figure 3.3: Setup of the triple-GEM detector with all stages of the detector powered individually.

A *standard* triple-GEM detector with hole diameters of $70\,\mu$m, hole pitch of $140\,\mu$m and an active area of $10{\times}10\,cm^2$ was used to study the effects of high charge densities. The used gap lengths were $3\,$mm for the *Drift* gap, and $2\,$mm for the other gaps, as is shown in figure 3.3. The respective volumes were defined by the gap length and the active area of the detector.

Each electrode of the detector was powered individually with a channel of a *CAEN N1471H* high-voltage power-supply [31]. Currents were read on each electrode via the integrated ammeters of the power-supplies. The anode current was read with a *Keithley Model 6487* Picoammeter [32]. Event-by-event signals were read from the bottom electrode of the third GEM via capacitive coupling to an *ORTEC*® *142PC* [33] pre-amplifier and *ORTEC*® *672 Spectroscopy Amplifier* [34]. Pulse-height spectra were acquired with an *AMPTEK MCA-8000D Multi-Channel Analyser* [35].

The detector was continuously flushed with an Ar/CO_2 gas-mixture of 70% Ar and 30% CO_2 mass content at approximately $5\,L/h$.

Collimated $8\,keV$ X-rays of about one millimetre beam diameter from a Cu X-ray generator were used to produce the primary ionisation in the conversion volume. The detector was mounted vertically on a back-plate with a distance of about $30\,cm$ to the X-ray generator. The detector was shielded on the side facing the X-ray tube with a copper plate of two millimetres thickness. A hole at the desired hit position ensured sufficient collimation of the X-ray beam. The X-ray flux was adjustable by changing the X-ray tube intensity or using calibrated attenuators. The X-ray beam could be quickly turned on or off with an integrated shutter.

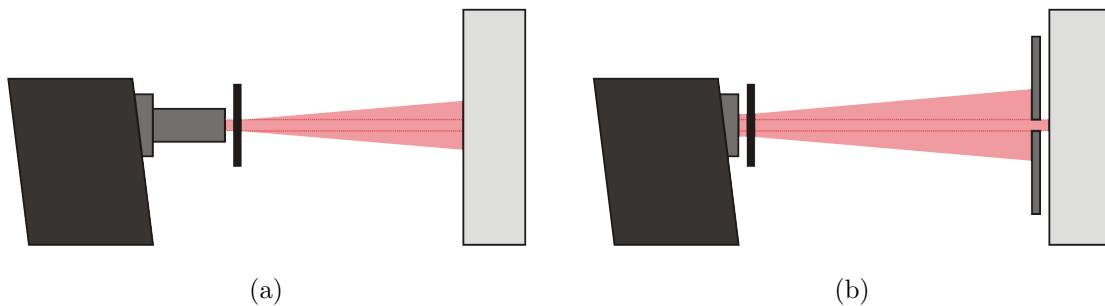(a)   (b)

Figure 3.4: Exaggerated illustration of the problem arising from using a collimated beam with absorbers mounted close to the X-ray tube (a): due to scattering on the absorber the beam gets widened, thus changing the beam diameter. Using a copper plate with holes as an absorber close to the detector overcomes the problem (b).

During early measurements it was observed that the use of different absorbers resulted in a broadening of the X-ray beam due to scattering. The resulting flux was therefore overestimated. Removing the collimator of the X-ray tube and placing a two millimetre thick copper plate with only a single hole of known diameter directly in front of the detector solved the problem. A strongly exaggerated illustration of the problem and the solution is found in figure 3.4.

3.2.2   Measurements and methods

The observed effects were checked to be unrelated to global effective gain variations, e.g. due to changes in ambient parameters. A reference position was continuously irradiated with an Fe-55 source. The peak position of the 5.9 keV peak in the pulse height spectra was continuously monitored when the shutter of the X-ray tube was closed.

All electrodes were powered for at least one hour before starting the measurements to ensure stability of the currents monitored. Charging-up effects [36] were excluded as the origin of

the observed behaviour by waiting until the currents $I_{i,on}$ were stable after starting the irradiation at low flux, and by repeated measurements going from low to high X-ray flux and vice versa.

The currents collected at the drift cathode, GEM electrodes and read-out anode were calculated as $I_i = I_{i,on} - I_{i,beamoff}$. The currents $I_{i,beamoff}$ were the currents read on the i-th electrode when the shutter of the X-ray tube was closed. These currents take into account the charge collected when the detector is continuously exposed to X-rays of the Fe-55 source as well as leakage currents on the electrodes. The currents $I_{i,on}$ were the currents read when the detector was additionally irradiated with X-rays of the Cu X-ray tube.

The *effective gain* was calculated as $G_{eff} = I_A/(Rn_pe)$ with the current I_A collected at the read-out anode, the estimated interaction rate R, the number of primary electrons $n_p \approx 290$ for the gas mixture used and the electron charge e. The ions per primary electron were calculated as $G_{ion} = I_C/(Rn_pe)$ with the current I_C collected at the drift cathode. The ions per primary electron are dubbed the *ion gain* for the sake of easier reading. The *ion back-flow* $IBF = I_C/I_A$ is defined as the ratio of the currents read from the cathode and the anode.
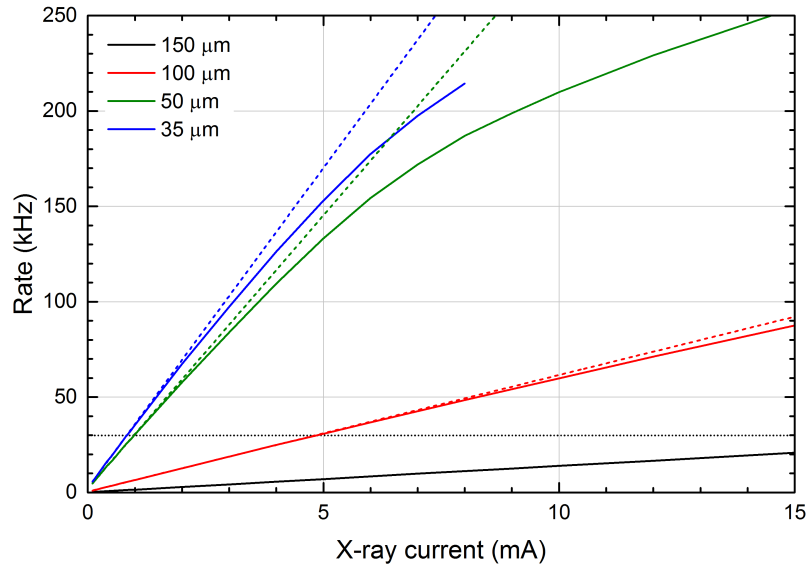

Figure 3.5: Measured interaction rate for different copper absorber thickness depending on the X-ray tube current. A linear fit (dashed) was done using data points up to a rate of $30\,\mathrm{kHz/mm^2}$ (dotted line) until which a linear correlation between rate and current was found.

The flux was measured by using collimators of known diameter and measuring the X-ray rate with a discriminator. For high rates the discriminator saturates due to pile-up, as shown in figure 3.5. There are two ways to overcome this problem:

- Using a linear fit. The X-ray flux is linear as a function of the current supplied to the

X-ray tube. The rate is measured at a range where the discriminator is not saturated, and is then plotted versus the X-ray tube current. A linear function is then fit into this plot and extended to cover the full range of the X-ray tube currents used.

- Using absorbers. Absorbers are first calibrated using smaller X-ray fluxes. By comparing the rate measured with and without absorber the attenuation coefficients of the absorbers are defined. When studying the effects of high charge densities, first measurements are taken without absorbers and the currents of all stages, i.e. drift cathode, GEM electrodes and readout anode, are noted. The measurements are then repeated a second time with absorbers to measure the rate with absorbers. These are then used to calculate the flux of the previous measurement with known attenuation coefficients.

The flux was measured using a mixture of both methods. For low X-ray fluxes the rates were measured directly. For intermediate X-ray fluxes achieved with thick absorbers the first method was used to extrapolate the rate at high X-ray tube currents. For higher X-ray fluxes achieved with thin absorbers the second method was used.
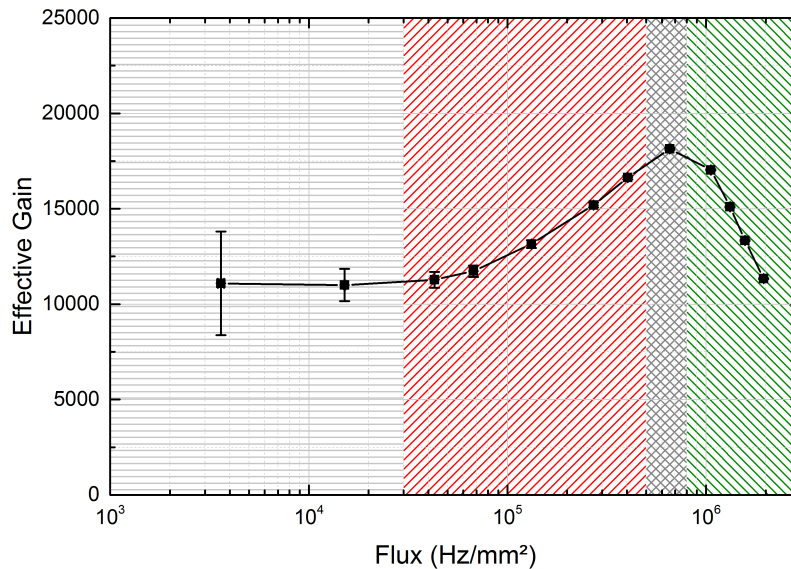
3.2.3 Example of the observed effects

Figure 3.6: Effective gain depening on the X-ray flux for a *nominal* effective gain of 10×10^3.

Figure 3.6 shows an example of the behaviour of a triple-GEM's effective gain depending on the X-ray flux. All curves presented in this chapter will show a similar behaviour. A dependence of the curve's shape on the individual fields applied to each electrode will be presented in the following sections.

The detector in this example was operated at a *nominal* effective gain of approximately 10^4.

This nominal value was reached by applying potential differences of 400 V, 360 V and 320 V between the top and bottom electrode of the first, second and third GEM respectively. The *Drift* field was set to 2 kV/cm, the *Transfer 1*, the *Transfer 2* and the *Induction* field were set to 3.6 kV/cm each. The voltages applied to each electrode were kept at a constant value by the used power supply.

The detector first operates at a *stable* effective gain, ranging from low flux to about 30 kHz/mm^2 (horizontal pattern). The effective gain is constant and at the nominal value expected by the voltages applied to the electrodes of the detector. For higher fluxes up to approximately 0.5 MHz/mm^2 (upward pattern) the effective gain *increases* as a function of the flux. The effective gain then reaches a *plateau* which goes on until about 0.8 MHz/mm^2 (criss-cross pattern). Here the effective gain only slowly increases and then decreases again. Once the flux is higher (downward pattern) the effective gain strongly *decreases* again.
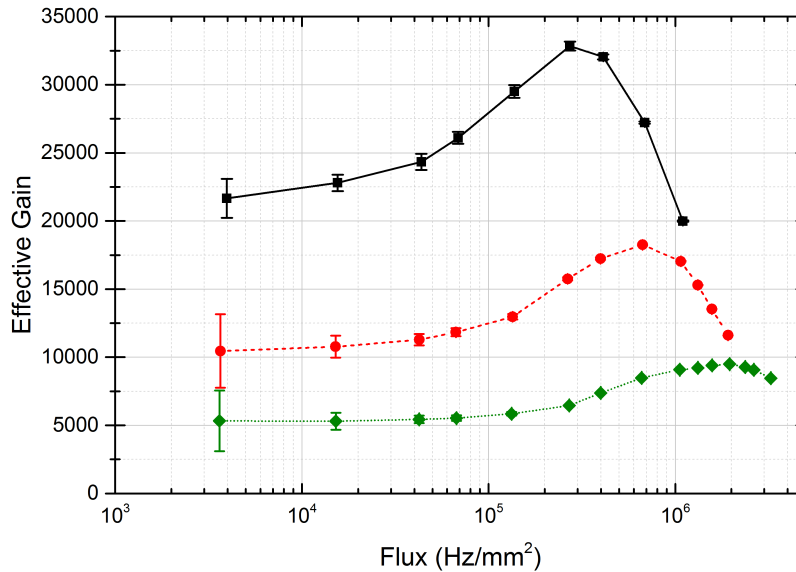
3.2.4 Dependence on the effective gain

Figure 3.7: Effective gain depending on the X-ray flux for *nominal* effective gains of 5×10^3 (dotted), 10×10^3 (dashed), and 20×10^3 (solid).

Effective gain curves were acquired for *nominal* effective gains of approximately 5×10^3, 10×10^3 and 20×10^3 (figure 3.7). The *Drift* field was kept constant at 2 kV/cm and the other transfer fields at 3.6 kV/cm. The variations of *nominal* effective gain were reached by changing the voltages across all three GEMs, with GEM 1 at 410 V, 400 V and 390 V, GEM 2 at 370 V, 360 V and 350 V, and GEM 3 at 330 V, 320 V and 310 V for highest to lowest gain studied.

The dependence of the effective gain on the onset of space-charge induced variations can

be seen in figure 3.7: for higher *nominal* effective gains the effect appears at lower X-ray flux, with the increase being steeper. As explained in section 3.1, the magnitude of the field distortions depends on the number of ions generated and accumulating in the detector. For a higher *nominal* effective gain of about 20×10^3 the number of ions in the detector volume is larger when compared to a detector operated at 10×10^3 or 5×10^3.

When comparing the curve for a *nominal* effective gain of 20×10^3 with the other two, it is evident that there is already a slight increase of effective gain at a flux below $10 \, \text{kHz/mm}^2$. This effect is due to space-charge effects influencing detectors at this already considerably large X-ray fluxes if they are operated at high gain. The plateau of the curve is stretched over a larger range of X-ray fluxes for lower gains. Additionally, the decrease of effective gain is not as steep as those at higher *nominal* values, even though the relative increase of effective gain is larger.

3.2.5   Dependence on individual fields

To identify the origin of the increase and decrease of effective gain, the influence of field variations on the observed effect was studied.

One of the transfer fields was varied, while the other three transfer fields and the amplification fields were kept constant at $E_D = 1.5 \, \text{kV/cm}$, $E_{T1} = 3.6 \, \text{kV/cm}$, $E_{T2} = 3.6 \, \text{kV/cm}$, and $E_I = 3.6 \, \text{kV/cm}$. The voltages across the GEMs were kept at $V_{GEM1} = 410 \, \text{V}$, $V_{GEM2} = 370 \, \text{V}$ and $V_{GEM3} = 330 \, \text{V}$ for all measurements.

3.2.6   Drift field variation

With the *Transfer 1* field and the potential difference across GEM 1 kept constant, the collection efficiency of the first GEM depends on the *Drift* field. For low fields electrons are lost due to attachment, for high fields they end up on the top electrode of the first GEM. Changing the *Drift* field therefore modifies the number of electrons available for the first step of electron multiplication as well as the number of electrons introduced into the *Transfer 1* gap. In total numbers of electrons available from this stage onward, both the effects of reduced collection efficiency and electron attachment *at small X-ray flux* can be regarded as equal.

The *Drift* field was varied from $0.1 \, \text{kV/cm}$ to $5 \, \text{kV/cm}$, thus studying the effect for full collection efficiency, as well as reduced effective gain due to the two effects described.

Plotting the effective gain versus the particle flux (Fig. 3.8) shows three different regions: *stable* operation up to X-ray fluxes of approximately $2 \times 10^4 \, \text{Hz/mm}^2$, an *increase* of the effective gain up to X-ray fluxes of about $3 \times 10^5 \, \text{Hz/mm}^2$ to $6 \times 10^5 \, \text{Hz/mm}^2$ and a *decrease* of the effective gain starting between $3 \times 10^5 \, \text{Hz/mm}^2$ and $6 \times 10^5 \, \text{Hz/mm}^2$. The behaviours are different for low fields resulting in electron attachment (red curves), medium fields with full collection efficiency (black curves), and high fields with reduced collection efficiency (green
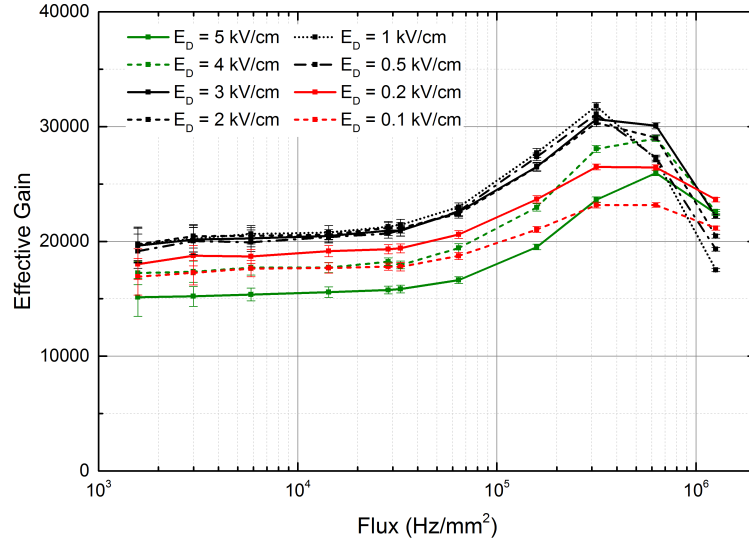
Figure 3.8: Dependence of the effective gain on the X-ray flux for different *Drift* fields E_D. Other transfer fields were kept constant at $E_{T1} = E_{T2} = E_I = 3.6\,\text{kV/cm}$. GEM voltages were kept constant at $V_{GEM1} = 410\,\text{V}$, $V_{GEM2} = 370\,\text{V}$ and $V_{GEM3} = 330\,\text{V}$.
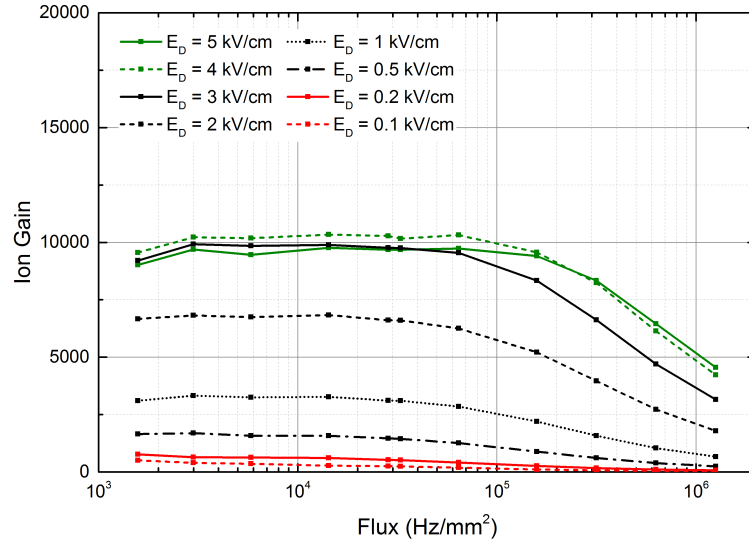

Figure 3.9: Dependence of the ion gain on the X-ray flux for different *Drift* fields E_D. Other transfer fields were kept constant at $E_{T1} = E_{T2} = E_I = 3.6\,\text{kV/cm}$. GEM voltages were kept constant at $V_{GEM1} = 410\,\text{V}$, $V_{GEM2} = 370\,\text{V}$ and $V_{GEM3} = 330\,\text{V}$.

curves).

The ion gain (Figure 3.9) is stable up to the same flux for all fields studied, except for the ones with reduced collection efficiency. Here the effective gain is stable up to fluxes of about $60\,\mathrm{kHz/mm^2}$. As discussed in section 3.1.1, the fields are changed due to ion space-charge in all the regions. Since the ion extraction scales with the field applied above a GEM, it can be assumed that for the higher initial *Drift* fields the space-charge effects don't reduce the ion extraction as fast as with the lower fields studied. Judging from the lower *nominal* effective gain for those two curves in figure 3.8, higher fluxes are needed to reach the same field reduction due to accumulation of ions.
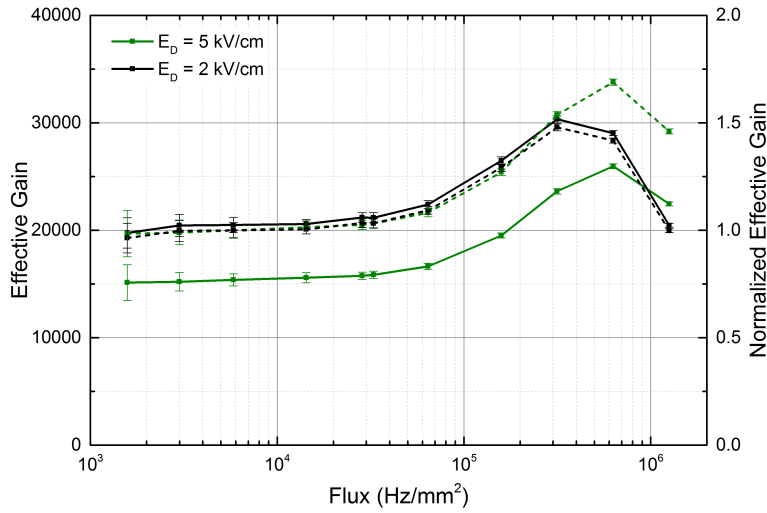

Figure 3.10: Effective gains (solid) and normalized effective gains (dashed) for *Drift* fields of $2\,\mathrm{kV/cm}$ (black) and $5\,\mathrm{kV/cm}$ (green).

Figure 3.10 shows two curves of figure 3.8, one acquired for a *Drift* field of $2\,\mathrm{kV/cm}$ (black) and the other for $5\,\mathrm{kV/cm}$ (green). Even though the *nominal* effective gain is different for both settings, the behaviour is approximately the same up to an X-ray flux of about $100\,\mathrm{kHz/mm^2}$. While the curve for the lower *Drift* field then reaches a *peak* at around $300\,\mathrm{kHz/mm^2}$ and 150% of the nominal value, the other curve exhibits an increase of effective gain to a flux of approximately $500\,\mathrm{kHz/mm^2}$ before seeing a decrease. At the same time, the relative increase to around 170% of the *nominal* effective gain is larger for the setting with higher *Drift* field.

Figure 3.11 shows the two curves for *Drift* fields of of $0.1\,\mathrm{kV/cm}$ (red) and $4\,\mathrm{kV/cm}$ (green). Even though at the same *nominal* effective gain of about $17{\times}10^3$, the curves show different behaviour both for the increase and the decrease of effective gain. Both curves show a stable effective gain up to approximately the same range of X-ray fluxes. The plateau of the curve is reached at lower flux for the higher *Drift* field. The relative change is about 60% for higher field, as compared to around 30% for the lower field, with both a steeper increase
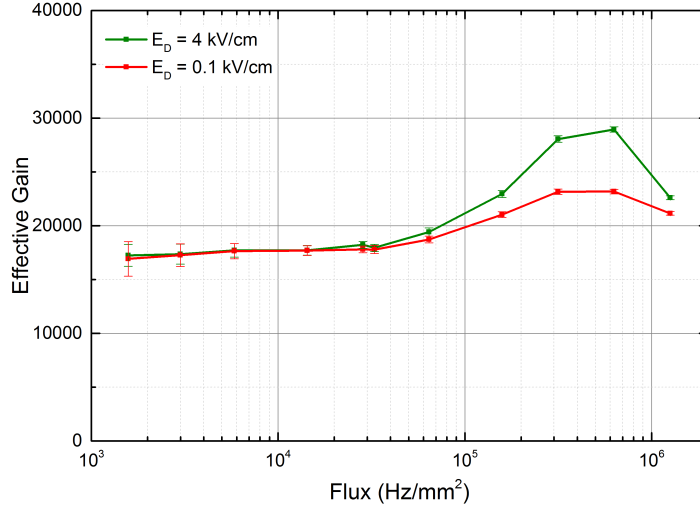
Figure 3.11: Effective gains for *Drift* fields of $0.1\,\text{kV/cm}$ (red) and $4\,\text{kV/cm}$ (green).

and decrease. Knowing that the same amount of electrons reaches the *Transfer 1* gap and following stages of the detector, the difference of the extent of the observed effect has to be attributed mainly to changes in the *Drift* field. Comparing the initial effective gains for different fields in figure 2.15 and assuming a decrease of the field due to ions accumulating in the *Drift* volume, there is only a slight decrease of collection efficiency for an initial *Drift* field of $0.1\,\text{kV/cm}$ and a comparably larger increase for a field of $4\,\text{kV/cm}$.

The same conclusion can be drawn for figure 3.10: the reduction of the *Drift* field from its nominal value of $2\,\text{kV/cm}$ leads to no change in electron collection efficiency, while there is still a large margin for an increase of efficiency when operating the detector at a *Drift* field of $5\,\text{kV/cm}$.

3.2.7 Induction field variation

Changing the *Induction* field governs the extraction efficiency of the last GEM. A high *Induction* field leads to an increased extraction of electrons and thus a higher effective gain.

In figure 3.12 an increase of effective gain is observable for *Induction* fields of $1\,\text{kV/cm}$ or higher, with a decrease of effective gain only appearing at fields of $0.5\,\text{kV/cm}$.

When calculating the *total gain* as the sum of currents read from both the anode and the bottom electrode of GEM 3, it is evident that the observed effect originates mainly from a sharing of charge between those two electrodes. Reducing the *Induction* field leads to an increasing number of field lines ending up at the bottom electrode of GEM 3. Electrons from the GEM holes following those field lines are not collected on the anode but rather on this electrode, as has been shown in figure 2.13 of section 2.5.4. The dependence of the *total gain* on the X-ray flux can be seen figure 3.13. The previously shown strong variations for different
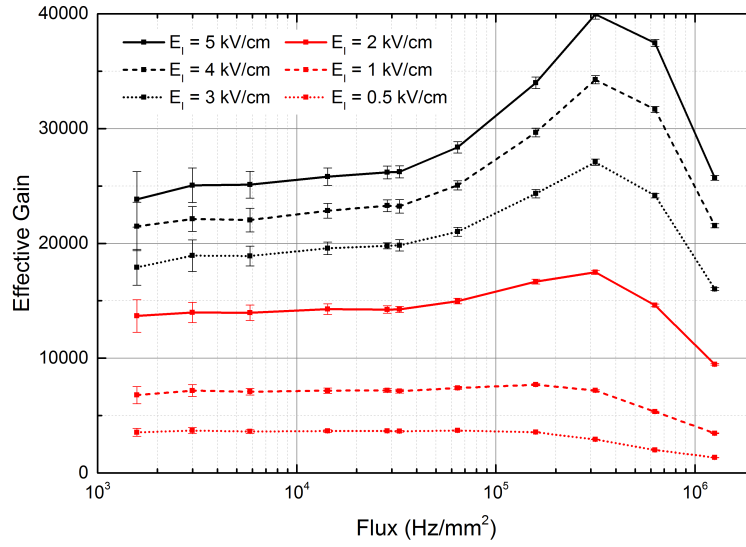
Figure 3.12: Dependence of the effective gain on the X-ray flux for different *Induction* fields E_I. The other transfer fields were kept constant at $E_D = 1.5\,\text{kV/cm}$ and $E_{T1} = E_{T2} = 3.6\,\text{kV/cm}$. GEM voltages were kept constant at $\text{V}_{GEM1} = 410\,\text{V}$, $\text{V}_{GEM2} = 370\,\text{V}$ and $\text{V}_{GEM3} = 330\,\text{V}$.
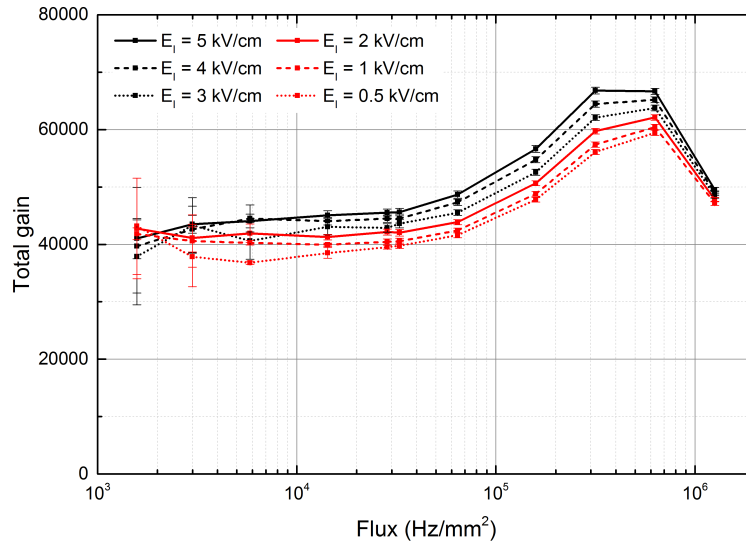

Figure 3.13: Dependence of the total gain for different *Induction* fields when taking charge sharing between the bottom electrode of third GEM and the read-out anode into account. The total gain $G_{tot} = (I_{G3B} + I_A)/(Rn_p e)$ was calculated with the sum of currents read from the bottom electrode of the third GEM I_{G3B} and the read-out anode I_A.

Induction fields can not be observed. The differences in *nominal* effective gain are due to the *Induction* field extending into the GEM holes. The fields in the holes are therefore slightly increased for higher *Induction* fields. This leads to a larger amplification and thus a higher *nominal* effective gain. Due to the higher gain, more ions drift back into the stages above the third GEM. The increase of effective gain can therefore be observed at lower X-ray flux for larger *Induction* fields.
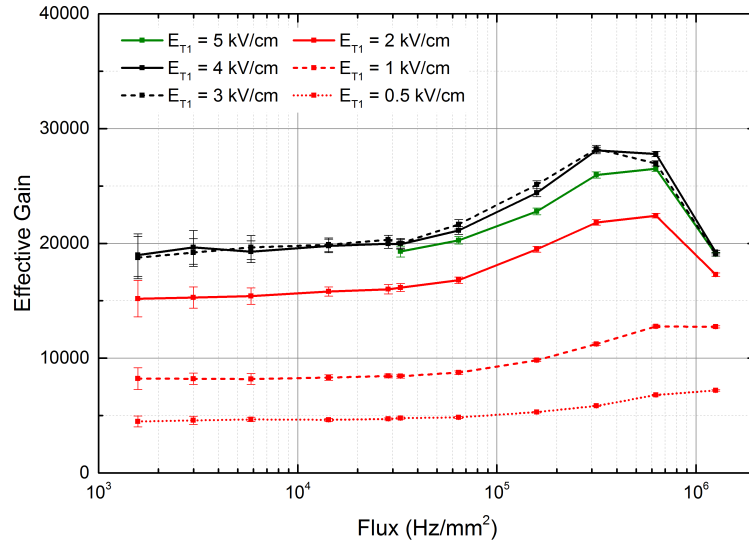
3.2.8   Transfer 1 field variation

Figure 3.14: Dependence of the effective gain on the X-ray flux for different *Transfer 1* fields E_{T1}. Other transfer fields were kept constant at $E_D = 1.5\,\text{kV/cm}$ and $E_{T2} = E_I = 3.6\,\text{kV/cm}$. GEM voltages were kept constant at $V_{GEM1} = 410\,\text{V}$, $V_{GEM2} = 370\,\text{V}$ and $V_{GEM3} = 330\,\text{V}$. Data points for $E_{T1} = 5.0\,\text{kV/cm}$ are partly omitted due to charging-up of the GEM foils.

The variation of the *Drift* field in section 3.2.6 already demonstrated the field distortions and resulting changes of the collection efficiency of the first GEM.
Changing the *Transfer 1* field influences the extraction efficiency of the first GEM but additionally also the collection efficiency of the second GEM. The *Transfer 1* field was varied from $0.5\,\text{kV/cm}$ to $5\,\text{kV/cm}$. The dependence of the extraction efficiency of the first GEM on the *Transfer 1* field behaves in every way as the curve for the *Induction* field shown in figure 2.15. The extraction efficiency is increased by a factor of five when comparing the lowest and highest *Transfer 1* field. The collection efficiency of the second GEM on the other hand behaves like the curve of the *Drift* field shown in figure 2.15. The collection efficiency is slightly reduced for low fields, stable up to 3kV/cm and then reduced for higher fields. Figure 3.14 confirms this picture. Low *Transfer 1* fields lead to a lower *nominal* effective gain. *Transfer 1* fields of $3\,\text{kV/cm}$ and $4\,\text{kV/cm}$ yield the same *nominal* effective gain because the
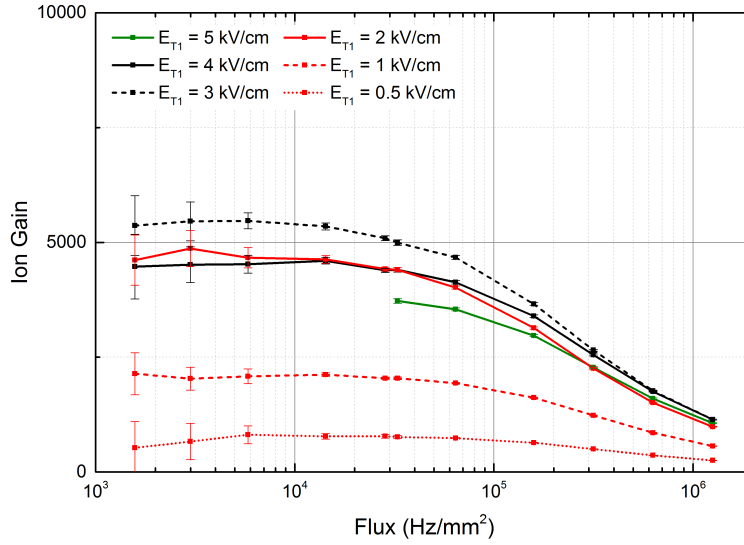
Figure 3.15: Dependence of the ion gain on the X-ray flux for different *Transfer 1* fields E_{T1}. Other transfer fields were kept constant at $E_D = 1.5\,\text{kV/cm}$ and $E_{T2} = E_I = 3.6\,\text{kV/cm}$. GEM voltages were kept constant at $\text{V}_{GEM1} = 410\,\text{V}$, $\text{V}_{GEM2} = 370\,\text{V}$ and $\text{V}_{GEM3} = 330\,\text{V}$. Data points for $E_{T1} = 5.0\,\text{kV/cm}$ are partly omitted due to charging-up of the GEM foils.

higher extraction efficiency is compensated by the lower collection efficiency. For the highest *Transfer 1* field the reduced collection efficiency leads to a lower effective gain.

The behaviour of figure 3.14 is comparable to the curves acquired for different effective gains in figure 3.7: for lower *nominal* effective gains the onset of the increase is pushed towards higher X-ray fluxes.

The increase of effective gain is explained by the distortions of the transfer fields between the GEMs. The decrease of ion gain, as shown in figure 3.15 can be attributed to the same effect. With decreasing fields at the top electrodes of the GEMs the ion extraction is reduced. Due to increasing fields at the bottom electrodes of the GEMs the ion collection is decreased. Space-charge effects are therefore *increasing* the *electron* efficiencies while at the same time they are *reducing* the *ion* efficiencies!

Looking at figure 3.16 gives a hint at the mechanism behind the decrease of effective gain: at high X-ray fluxes the ion back-flow reaches a plateau for *Transfer 1* fields of $2\,\text{kV/cm}$ and more. This equal reduction of the number of ions (figure 3.15) and electrons (figure 3.14) reaching the cathode or anode hints towards a decrease of the electron-ion pairs produced during amplification. For *Transfer 1* fields of less than $2\,\text{kV/cm}$ this plateau is not reached for the X-ray fluxes investigated. Additionally, at these fields the effective gain in figure 3.14 does not yet decrease. The ion gain on the other hand is further reduced due to a change of ion collection and extraction, as can also be seen in the reduced ion back-flow in figure 3.16.
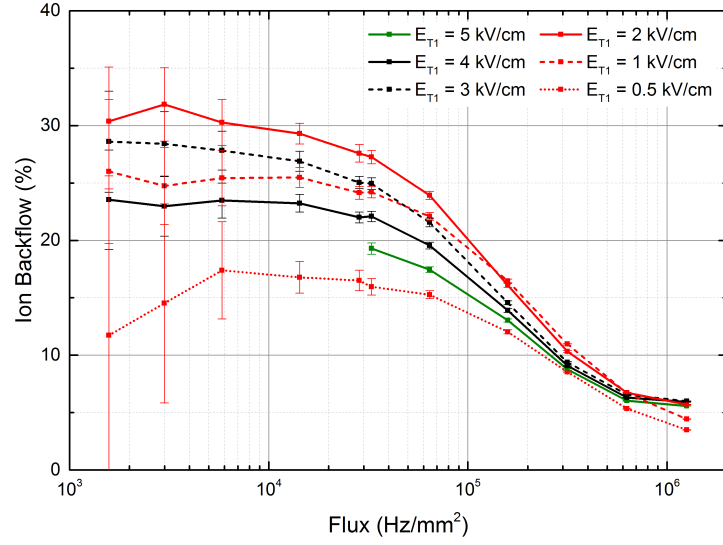
Figure 3.16: Dependence of the ion back-flow on the X-ray flux for different *Transfer 1* fields E_{T1}. Other transfer fields were kept constant at $E_D = 1.5\,\text{kV/cm}$ and $E_{T2} = E_I = 3.6\,\text{kV/cm}$. GEM voltages were kept constant at $\text{V}_{GEM1} = 410\,\text{V}$, $\text{V}_{GEM2} = 370\,\text{V}$ and $\text{V}_{GEM3} = 330\,\text{V}$.
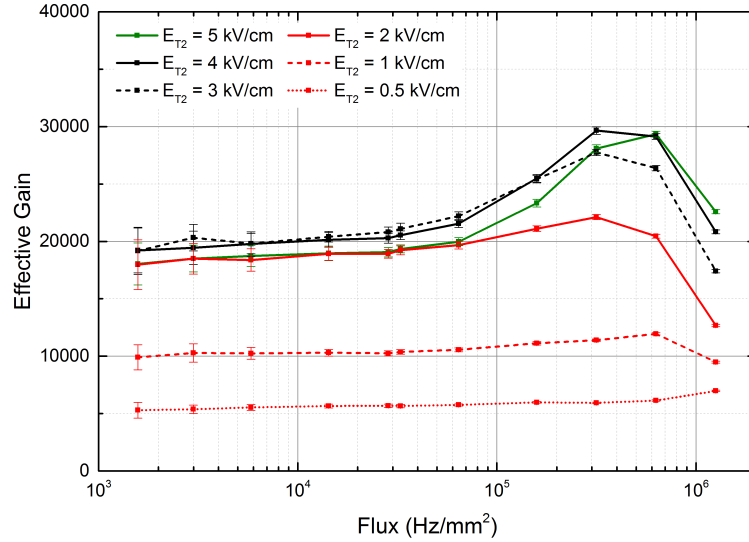
3.2.9 Transfer 2 field variation

Figure 3.17: Dependence of the effective gain on the X-ray flux for different *Transfer 2* fields E_{T2}. Other transfer fields were kept constant at $E_D = 1.5\,\text{kV/cm}$ and $E_{T1} = E_I = 3.6\,\text{kV/cm}$. GEM voltages were kept constant at $\text{V}_{GEM1} = 410\,\text{V}$, $\text{V}_{GEM2} = 370\,\text{V}$ and $\text{V}_{GEM3} = 330\,\text{V}$.

Figure 3.17 shows the dependence of the effective gain on the X-ray flux for different *Transfer 2* fields. As is expected from previous measurements, the onset of the increased effective gain is again pushed towards higher X-ray fluxes for reduced *nominal* effective gains

(red curves).

There is again a different behaviour for curves of the same *nominal* effective gain, but with different *Transfer 2* fields of $2\,\mathrm{kV/cm}$ and $5\,\mathrm{kV/cm}$ (solid red and solid green). Again, the electron collection and extraction efficiencies behave like the effective gain for varying *Drift* and *Induction* fields shown in figure 2.15. For a high *Transfer 2* field the collection efficiency of GEM 3 can be considerably increased due to ion space-charge, as well as the extraction efficiency of GEM 2. For a low *Transfer 2* field only the extraction efficiency can be substantially increased. The collection efficiency of GEM 3 might even be reduced if the field distortions are too large.

The decrease of effective gain can again be explained by the decrease of the amplification fields, hence a decrease of electron multiplication. The results indicate that the decrease of the amplification fields doesn't only occur once the plateau of the gain curve is reached, as was previously assumed. While the transfer fields still increase, the amplification fields already start decreasing. On the rising slope of the curve the first effect is more dominant than the other one. On the falling slope there is still an increase of collection and extraction efficiencies, but the decrease of amplification becomes more dominant. For a *Transfer 2* field of $2\,\mathrm{kV/cm}$ there is almost no increase of efficiencies compensating the reduced amplification. The decrease of effective gain is therefore much stronger than for the other curves.

3.2.10   Dependence on the GEM voltages

Figure 3.18 shows the dependence of the effective gain on the X-ray flux for various voltages applied across the third GEM, with all the other transfer fields and amplification fields kept constant. The third GEM, acting as the largest ion generator in the volume, yields the greatest contribution to the ion space-charge found within the detector.

In figure 3.19 the dependence of the effective gain on the X-ray flux is shown for equal *nominal* effective gains at different voltages applied across individual GEMs. The sum of voltages across the GEMs are kept constant at $1080\,\mathrm{V}$ (solid) and $1070\,\mathrm{V}$ (dashed) for the curves shown, with either the first or the third GEM operated at reduced potential differences.

Even though the amount of charge within the detector is the same for low X-ray flux, for higher fluxes the field distortions are stronger if mainly the third GEM contributes to the creation of ions. The reason for this is to be found in the number of ions drifting back into the volume on top of the GEM: for the first case, the greatest amplification occurs in the first GEM with the highest relative but low absolute number of ions drifting back into the conversion volume; for the second case a lower relative but very high absolute number of ions is drifting back into the *Transfer 2* volume and consequently all the volumes prior to that stage.
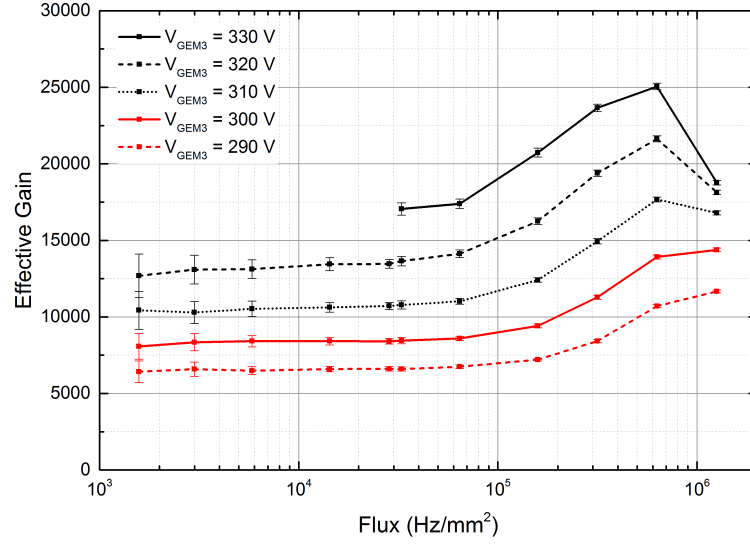
Figure 3.18: Effective gain depending on the X-ray flux for different GEM 3 voltages, ranging from 330 V to 290 V in steps of 10 V. The other GEM voltages were $V_{GEM1} = 410$ V and $V_{GEM2} = 370$ V. The transfer fields were kept constant at $E_D = 1.5$ kV/cm and $E_{T1} = E_{T2} = E_I = 3.6$ kV/cm. Parts of the curve for $V_{GEM3} = 330$ V are omitted due to errors during data acquisition.
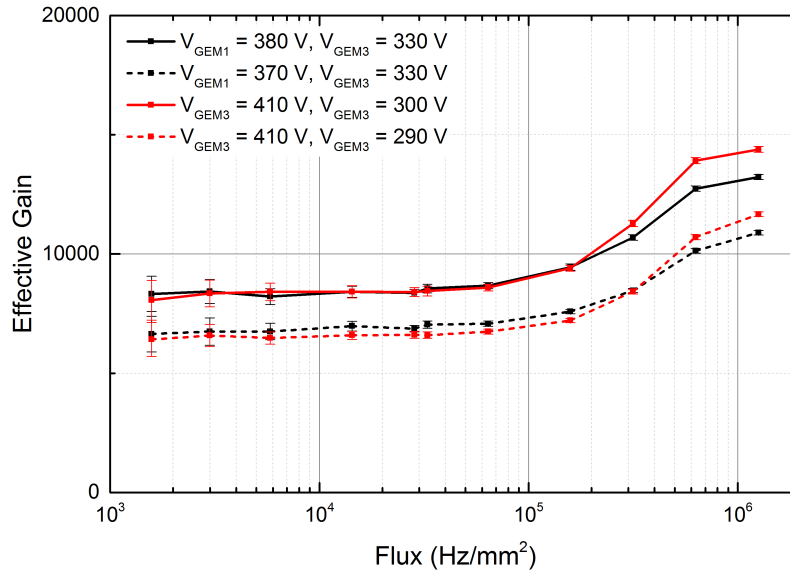

Figure 3.19: Effective gain depending on the X-ray flux for different GEM voltages. The black curves show GEM 1 voltages of 380 V and 370 V, the red ones GEM 3 voltages of 300 V and 290 V. The voltages applied to the other GEMs were $V_{GEM1} = 410$ V, $V_{GEM2} = 370$ V and $V_{GEM3} = 330$ V. The transfer fields were kept constant at $E_D = 1.5$ kV/cm and $E_{T1} = E_{T2} = E_I = 3.6$ kV/cm.

3.2.11   Simulations

As shown in section 3.1 and confirmed by the measurements presented so far, field distortions
in the transfer gaps lead to an increase of effective gain and distortions in the amplification
gaps lead to a decrease of effective gain. The model used previously assumed uniformly gen-
erated ions drifting in an electric field, which leads to static field distortions. In reality, the
picture is much more complex. The movement of ions generated in the GEM holes leads to
space-charge effects resulting in field distortions. The distorted fields change both the collec-
tion and extraction efficiencies for electrons and ions. The number of electrons collected in
the GEM holes is changing, as well as the number of ions extracted. With a changing number
of ions extracted, the field distortions are also modified, once again having an influence on
the collection and extraction efficiencies, and so on.
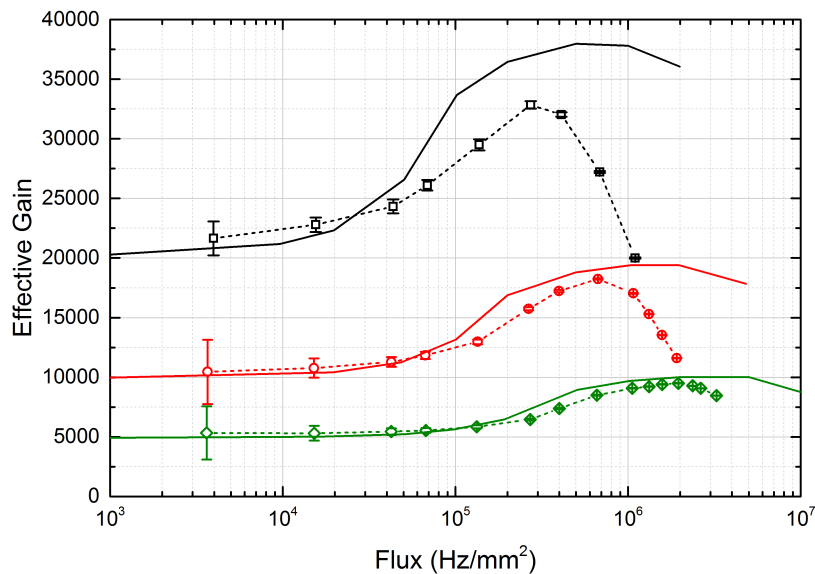This effect can therefore not be solved analytically any more.

Figure 3.20: Computed average effective gain depending on the X-ray flux for *nominal* ef-
fective gains of $5{\times}10^3$ (green), $10{\times}10^3$ (red), and $20{\times}10^3$ (black). Measured effective gains
of figure 3.7 shown as dashed lines.

The behaviour of the triple GEM detector was simulated using the Finite Element Ana-
lysis software package COMSOL Multiphysics® [20]. The electron and ion distributions in the
detector are described macroscopically by numerically approximating the solutions of a set
of partial differential equations of second order. The equations used are Maxwell's first equa-
tion for the potential distribution, and the drift and diffusion equations for electrons and ions.

$$\vec{\nabla} \cdot \varepsilon \vec{\nabla} V = -q_e(\rho_i - \rho_e)$$
$$\frac{\partial \rho_e}{\partial t} = \alpha|\vec{W}_e|\rho_e - \eta|\vec{W}_e|\rho_e - \vec{\nabla} \cdot (\vec{W}_e\rho_e - D_e\vec{\nabla}\rho_e) \tag{3.5}$$
$$\frac{\partial \rho_i}{\partial t} = \alpha|\vec{W}_e|\rho_e - \vec{\nabla} \cdot \vec{W}_i\rho_i$$

Equations 3.5 are solved for the electric potential V, and the spatial distribution of electrons ρ_e or ions ρ_i respectively, with the electron charge q_e and the permittivity ε of the gas, the electron drift velocity $\vec{W}_e$ and diffusion tensor D_e, the first Townsend coefficient α and the attachment coefficient η, which are all dependent on the electric field. Electron transport coefficients in an Ar/CO_2 70/30 gas mixture are computed using Magboltz 8.97 [37], and the amplification is calculated with the Townsend coefficient corrected for Penning transfer [38]. The ion mobilities are taken from [39]. The model and mathematical formulation is modified from [40] to include the movement of ions.

Due to the computational power needed, a two-dimensional axial-symmetric geometry is used to simulate the effect in a triple GEM detector. The modelled GEMs therefore only contain a single GEM hole, with the holes of all three GEMs perfectly aligned and no asymmetries in the ϕ-coordinate taken into account.

The simulated effective gain as a function of the X-ray flux can be seen in figure 3.20. It is qualitatively comparable to the measurements presented so far. Deviations at very large X-ray fluxes are mostly owed to the stochastic nature of the arrival time of the X-rays, which is not taken into account in these simulations. The primary charge in each simulation is created with equidistant times between each event. In a real detector the time between two events is distributed exponentially. Measurements of this behaviour will be presented and discussed in section 3.4.

The ions created in the GEM holes during the electron avalanches drift upward into the transfer and conversion volumes. The dynamic equilibrium of production and evacuation results in an increased number of positive ions in these volumes, as shown in figure 3.21. This leads to a steady space-charge distribution that modifies the electric field. The fields get distorted in a way that the fields close to the top of the GEM electrodes are reduced and the fields close to the bottom electrodes are increased, as calculated in figure 3.22. The average field over the full length of the gap equals the nominal field applied within the respective volume. The effect becomes stronger for each successive stage of amplification, with the smallest distortion in the *Drift* gap and the largest in the *Transfer 2* gap, for the field configurations used. The distortions in the *Induction* gap are minimal due to an absence of ions in this region. As discussed before, the electrons are moving faster than the ions and their effect is negligible. As explained previously, the electron collection efficiencies and extraction efficiencies of a GEM operated at a fixed potential difference strongly depend on the fields applied above and below the GEM, respectively. Due to the field distortions both
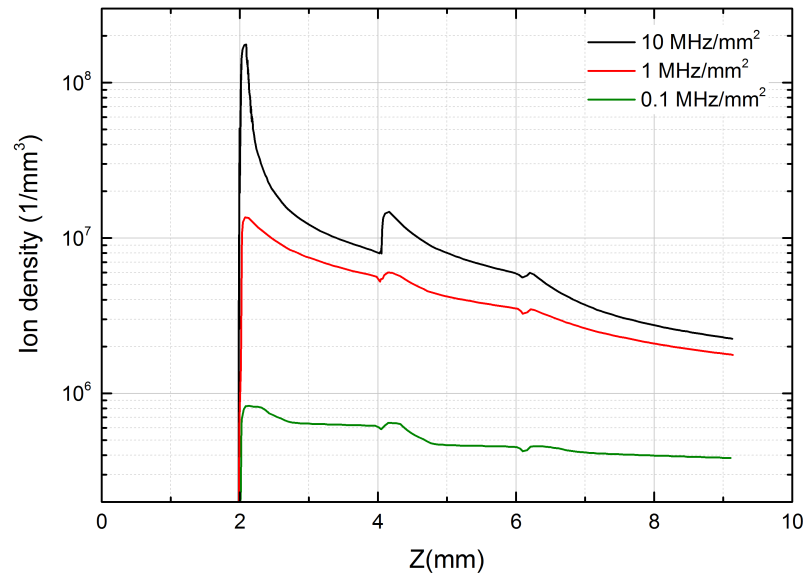
Figure 3.21: Computation of the ion concentrations in the detector for X-ray fluxes of $0.1\,\mathrm{MHz/mm^2}$ (red), $1\,\mathrm{MHz/mm^2}$ (green) and $10\,\mathrm{MHz/mm^2}$ (blue) along the hole axis.
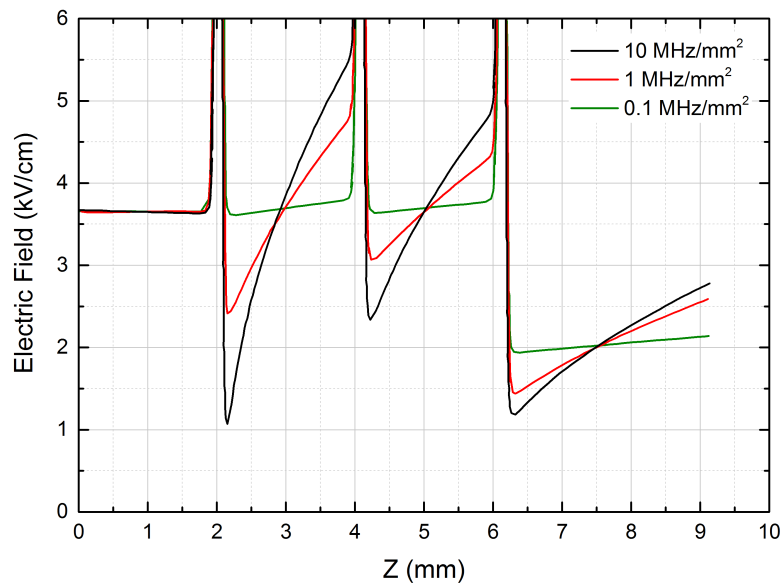
Figure 3.22: Computation of the field distortions in the transfer gaps for X-ray fluxes of $0.1\,\mathrm{MHz/mm^2}$ (red), $1\,\mathrm{MHz/mm^2}$ (green) and $10\,\mathrm{MHz/mm^2}$ (blue) along the hole axis. The *nominal* fields are $2\,\mathrm{kV/cm}$ in the *Drift* gap and $3.5\,\mathrm{kV/cm}$ in the other gaps.

the collection and extraction efficiencies for electrons are increased. With the efficiencies for electrons not at their maximum for the nominal fields applied, this leads to an observable increase of effective gain up to the point where the collection and extraction efficiencies reach close to - but not yet - its maximum (this effect is observed and confirmed in section 3.4.2). At the same time the collection and extraction efficiencies for ions are decreased. This results in a significant reduction of the ion back-flow and ion gain.

The initial slow rise of the effective gain in figure 3.20 can be explained as following: the highest charge-density is first and foremost reached in the *Transfer 2* volume, since the number of electron-ion pairs generated in the last step of amplification is the greatest in number. The first stage with increased electron collection efficiency is the third GEM, with the second GEM just above the *Transfer 2* volume having a higher extraction efficiency. With larger ion densities across the whole detector, the second GEM's electron collection efficiency also increases, with the first GEM following suit. While the first GEM starts undergoing an increase of efficiency, the third GEM's is already at its maximum, thus a flattening of the curve occurs.
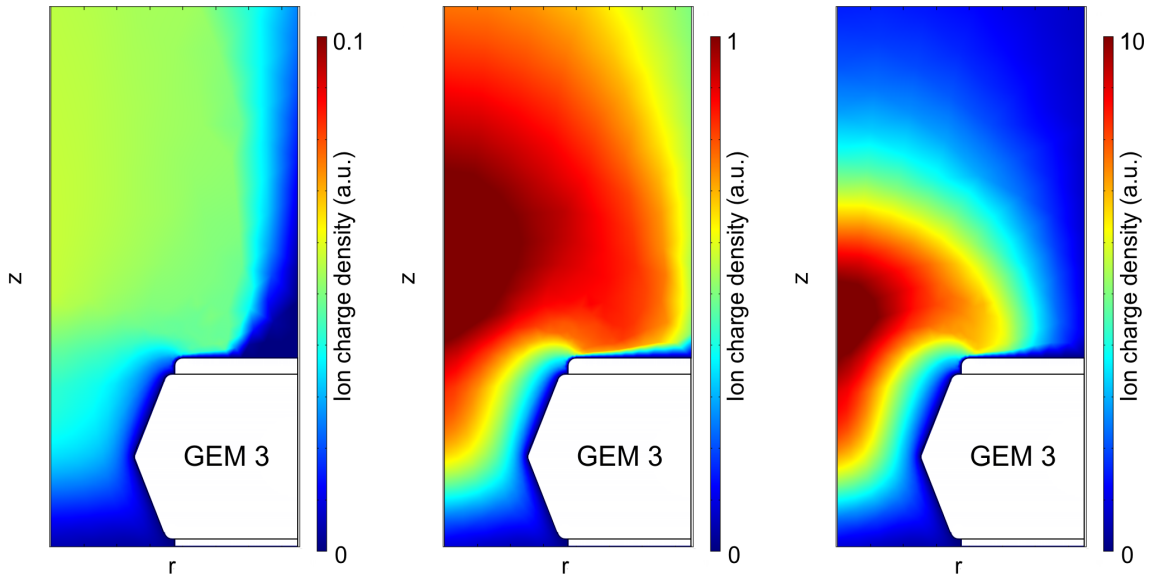

Figure 3.23: Computation of the ion charge density close to the bottommost GEM for X-ray fluxes of $0.1\,\mathrm{MHz/mm^2}$ (left), $1\,\mathrm{MHz/mm^2}$ (center) and $10\,\mathrm{MHz/mm^2}$ (right) along the hole axis.

On the peak of the effective gain curve space-charge effects in the amplification regions become more dominant. With the ion velocity strongly depending on the field, and the field significantly reduced in close vicinity to the GEM holes, the ions start accumulating close to the top of the GEM holes. As can be seen in figure 3.23 the ion density close to the GEM holes is larger than in the rest of the volume. Due to the presence of these ions the fields are further decreased, additionally reducing the ion extraction. Ions generated during an avalanche, or
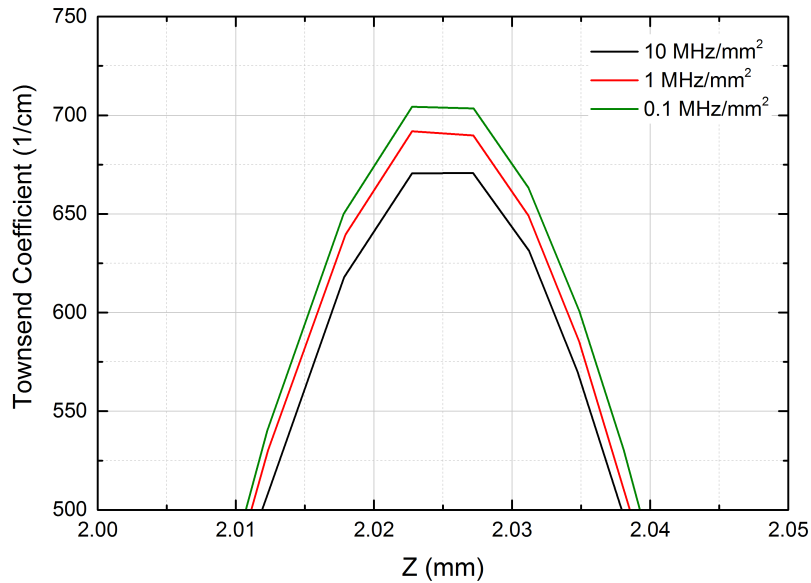
Figure 3.24: Computation of the Townsend coefficient in the holes of the third GEM for X-ray fluxes of $0.1\,\mathrm{MHz/mm^2}$ (red), $1\,\mathrm{MHz/mm^2}$ (green) and $10\,\mathrm{MHz/mm^2}$ (blue).

drifting back from subsequent GEMs, now accumulate in the GEM holes, thus reducing the fields and decreasing the effective gain of the detector. This effect is simulated and can be seen in figure 3.24. The ion back-flow reaches a plateau as a result of less electron-ion pairs being produced within the amplification stages.

Once the flux is increased further, the electron collection and extraction efficiencies of the GEM are assumed to be at their maximum. Due to the reduction of fields in the GEM holes the effective gain is significantly dropping. As with other devices which are limited by ion space-charge in the amplification region, the triple-GEM's effective gain will eventually be reduced to zero if the flux is increased.

3.3   The effect in single-stage and double-stage devices

Concluding from the measurements and simulations previously discussed, for double-GEM detectors the increase of effective gain due to positive ion charge densities should be observable, even though less pronounced than for a triple-GEM detector. For very high X-ray fluxes even a decrease of effective gain should be visible.

For single-GEM detectors, only consisting of a conversion volume on top of the GEM and an *Induction* volume below, therefore lacking a transfer region, the picture should be different: First, the field modification of the *Drift* field above the GEM should behave in every way as for all other devices studied, but less pronounced due to the low number of back-drifting ions, as compared to double- and triple-GEM detectors. Secondly, and most important, the field modifications below the GEM, devoid of ions, are non-existent. A modification of the

amplification fields in the GEM holes is expected at high gains and high X-ray fluxes.

3.3.1 Experimental setup

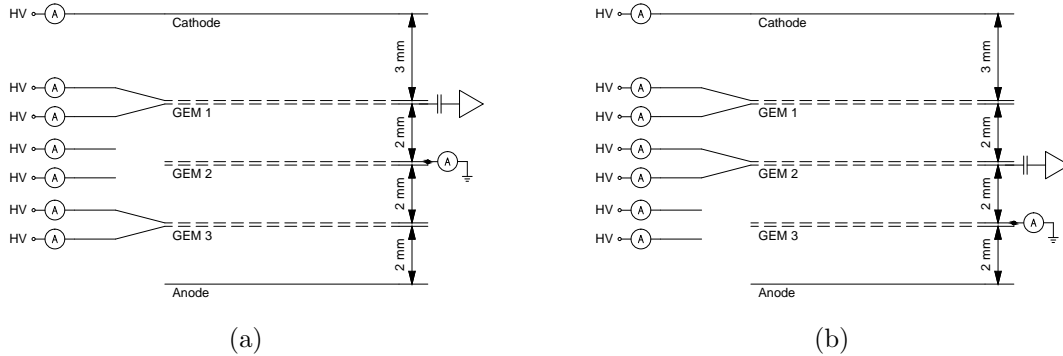(a)   (b)

Figure 3.25: Setup for single-GEM (left), and double-GEM (right) measurements. The *Drift* gap of each setup had a length of three millimetres, with the other gaps kept at two millimetres.

Space-charge effects were investigated in single-GEM and double-GEM detectors. To allow for an easy comparison of the measurements to those done for a triple-GEM detector, the device was kept in place and the charge, originally read out on the anode was read from the top and bottom electrode of one of the subsequent GEM foils simultaneously. The setup for both the single- and double-GEM measurements, as shown in figure 3.25, was modified in two steps: the capacitors of the read-out chain was moved from the third GEM's bottom electrode high-voltage feed through to the feed through of the bottom electrode of one of the GEMs above it. Additionally, the feed throughs of the top and bottom electrode of the respective GEM were shorted and connected to a pico ammeter.

This method has some advantages over using the second and third GEM, or only the third GEM to operate as a double- and single-GEM detector, respectively. First, the detector was not opened, therefore minimizing the risk of detector failure due to physical damages or contaminations. Secondly, the length of the conversion volume was kept at three millimetres, allowing for the same primary charge to be generated in it. Thirdly, the distance between the conversion volume and the X-ray tube was kept constant. Fourthly, no additional absorbers were introduced between the X-ray tube and conversion volume, as would have been the case if one or two GEM foils on top of the *Transfer 1* or *Transfer 2* volume were not used. A disadvantage was the somewhat affected charge collection on the GEM foils. Even though the electrodes were shorted and read simultaneously, a tiny fraction of electrons might get collected on the walls inside the GEM holes, leading to unwanted charging-up effects. This small disadvantage is easily acceptable when compared to the benefits listed above.

The electrodes of the GEM foils and the drift cathode were again powered individually, allowing for a modification of one selected field while keeping the others constant. A copper

X-ray tube and calibrated absorbers were used to irradiate the modified detector with a known X-ray flux. Both the setup and the methods used are already described in sections 3.2.1 and 3.2.2 respectively.
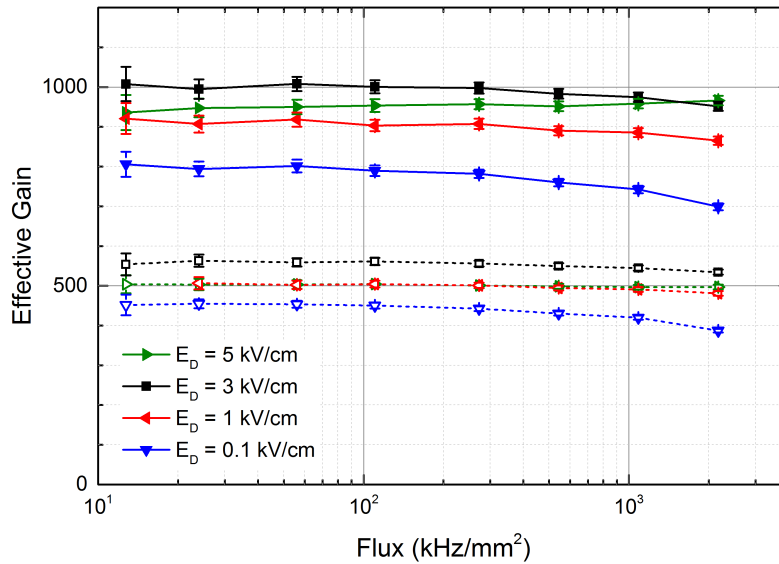
3.3.2   Single GEM

Figure 3.26: Effective gain for a single-GEM detector operated at a *nominal* effective gain of 500 (dashed) and 1000 (solid).
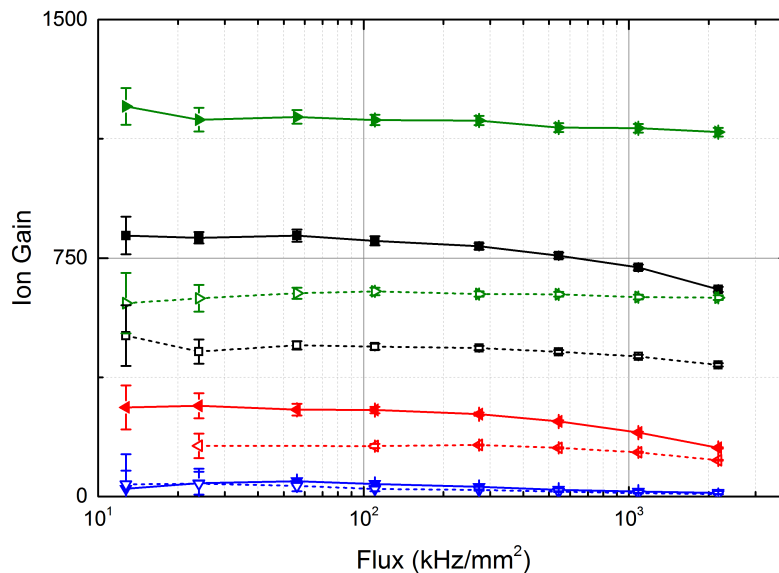

Figure 3.27: Ion gain for a single-GEM detector operated at a *nominal* effective gain of 500 (dashed) and 1000 (solid).

The effective gain of a single-GEM detector was studied for *nominal* effective gains of 500 and 1000. As seen in figure 3.26 the effective gain is stable up to about $100 \, \text{kHz/mm}^2$ for a *nominal* effective gain of 1000, and to approximately $1 \, \text{MHz/mm}^2$ for the *nominal* effective gain set to 500, for most of the *Drift* fields studied. For all fields the effective gain slightly decreases above the values listed, with only the *Drift* field of $5 \, \text{kV/cm}$ showing a different behaviour as it is stable for the lower gain setting and increasing for the higher one. The behaviour of the effective gains at large particle fluxes confirms the observations previously discussed: the *Drift* field is reduced due the ion space-charge and the *Induction* field is not affected. Resulting from the *Drift* field of $E_D = 5 \, \text{kV/cm}$ having a reduced electron collection efficiency, there is an increased effective gain at very high X-ray fluxes. For all cases the effective gain of the detector is reduced at large X-ray fluxes due to ions accumulating in the GEM holes, with the increased electron collection efficiency at $E_D = 5 \, \text{kV/cm}$ compensating the effect. The ion gain on the other hand starts decreasing at a flux of approximately $100 \, \text{kHz/mm}^2$ for all fields studied, as shown in figure 3.27. The reason for this is to be found in the reduced ion extraction efficiency with decreasing fields above the GEM, as was pointed out at the beginning of this chapter.
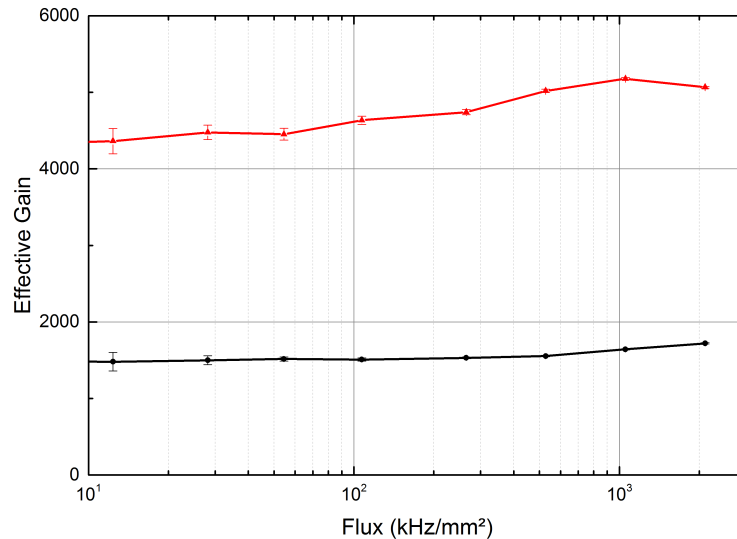
3.3.3   Double GEM

Figure 3.28: Effective gain over particle flux for double-GEM detector. The *nominal* effective gain of the detector was set to $1.5{\times}10^3$ (black) and $4.5{\times}10^3$ (red). The curve for a *nominal* effective gain of $9{\times}10^3$ (green) is omitted. Explanations to be found in the text. The *Drift* field was set to $E_D = 2 \, \text{kV/cm}$ and the other fields to $E_T = E_I = 3.6 \, \text{kV/cm}$.

Effective gain curves were acquired for *nominal* effective gains of $1{\times}10^3$ and $5{\times}10^3$. The curves of effective gain depending on the X-ray flux can be seen in figure 3.28. Both curves

<div align="center">(a)</div>
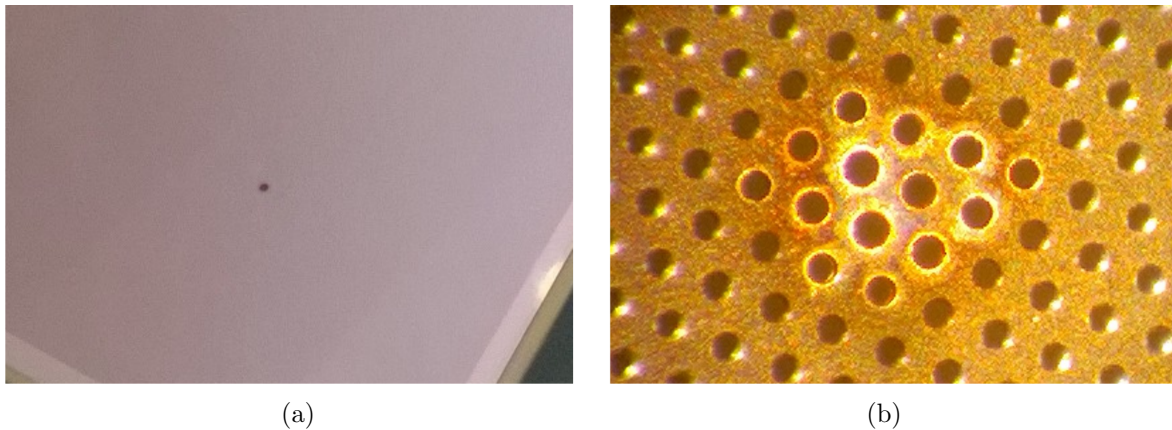

<div align="center">(b)</div>

Figure 3.29: Photograph of the irradiated part of the second GEM of the double-GEM detector. A detail of the affected holes is shown on the right.

show the expected behaviour comparable to a triple-GEM detector operated at lower effective gains. Both the increase and decrease of the effective gain are observable, the proportionate increase of the effective gain however is considerably smaller when compared to a triple-GEM detector: as discussed in the previous sections, the increase of effective gain is the sum of higher collection and extraction efficiencies of *all* GEMs mounted in the detector. Only raising the efficiencies in two instead of three GEMs leads to a proportionally reduced increase of effective gain.

During acquisition of an additional curve for an effective gain of 10×10^3, the detector was found to be severely damaged. The hole diameter was increased by an effect yet to be investigated. Due to the increased hole diameter of the holes affected, the effective gain was permanently reduced. A picture of the damaged area is shown in figure 3.29 (a), with an image of the damaged holes found in 3.29 (b).

3.4 Dependence of the energy resolution on the X-ray flux

The influence of space-charge in the transfer and amplification regions onto the energy resolution, as well as the shape of the pulse height spectra was studied.

3.4.1 Experimental setup

The same setup as for the previous measurements was used, with the pre-amplifier and amplifier replaced by a faster amplifier without charge integration or shaping. Using a *Mini-Circuits R ZKL-1R5+* amplifier [41] in combination with a LeCroy WaveRunner® Xi series oscilloscope [42] allowed the acquisition of signals on an event by event basis even at rates in the order of MHz/mm². As with the previous measurements, the anode current was read out in parallel to allow the calculation of the effective gain.

3.4.2   Methods and measurements

The drawback of using a fast amplifier without charge integration was the considerably lower signal-to-noise ratio. While the slow pre-amplifier and amplifier used at low fluxes allows the discrimination of the signal from the background using a threshold filter, this method could not be employed here. Instead, the signal was separated from the noise with a pulse-width discriminator of the oscilloscope.

The histogram of the signals acquired could not be plotted into a pulse height spectrum directly. Each individual pulse was stored in the memory of the oscilloscope and then analysed offline. The integral of the pulses was calculated, as well as the time difference between individual signals using the time-stamp of the data files.
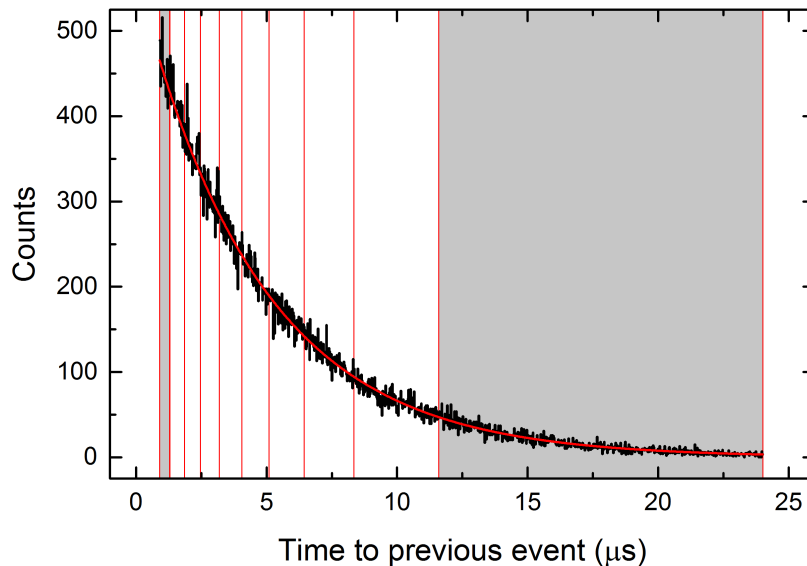

Figure 3.30: Histogram of the integrated signal in dependence of the time to the previous trigger. The histogram was acquired for a *nominal* effective gain of 20×10^3 at an X-ray flux of $270 \, \text{kHz/mm}^2$. The first and the last time interval (grey background) are used to study the impact on the energy resolution.

When plotted into a histogram of the time to the previous event as shown in figure 3.30 it is possible to measure the rate using an exponential fit on the slope of the histogram. Additionally, the instantaneous rate $R_{inst} = n/\Delta t_n$ for each event was calculated by counting the number of triggers n preceding it in a time interval of $\Delta t_n \geq 100 \, \mu\text{s}$, with Δt_n being the time interval between the pulse and the first trigger exceeding the limit of $100 \, \mu\text{s}$. To account for the oscilloscope's dead time of approximately $\tau_d = 0.8 \, \mu\text{s}$ the formula has to be modified to

$$R_{inst} = \frac{n}{\delta t - n\tau_d} \; . \tag{3.6}$$

Resulting from the number of signals per time interval being an integer number, plotting

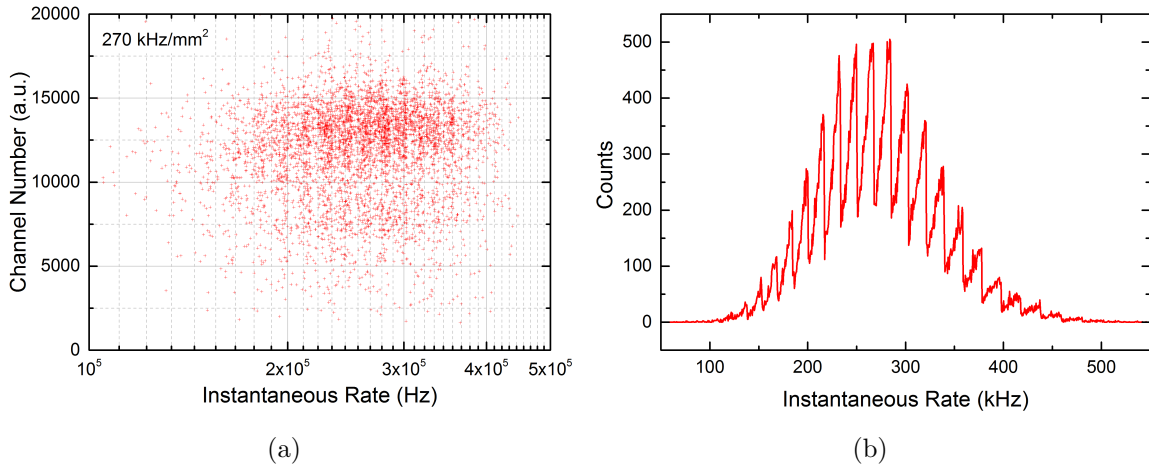(a)   (b)

Figure 3.31: Dependence of the charge integral on the instantaneous rate (a), as shown and described in section 3.4.2 on page 60, and histograms of the instantaneous rate (b). The detector was operated at a *nominal* effective gain of 20×10^3. Plots were acquired for an X-ray flux of $270 \, \text{kHz/mm}^2$.

the charge integrals over the instantaneous rate will lead to a striped pattern as is illustrated in figure 3.31.

Spectra were acquired for *nominal* effective gains of approximately 5×10^3, 10×10^3 and 20×10^3 at the X-ray fluxes (data points) shown in figure 3.7. 10^5 events were acquired for every selected X-ray flux. The phenomena observed will be discussed for the data acquired at a *nominal* effective gain of 20×10^3. For comparison, additional results acquired at lower *nominal* effective gains can be found in appendix A.

3.4.3   Time and flux dependence

Figure 3.32 shows the dependence of the charge integral on the instantaneous rate. The four selected ranges of instantaneous rate are shown in detail in figure 3.33.

For an X-ray flux of $4 \, \text{kHz/mm}^2$ the charge integral seems mostly independent of the instantaneous rate, even though a slight upward trend can be seen at higher rates (fig. 3.33 (a)). At these low rates the number of ions drifting back into the transfer regions don't have a strong impact on the field.
At $140 \, \text{kHz/mm}^2$ a dependence of the charge integral on the instantaneous rate can be observed: the higher the rate, the larger the charge integral (fig. 3.33 (b)). The larger number of ions drifting back into the transfer volumes lead to field distortions. As already described, this results in increased electron collection into, and extraction from the GEM holes. With increased efficiencies, the effective gain of the detector is increasing too.
When reaching the peak of the effective gain curve, a small dependence of the instantaneous rate on the charge integral is visible in the range depicted (figure 3.33 (c)). The back-drifting
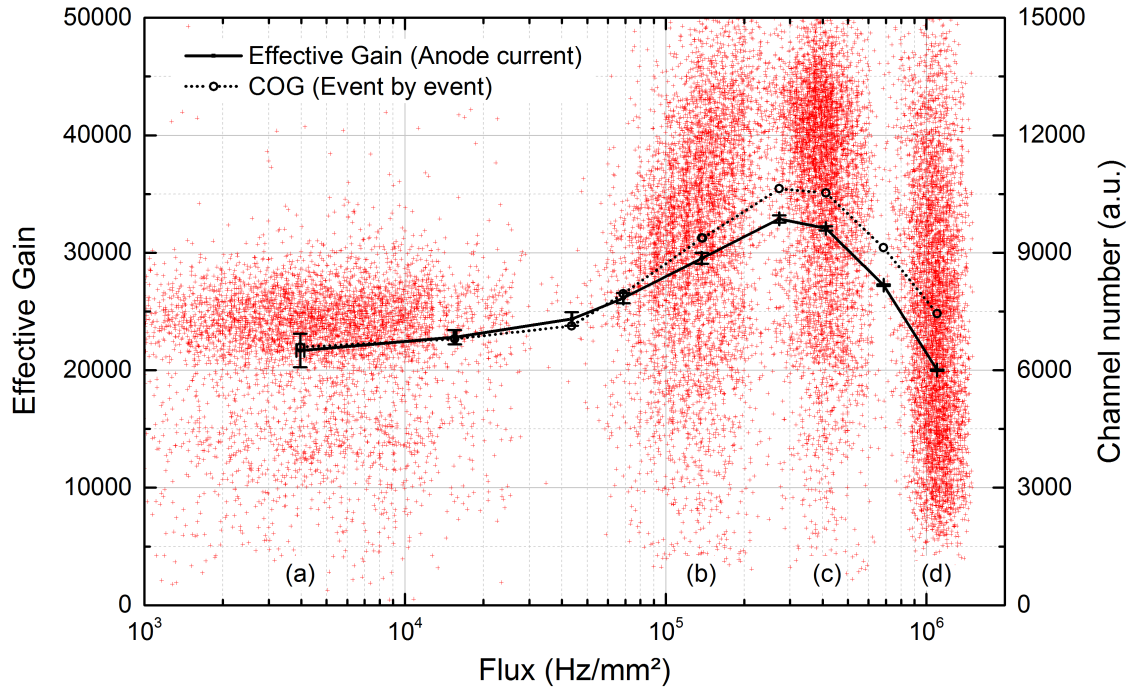
Figure 3.32: Effective gain over particle flux for a *nominal* effective gain of 20×10^3. The effective gain was calculated using the measured anode current as previously described. The secondary axis shows the first 5×10^3 data points for each of the plots in figure 3.33. The centre of gravity was calculated from the full set of data points acquired. The labels refer to the plots in figure 3.33.

ions have increased the collection and extraction efficiencies considerably. Figure 3.32 on the other hand shows the effective gain already slightly decreasing at this flux. The onset of the decrease can not be explained by the instantaneous rate alone.

At $690 \, \text{kHz/mm}^2$ (fig. 3.33 (d)) there is no dependence between charge integral and instantaneous rate any more, with the points evenly distributed over a wide range of instantaneous rates. Again, the observed decrease of the effective gain in figure 3.32 can not be explained by the large number of ions drifting back into the transfer volumes.

Figure 3.34 shows the charge integrals depending on the time to the previous event. The explanation for the decrease of effective gain can be found in figure 3.34(d): there is a clear dependence of the charge integral on the time to the previous event.

Electrons reaching the amplification stage are multiplied in Townsend avalanches. The produced electron-ion pairs result in a larger number of ions drifting towards the cathode. While those ions are still present in the holes or close to the entrance of the holes, new electrons from subsequents events already reach the holes. The multiplication of the electrons will now be affected by the charge of those ions still present. The more ions are close-by, the smaller the amplification field gets, the less electrons are produced in the avalanche. The distance
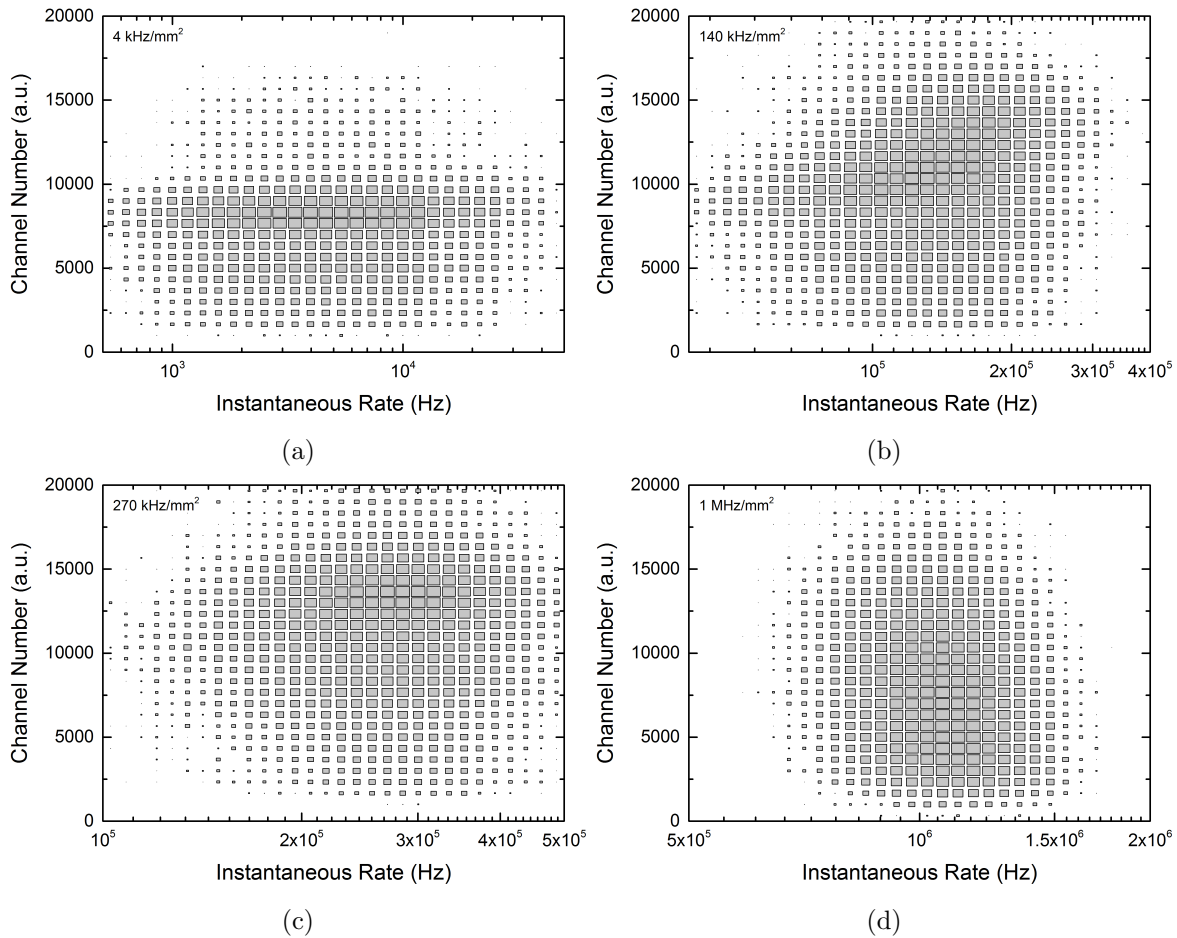
Figure 3.33: Dependence of the charge integral on the instantaneous rate. The plot shows a 2D histogram of the pulses acquired for figure 3.35. The area of each rectangle represents the squared counts per bin and is normalized to the largest number of counts. The detector was operated at a *nominal* effective gain of 20×10^3. Plots were acquired for particle fluxes of $4 \, \text{kHz/mm}^2$ (a), $140 \, \text{kHz/mm}^2$ (b), $270 \, \text{kHz/mm}^2$ (c), and $1 \, \text{MHz/mm}^2$ (d).

the ions can travel is dependent on the arrival time of the next electrons. This leads to a reduced effective gain for shorter times to the previous event.

The reduction of the effective gain therefore occurs event by event, contrary to the increase of the effective gain due to an average change in transfer fields.

Taking a look at figure 3.34(b) further emphasizes this observation: the increase of effective gain is independent of the time to the previous trigger. What matters is the overall charge present in the detector, governed by the instantaneous rate, as already shown in figure 3.33 (b).
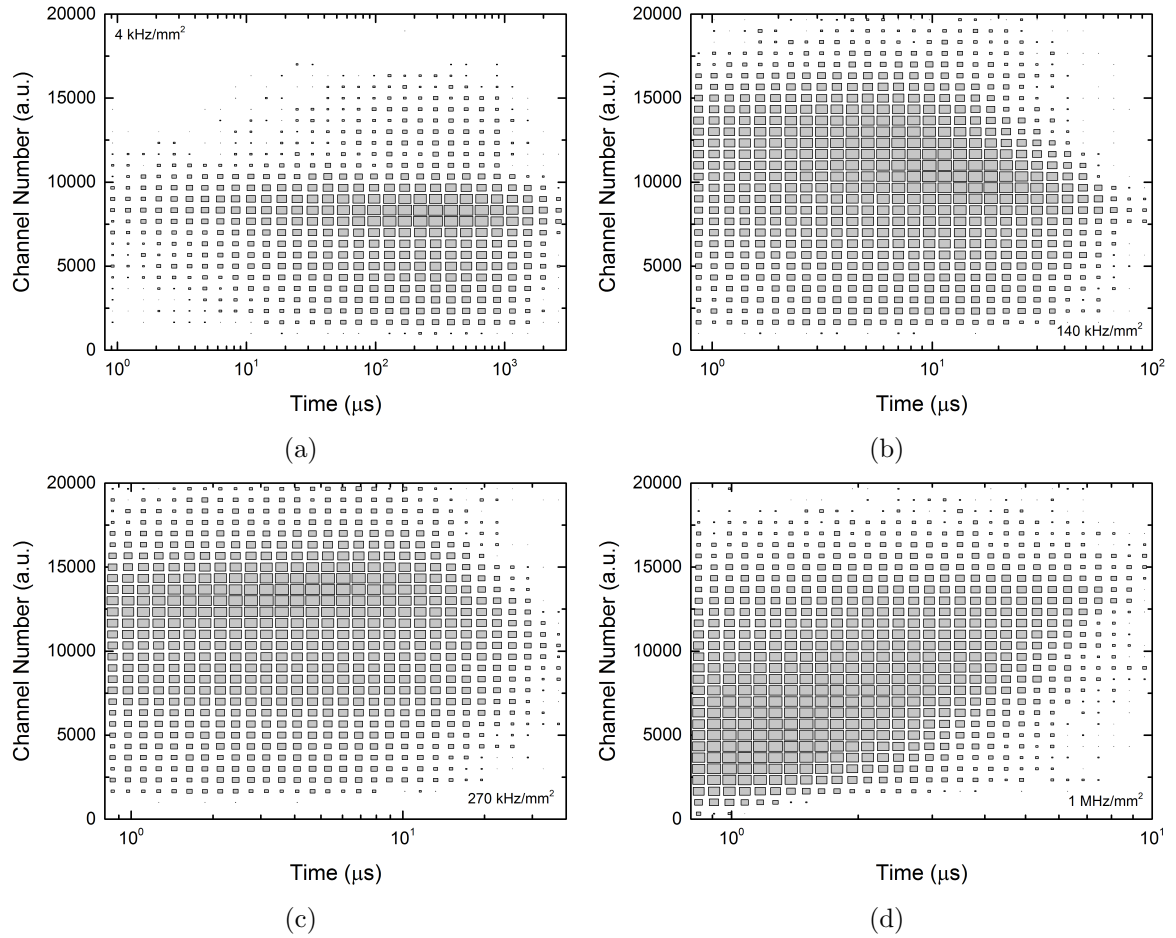
Figure 3.34: Dependence of charge integral on the time to previous trigger. The plot shows a 2D histogram of the pulses acquired for figure 3.35. The area of each rectangle represents the squared counts per bin and is normalized to the largest number of counts. The detector was operated at a *nominal* effective gain of $20{\times}10^3$. Plots were acquired for particle fluxes of $4\,\mathrm{kHz/mm^2}$ (a), $140\,\mathrm{kHz/mm^2}$ (b), $270\,\mathrm{kHz/mm^2}$ (c), and $1\,\mathrm{MHz/mm^2}$ (d).

3.4.4 Energy resolution

The previously described influence of the field distortions on the charge integral also have a strong impact on the energy resolution. Figure 3.35 (solid lines) gives examples of pulse height spectra acquired for different X-ray fluxes. Additionally, the spectra depending on the times to the previous event are shown (dashed lines). The pulse height spectra are split into ten time intervals depending on their time to the previous event, with each interval containing the same number of counts, as shown in figure 3.31. For clarity, only the first and last split histograms are shown as black and red dashed lines respectively. The spectra are scaled by a factor of 10 to allow easy comparison with the full histogram.

Figures 3.35 (a) to (d) show the previously described increase of the effective gain. Even
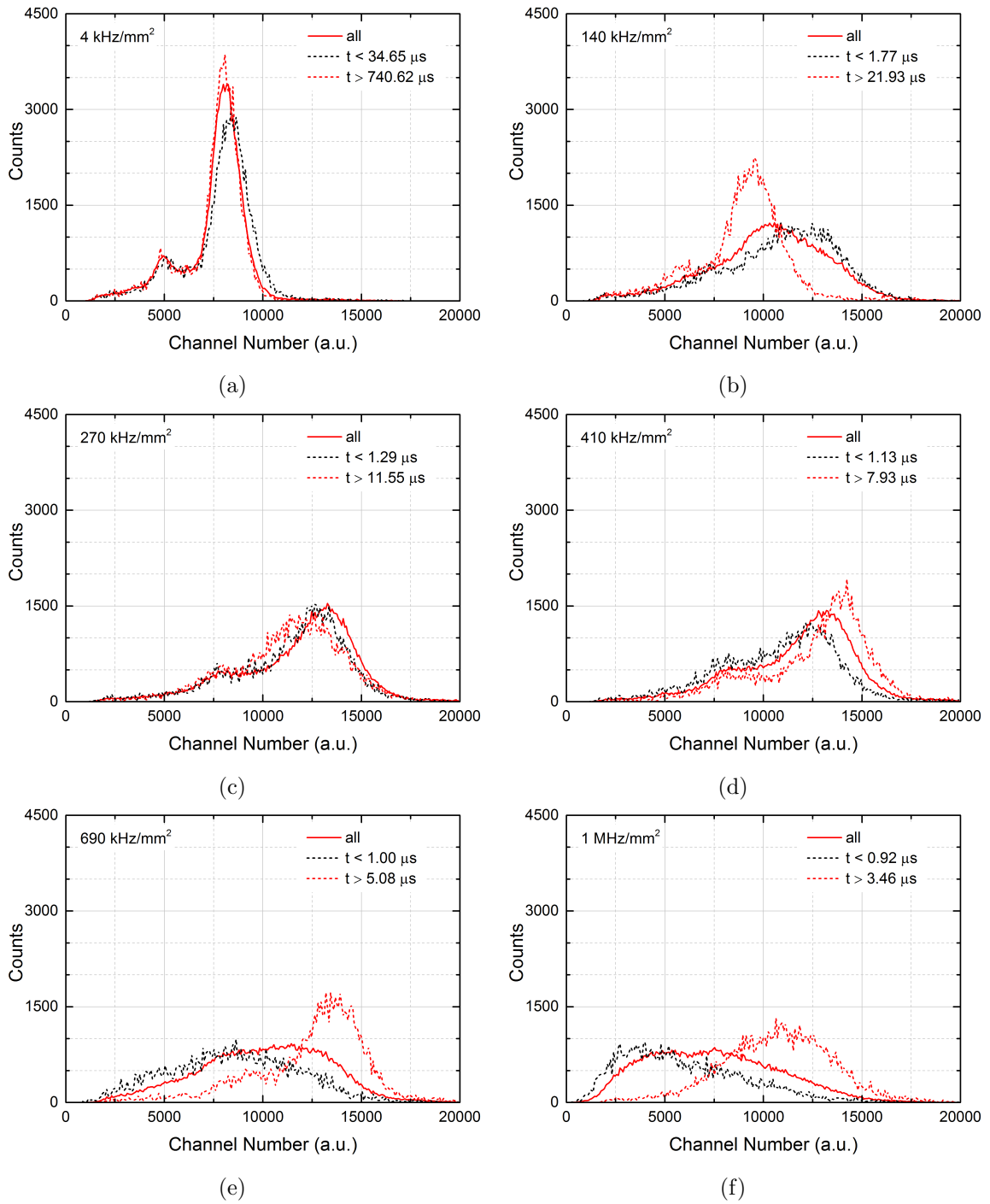
Figure 3.35: Pulse height spectra for different X-ray fluxes (solid) and fractions of pulse height spectra depending on the time to the previous trigger (dashed). Dashed spectra are scaled by a factor of 10 for easier comparison. For explanations see text. The detector was operated at a *nominal* effective gain of 20×10^3. Spectra were acquired for X-ray fluxes of $4 \, \text{kHz/mm}^2$ (a), $140 \, \text{kHz/mm}^2$ (b), $270 \, \text{kHz/mm}^2$ (c), $410 \, \text{kHz/mm}^2$ (d), $690 \, \text{kHz/mm}^2$ (e), and $1 \, \text{MHz/mm}^2$ (f).

though the increase occurs for events close in time to previous ones, the effect is due to the increase of the electron collection and extraction efficiencies. With the dependence on the instantaneous rate, the spectra get smeared out for increasing X-ray flux. The full energy peak and the escape peak are not separable in the region of increasing effective gain (figure 3.35 (b)). Once the effective gain curve reaches the plateau, the peaks are separable again, even though with decreased energy resolution (figure 3.35 (c)).

In figures 3.35 (d) to (f) it can be observed that the amplification is affected by the ion space-charge of previous events, as was previously described. Figure 3.35 (d) shows a decrease of the signal due to this effect (black line). The efficiencies of the GEMs continue to increase (red lines), as compared to e.g. figure 3.35 (c). This again confirms that there are two competing effects on the peak of the effective gain curve: the change in transfer fields are increasing the effective gain, while the change of amplification fields are decreasing the effective gain. For higher X-ray fluxes, the contribution of the amplification becomes dominant, leading to a decrease of effective gain.

Further increasing the X-ray flux would shift the position of the histogram towards even lower channel number.

3.5 Dependence of the energy resolution on the effective gain

The observations explained in the previous section are all related to space-charge effects, which are strongly dependent on the total amount of charge in the detector volume. Until now the charge was defined by keeping the detector at a constant low to medium *nominal* effective gain and changing the X-ray flux. In this section the effects of changing the *nominal* effective gain while keeping a low X-ray flux will be investigated.

3.5.1 Experimental setup

To investigate space-charge effects related to high effective gains the setup already described in section 3.4.1 was used. The *Drift* gap had a length of three millimetres, the *Induction* gap a length of 2 mm and both the *Transfer 1* and *Transfer 2* gaps are of a length of one millimetre each. To exclude any effects due to damages originating from discharges during previous measurements, a new irradiation position was chosen.

The transfer fields are kept constant at 3.6 kV/cm for *Transfer 1*, *Transfer 2* and *Induction* fields, and 2 kV/cm for the *Drift* field. The voltages across the GEMs were set to $V_{GEM1} = 397$ V/cm, $V_{GEM2} = 357$ V/cm, and $V_{GEM3} = 317$ V/cm to allow a *nominal* effective gain of 10^4. To increase the *nominal* effective gain, the potential differences between the GEMs' electrodes were increased starting at the listed values in equal steps on all three GEMs. The voltages used are listed in table 3.1. A copper X-ray tube was used to irradiate the detector, with the flux kept constant at about 550 Hz/mm^2.

G_{eff} ($\times 10^3$)	10	20	40	60	80	95	105	115	125
V_{GEM1} (V)	397	407	415	421	426	429	432	435	438
V_{GEM2} (V)	357	367	375	381	386	389	392	395	398
V_{GEM3} (V)	317	327	335	341	346	349	352	355	358
V_{tot} (V)	1071	1101	1125	1143	1158	1167	1176	1185	1194

Table 3.1: Potential differences on each GEM and sum of potential differences for *nominal* values of the effective gains investigated.

3.5.2 Measurements and methods

The measurements and methods are the same as explained in section 3.4.2.
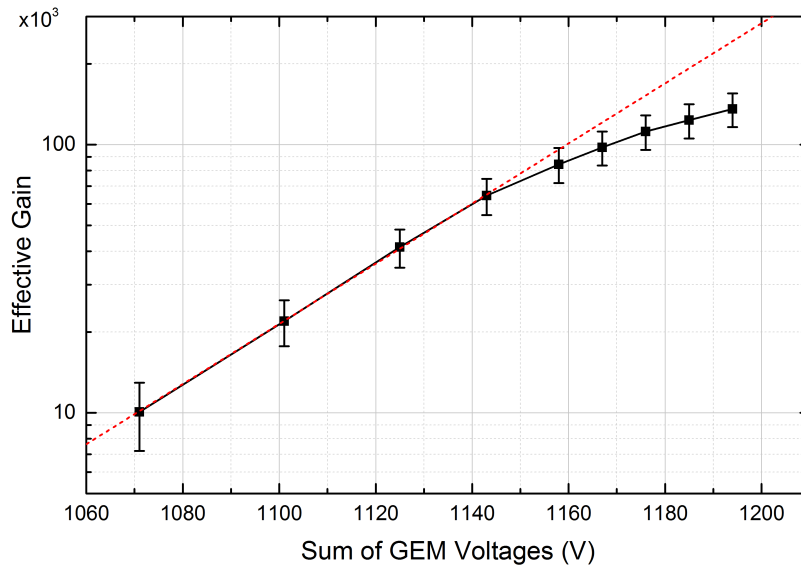
3.5.3 Results

Figure 3.36: Effective gain of the triple-GEM detector as a function of the total voltage applied across the three GEMs. The expected exponential behaviour of the effective gain without saturation is shown as a dashed line.

Due to the nature of the charge multiplication in GEM detectors, the effective gain is expected to be exponentially dependent on the sum of voltages applied to the three individual GEMs. Figure 3.36 shows the measured effective gain of the detector depending on the voltage across all three GEMs. For larger effective gains there is a deviation from the exponential behaviour (dashed line).

Figure 3.37 shows the positions of the full energy peak and escape peak in the pulse height spectra for the total voltage applied across the three GEMs. It shows a saturation for the 8 keV line starting at 1140 V, and a saturation of the escape line at 5 keV at higher voltage. Figure 3.37 also implies a convergence of of both curves at higher voltages. The voltages
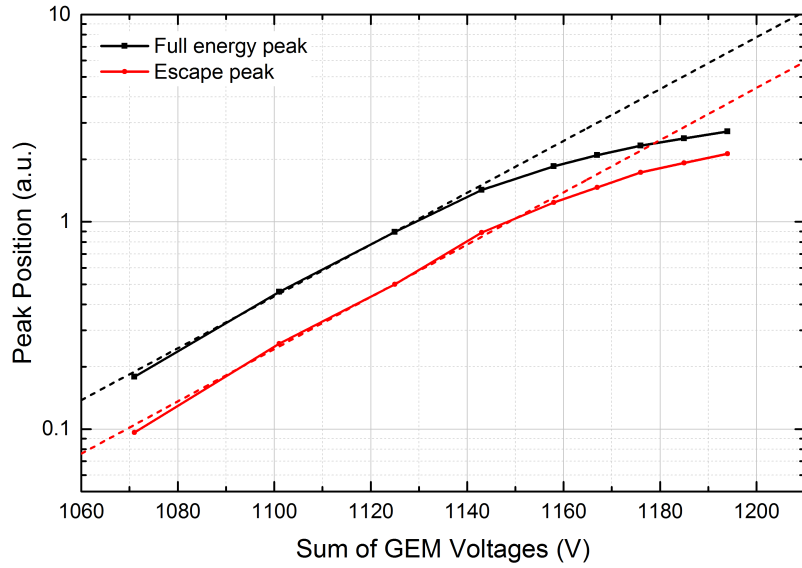
Figure 3.37: Position of the Cu 8 keV full energy peak and escape peak as a function of the total voltage applied across the three GEMs. The expected exponential behaviour of both peaks without saturation is shown as a dashed line.

could not be increased to higher values than those shown because of the onset of discharges.
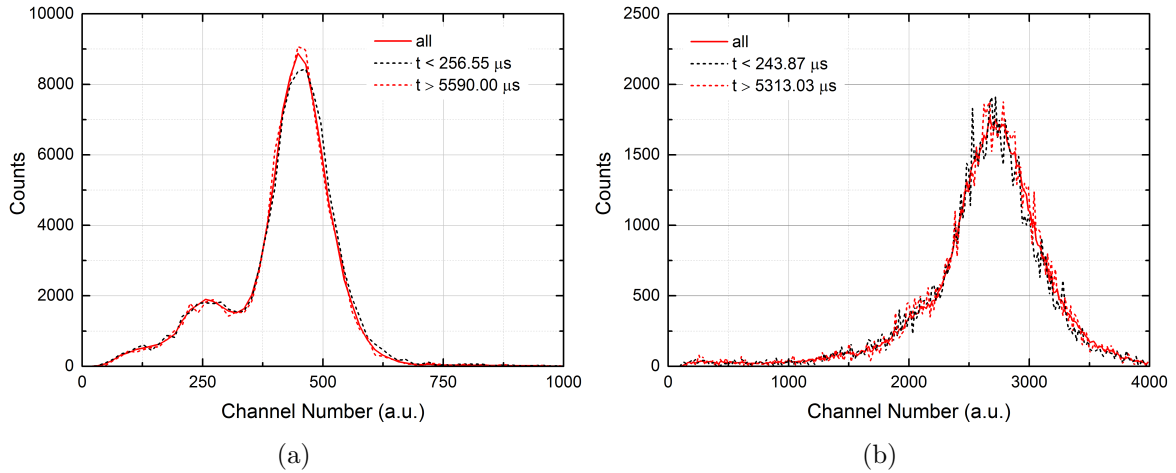

(a)	(b)

Figure 3.38: Pulse height spectra for different *nominal* effective gains (solid) and fractions of pulse height spectra depending on the time to the previous trigger (dashed). Dashed spectra are scaled by a factor of 10 to allow easier comparison of peak positions and shape. For explanations see text. Spectra were acquired with an X-ray flux of about 550 Hz/mm^2 and *nominal* effective gains of 20×10^3 (a) and 240×10^3 (b).

In section 3.2 space-charge effects for detectors operated at low gains and irradiated with high fluxes of soft X-ray fluxes were observed. The decrease of effective gain was due to the accumulation of positive ions from the charge multiplication of one event affecting the

amplification field of subsequent events. At the X-ray flux presented in this section, this is not the case. The ions have enough time to exit at the entrance of the GEM hole before the electrons of the next event arrive. Splitting the acquired pulse height spectra by their time to the previous event (see section 3.4.2) reveals no dependence on the time to the previous event (figure 3.38). On the other hand, the ions don't have enough time to exit the GEM hole to not affect the electrons of the *same* event. At these high effective gains, the multiplication of electrons leads to the creation of a huge number of ions. The ions from the front of the avalanche drift towards the entrance of the GEM hole. Their space-charge reduces the amplification field for the electrons of the same event arriving from the transfer region. The avalanche is therefore quenched by itself.

The saturation of the escape line at higher GEM voltages enforces this picture. The initial charge of the escape peak is much smaller than that of the full energy peak. To reach the same order of space-charge within the GEM holes, a much higher amplification field is needed. The quenching of the avalanche thus occurs at higher potential differences applied to the GEMs.
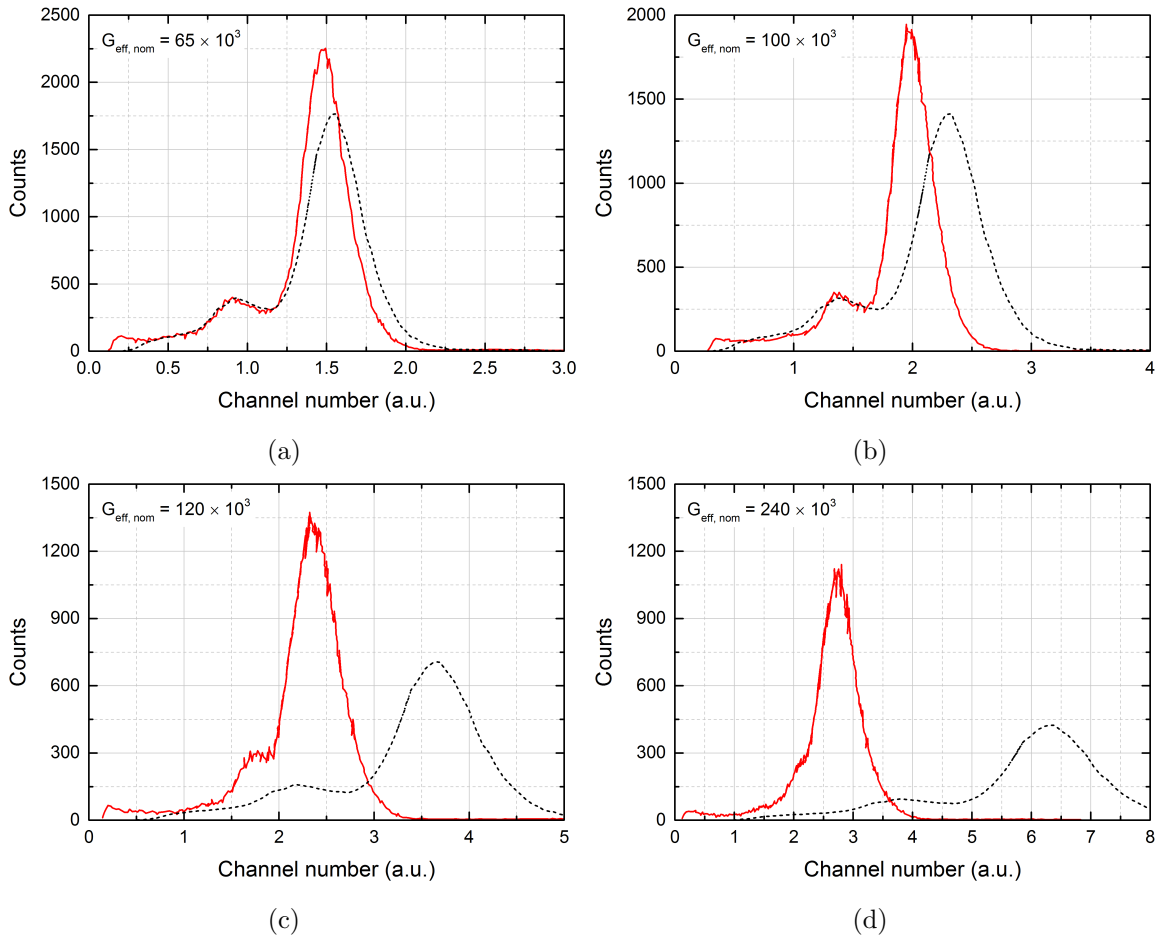

Figure 3.39: Pulse height spectra for *nominal* effective gains of 65×10^3 (a), 100×10^3 (b), 120×10^3 (c), and 240×10^3 (d) with the pulse height spectra for an effective gain of 20×10^3 rescaled to the unsaturated peak position following the exponential behaviour in figure 3.37.

Figure 3.39 shows pulse height spectra for various *nominal* effective gains. The spectra for an effective gain of up to 40×10^3 show no effects of saturation. For an effective gain of 65×10^3 the full energy peak is slightly saturated, with the effect getting stronger at higher effective gains.

At a *nominal* effective gain of 100×10^3 already both the full energy peak as well as the escape peak show effects of saturation. Both peaks' width is smaller and their centre is shifted towards lower channel numbers. This again shows a dependence of the saturation effect on the avalanche size.

For comparison, spectra not affected by saturation are plotted next to the saturated ones in figure 3.39. As well as the effective gain, both peak positions for the full energy peak and the escape peak are expected to scale exponentially to the voltage applied across the three GEMs. Thus, the peak position of the full energy peak can be calculated and any unsaturated pulse height spectrum normalized to it. Effects, such as a change in energy resolution are neglected in this case. The unaffected spectrum was acquired for an effective gain of 20×10^3.
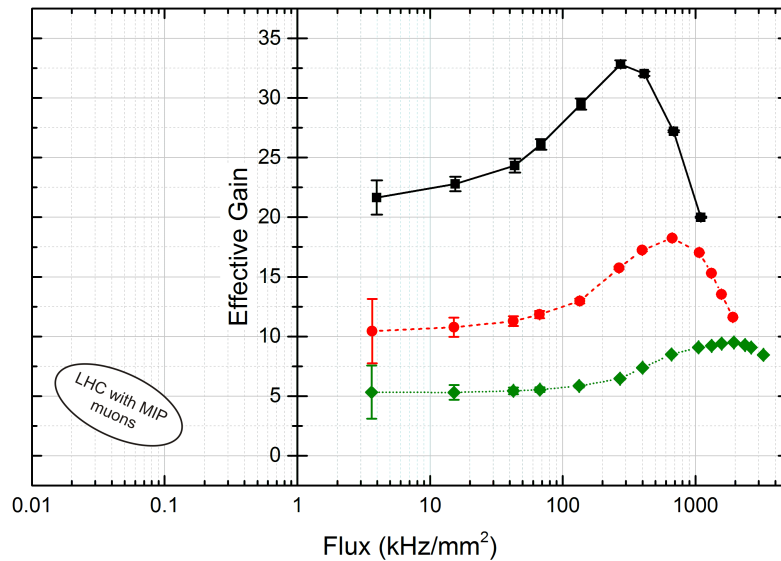
3.6   Discussion

Figure 3.40: Range of fluxes for the observed effects for different effective gains in comparison to current LHC experiments.

Positive ion space-charge is known to impose a limit on the operation of gaseous detectors, most notably as a saturation of the effective gain at very high particle fluxes. These limits were observed in the past for gaseous proportional counters and a number of micro-pattern gaseous detectors. Gaseous electron multipliers are known for their stable operation even at very large particle flux. The limits of operation are some orders of magnitude above what is

required e.g. in current LHC experiments, as seen in figure 3.40, or planned upgrades of those experiments. The possibility of using gaseous radiation detectors in general, and multi-GEM detectors in particular, in future experiments requires a re-evaluation of the intrinsic limits of those detectors.

As was shown, the onset of the change in detector gain is dependent on the *nominal* effective gain of the detector. Reducing the gain of the detector could therefore already push the observable effect to an X-ray flux above $1\,\mathrm{MHz/mm^2}$.

Additionally, it was shown that the effect depends on the charge present in each stage of the detector. The measurements were conducted with an $\mathrm{Ar/CO_2}$ 70/30 gas mixture for soft X-rays, yielding a primary charge of approximately 290 electrons in the conversion volume. For particles yielding less primary electrons, like e.g. muons, the necessary flux to observe the effect would be further increased. For neutrons on the other hand the primary charge would be increased. The particles which are detected by the GEM are of course dictated by the experiment they are used in and can not be changed. Still it is necessary to keep this in mind when comparing the measurements to the requirements of any experimental setup.

There are of course several parameters which can be changed: the gas mixture, the length of each gap, or even the GEM geometry. The following paragraphs give an overview why changing one of those parameters will not necessarily lead to the desired reduction of the observable effects.

Increasing the Argon content in the gas mixture would increase the primary charge released within the conversion volume. Reducing the Argon content reduces the primary charge. The effect would be shifted accordingly. But there are other parameters to be taken into account. The drift velocity of ions is, apart from the applied fields, depending on the gas mixture used. Increasing the content of Argon leads to higher ion mobility, as can be seen for example in [43]. The faster evacuation of ions would therefore decrease the space-charge effects in the detector. Additionally, the electron diffusion is affected. With reduced diffusion the possibility of electrons being collected on the top electrodes of the GEMs is decreased. This leads to higher initial collection efficiencies. The problem here is the diffusion depending on the applied field: depending on the nominal field and the content of Argon, reducing the field at the top electrodes of the GEMs might actually increase the diffusion (see figure 2.4) and reduce the collection efficiencies. At the same time, the amplification fields required to achieve the same nominal gain need to be higher for lower contents of Argon. This will have consequences for space-charge effects in the amplification regions.

Choosing a different quencher, as for example methane (CH_4) [44], or replacing Argon with another noble gas, for example Neon or Helium, will also increase the ion mobility [45], but will likely have unforeseen effects on all other parameters as well.

Another method to reduce the evacuation time of ions is to reduce either selected or all transfer gap lengths. As discussed previously, the effect is larger for every successive amplification stage involved, so a reduction of the *Transfer 2* gap length should yield stronger results than

for the *Transfer 1* gap. A shorter *Drift* gap will not lead to large changes and may additionally result in problems of reduced charge deposition by traversing particles. A smaller *Induction* gap length should have no effect owing to the absence of ions in it. Depending on the experimental conditions there is of course a lower limit on the gap length [46].

To increase the efficiencies of the GEM, it would also be possible to increase the hole diameter, reduce the pitch of the holes, or a combination of both. The resulting higher optical transparency of the GEMs would already lead to increased collection and extraction efficiencies at low fluxes, and a less pronounced effect at higher fluxes. What has to be taken into account when changing the geometry of the GEM foils is the stability of operation. Increasing the hole diameter requires higher potential differences applied between the GEM foils to reach the same amplification, which again could lead to undesired effects in detector operation.

3.7 Conclusions

Space-charge effects in multi-GEM detectors operated in an Ar/CO_2 70/30 gas mixture were studied. The behaviour of the effective gain and the ion back-flow into the conversion volume were investigated with collimated soft X-rays at fluxes of the order of MHz/mm^2.

The effective gain was observed to increase for high X-ray fluxes. This effect was found to be due to field distortions in the transfer regions between the drift cathode and the first GEM, and between the individual GEMs respectively. The electron collection and extraction efficiencies of the GEMs, not being 100%, under irradiation with low X-ray fluxes were considerably increased. For higher X-ray fluxes the effective gain was decreasing again, due to amplification field distortions in the GEM holes resulting in a reduction of the Townsend coefficient.

The ion back-flow was observed to continuously decrease under irradiation with high X-ray fluxes. The decrease was attributed first to a reduced ion collection and extraction due to the field distortions in the transfer gaps, and then to a reduced number of electron-ion pairs created per avalanche.

The effects were modelled using finite element analysis, showing the accumulation of ions, first in the transfer gaps, and then in the GEM holes. The model is in good qualitative agreement with the measurements. The deviations are mostly owed to the stochastic behaviour of the space-charge which can not be taken into account in the simulations.

Measurements with a double-GEM detector and a single-GEM detector showed that the effect of increasing effective gain is to be found in any device in which the transfer of charge from one stage to the next one is not 100%. The decrease of effective gain is observable once the positive ion space-charge in the amplification region gets large enough.

The energy resolution and shape of the pulse-height spectra of soft X-rays were studied. A method was developed to successfully acquire pulse height spectra at fluxes of the order of MHz/mm^2. The energy resolution was observed to decrease with increasing X-ray flux, with

notable distortions for the rising and falling slope of the effective gain curve. The distortions at increasing effective gain were found to be affected by the change of the transfer fields. The signals at decreasing effective gain were found to be dependent on the time to the previous event, determining the amount of ions from previous avalanches still present in the holes.

The extent of the observed effects on the effective gain, the ion back-flow and the energy resolution were dependent on the total amount of charge within the detector volume, mostly governed by the primary charge released within the conversion volume and the nominal effective gain of the detector.

Saturation effects in triple-GEM detectors operated in an Ar/CO_2 70/30 gas mixture were investigated. Detectors were operated at large effective gains, and irradiated with small fluxes of soft X-rays. The detectors were found to experience saturation when operated at effective gains of around 10^5 or above. The build-up of positive ions within each electron avalanche lead to a self-quenching effect, thus reducing the effective gain. Event by event measurements showed that the effect dependends on the avalanche size, affecting lower-energetic events less than those with higher energies. This again showed that the magnitude of the effect was governed by the primary charge released within the conversion volume of the detector.

Chapter 4

Charge Transfer Properties Through Graphene for Applications in Gaseous Detectors

For the upgrade of the Time Projection Chamber (TPC) of the ALICE experiment, a triple-GEM detector was proposed as read-out device [47]. The impact of ion pile-up within the conversion volume of the TPC on the track reconstruction and particle identification was thoroughly studied. While positive ions created during the primary ionization also contribute to space-charge induced field distortion, the main factor is the large number of ions drifting back into the conversion volume from the triple-GEM. To reduce the ion back-flow, eventually a quadruple-GEM detector using a variation of different GEM foils and optimized field configurations was suggested as the charge-amplification and read-out device [48].

While the ALICE TPC upgrade is just one prime example, considerable efforts have been made to reduce the back-flow of positive ions into the conversion volume of gaseous detectors for various applications, e.g. TPCs [22], gaseous photo-multipliers [27] or multi-GEM detectors in general. The influence of gas-mixtures and pressures was studied [49], as well as the effect of the fields applied [50]. The latter parameter has the largest impact, resulting in an easy way to control the amount of ion back-flow *to a certain extent and with considerable trade-offs*, for example in detector gain. This method alone is insufficient for some applications, therefore the use of a quadruple-GEM or gating wires between the second-to-last and last GEM was investigated.

We started research on a different approach: using a layer of pristine graphene suspended over the holes of a GEM as a membrane only transparent to electrons and therefore effectively removing the ion back-flow completely.

A review on the currently known transfer properties of electrons and ions through graphene is given in section 4.1. The production of graphene samples is summarized in section 4.2. The transfer of graphene layers onto support structures mounted into the detector is described

in sections 4.3 and 4.4. A description of different methods of quality assurance is given in section 4.5.

The experimental setups used, and the methods developed to measure the charge transfer properties through graphene are explained in section 4.6 and 4.7 respectively.

Measurements of graphene single-layers and triple-layers on GEM-like meshes are presented in section 4.8 through 4.9. The investigation of charge transfer properties through graphene on GEM electrodes is described in section 4.10. Descriptions of the methods and measurements are given at the introduction to each section. A summary and outlook is given in section 4.11 at the end of the chapter.

4.1   Charge transfer properties of graphene

Graphene is the thinnest material to date, consisting of a single layer of carbon atoms arranged in aromatic rings forming a honeycomb-like structure. Its extraordinary mechanical properties allow for a stable integration of freely suspended graphene over holes of tens of micrometers in diameter. The basic hexagonal ring has a bond length of 0.142 nm and an inner radius of 0.246 nm. The π bonds orthogonal to the lattice can be seen as a delocalised cloud of electrons which overlaps the hole in the hexagon. This reduces the opening pore, yielding an effective diameter of 0.064 nm [51], much smaller than the van der Waals radius of most atoms.

Graphene has been shown to exhibit high transparency to electrons with energies ranging from tens of keV up to 300 keV [52][53][54]. While these energy ranges are commonly used for transmission electron microscopy, they are three to four orders of magnitude above the drifting electron energies found in gaseous detectors. Several studies, both theoretical and experimental, have been done for electron energies in the range of a few to hundreds of electron-volts. The most important results are summarized in the following paragraphs.

Electron transmission measurements were performed by very low energy scanning transmission electron microscopy (STEM) [55]. The electron energies used were ranging from 1 eV to 5 keV, with the energy range from 1 eV to 30 eV investigated in detail. The electron transmission, even though not quantified, showed a dependence on the electron energy, with a transmission peak around 5 eV.

The electron reflectivity for free-standing graphene was computed for electron energies ranging from 0 eV to 8 eV [56]. It was found to show a number of minima and maxima in reflectivity depending on the number of graphene layers. The reflectivity, computed for up to six layers of graphene, was experimentally confirmed for up to four layers of graphene supported on SiO_2. These results are similar in behaviour to those measured for graphene single-, double- and triple-layers on a copper surface [57], with the number of reflectivity minima depending on the number of graphene layers.

Calculations for energies from 20 eV to 200 eV [58] show electron transmission variations de-

pending on the energy, with a strong trend of increased transmission for electron energies above 40 eV. Electron energies between 20 eV and 40 eV show strong variations in transmission, ranging from 0.05 % to 0.95 %, with the largest transmission at 20 eV.

A direct measurement [59] of the electron transmission of freely suspended graphene has been done in a vacuum setup, showing a transmission of 73 % for electrons of 66 eV. The same study found a further decrease of 27 % per additional graphene layer, with respect to the number of electrons passing the previous one. Measurement for electron energies ranging from 100 eV to 205 eV showed similar results [60], with single-layer graphene showing an electron transmission of 74 %. The electron transparency for freely suspended graphene has only recently been measured [61] for low-energetic electrons of 10 eV to 40 eV and was found to be approximately 50 % to 60 % and independent of the electron energy. A sharp decrease for electron energies lower than 10 eV was probably due to build-up of space-charge and barium contaminations within the setup and could not be investigated conclusively. Some important results for the energy ranges used in gaseous detectors are illustrated in figure 4.1.
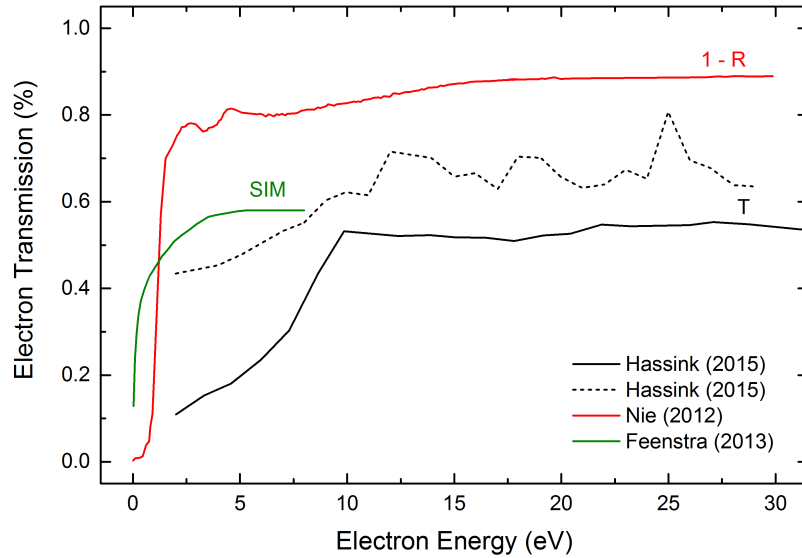

Figure 4.1: Electron transmission through suspended graphene sheets as measured by *Hassink, et al.* [61] and simulated by *Feenstra, et al.* [56]. The electron reflectivity of graphene on a copper substrate was measured by *Nie, et al.* [57]. The transmission *T = 1-R* does not take interactions between the electrons and the graphene layer into account. All curves show the behaviour in vacuum.

On the other hand, graphene should be impermeable to atoms, molecules and ions [62] if they do not have enough energy to go through the electron cloud. Experimentally, suspended graphene has been measured to withstand an irradiation dose up to approximately 10^{16} ions/cm^2 at tens of keV energies [63]. Other experiments have shown that graphene is completely impermeable to helium atoms up to 6 atm [64].

4.2   Graphene growth

There are several methods of fabrication of graphene, the most common of which are mechanical and liquid phase exfoliation, reduction of graphite oxide, and chemical vapour deposition (CVD). The earliest method of isolating graphene was continuous peeling of graphite with adhesive tape until only small flakes of graphene remained on it [65]. This method yielded graphene flakes of up to $100\,\mu m$ in length, which is already sufficient to study intrinsic properties of graphene [66].

Another method to obtain graphene is the reduction of graphite oxide. In the most common method [67] graphite is treated with a mixture of sulphuric acid, sodium nitrate and potassium permanganate. The graphite oxide obtained is then exfoliated sonically to create graphene oxide. After (electro)chemical reduction the graphene oxide has structure similar to graphene, even though limited in size and containing a large number of defects [68][69][70]. Graphene can also be obtained by exfoliation of graphite using non-oxidizing solvents. The dispersion containing both graphite and graphene flakes can then be centrifuged and filtered to obtain a powder of graphene flakes [71][72].

Even though graphene produced by exfoliation of graphite or chemical reduction of graphite oxide is of high quality, the process is time-consuming and the samples are restricted both in terms of sample size and uniformity, therefore putting a natural limitation to bringing the production of graphene to an industrial scale.

Another approach, which was proven to scale up the production of high quality graphene layers, was the direct growth of graphene on substrates by chemical vapour deposition. First results were obtained on silicon carbide [73], ruthenium [74] and nickel [75], followed shortly after by synthesis of graphene on copper substrates [76][77].

CVD strongly depends on parameters like temperature and pressure ranges used during nucleation [78], or contaminants like oxygen attached to the substrate surface [79]. It is furthermore believed to be equally dependent on the quality of the surface itself [80][81], even though recent studies "suggest that the growth of continuous macroscopic pristine graphene on copper is not limited by the substrate" [82]. A recent method allows the growth of graphene on liquid copper-nickel alloys [83][84], claiming graphene sheets with less wrinkles and defects and with properties closer to theoretical graphene.

A wide variety of products employing the production techniques described are readily commercially available by an ever growing number of suppliers (see [85][86], and [87] or [88] as examples for suppliers of the samples used in this work and for ongoing studies).

4.3   Graphene transfer

To achieve large area graphene coverage on a target substrate, in general the wet transfer method [89] is used: Graphene layers on copper substrates are covered with a sacrificial layer
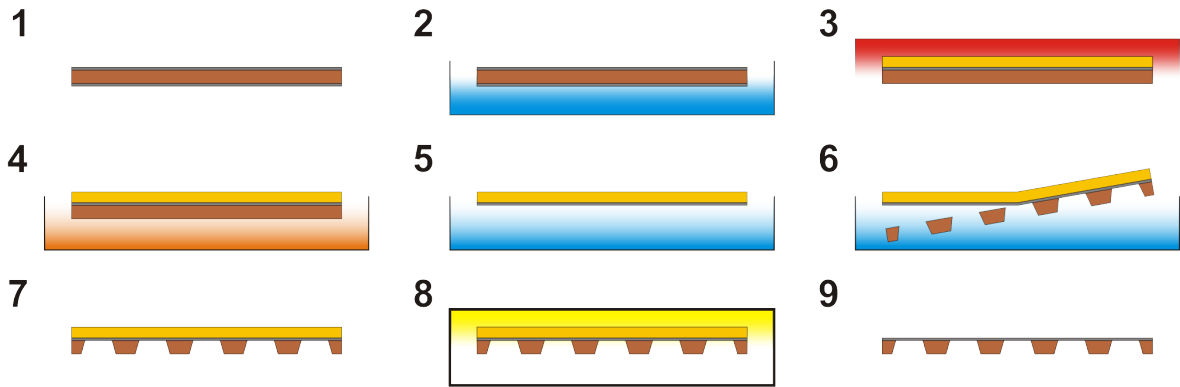
Figure 4.2: Schematic of graphene transfer onto a support structure: Commercially available graphene on a copper substrate (1) is suspended in nitric acid to etch away one of the two graphene layers (2). A layer of PMMA is spin-coated onto the remaining layer and cured (3). The copper substrate is etched away in perchloric acid (4) and cleaned in several steps in demineralized water (5). The graphene layer is transferred onto a support (6), still protected by the PMMA layer (7). The PMMA layer is then removed with ethanol (8) [in a critical point dryer to prevent the graphene from breaking], yielding a layer of graphene on the support structure (9) ready to be mounted into the detector.

of polymethyl methacrylate (PMMA). The copper is etched away and the stack of PMMA and graphene transferred onto the target substrate. The PMMA is then dissolved and washed away.

The transfer process is depicted in figure 4.2. The text in square brackets is an alternative step [90] integrated into the routine after several unsuccessful transfers.

Improved methods [91] and alternative approaches to the wet transfer method have been developed: free-standing graphene membranes can be manufactured without the need for transfer, either employing direct growth of graphene on a support structure covering the holes [92][93] or etching of holes into the substrate the graphene is deposited onto [94]. The latter method and results obtained within this thesis are described in section 4.4.

Graphene, even though considered a perfectly flat and real two-dimensional material, after transferring and freely suspending it in holes, exhibits a change in topology: even perfectly arranged graphene shows a number of height fluctuations [52][95]. The lattice's perfect hexagonal shape is disturbed by imperfect boundaries between joined graphene flakes, resulting in a number of pentagonal and heptagonal rings along the grain boundaries. The resulting deviations from the two-dimensional shape not only give the suspended graphene three-dimensional stability, but also reduce the stress and with it the number of defects within the layer [96][97].

Even though the size of even single isolated graphene flakes is of the order of micrometres, it can already be observed under an optical microscope, owing to a small change in contrast compared to silicon wavers or even when freely suspended on a support structure [66]. As

will be shown in this chapter, the position of graphene layers on a metal support struc-
tures utilized for our studies can be seen with the naked eye, therefore allowing the mounting
of the samples in standard clean room facilities without the help of any additional equipment.

Graphene samples were purchased by the suppliers listed above. GEMs and GEM-like
meshes were manufactured at the CERN MPT workshop. The layout of both GEMs and
meshes was altered during the project to overcome challenges arising both in graphene trans-
fer and measurements. A detailed description of the support structures used can be found in
the specifications of the setup presented at the beginning of each study within this chapter.
The transfer of the graphene layers onto the support structures was done by collaborators
at University College London and London Centre for Nanotechnology, as described in sec-
tion 4.3. The transfer process, initially failing completely, as well as the quality assurance,
was refined several times as is explained in the sections following. Ultimately, a new transfer
method was developed [98] to achieve large area coverage with graphene. The new method
allows coverage of hole diameters at least one magnitude of order larger than previously
achieved [89][94], without defects and contaminations with residual PMMA. In section 4.8.2
additional measurements on single-layer graphene, transferred onto meshes by an external
supplier, are described. The transfer of multiple layers of graphene onto meshes and GEMs
is explained in sections 4.9.1 and 4.10 respectively.

4.3.1   Critical point drying

During the supercritical drying process the PMMA is dissolved in acetone, which is then
washed away with highly pressurised and thus liquified carbon dioxide. The liquid carbon
dioxide is heated to bring it above its critical point (31 °C and 74 bar approximately), thus
removing any surface strain on the suspended graphene sample. With the pressure gradually
released until the supercritical CO_2 becomes gaseous again, it is released from the chamber
where a dried sample remains.
The steps enforced during the drying process are the following:
The chamber of the critical point drier is thoroughly cleaned with acetone, and then cooled
down to below 15 °C by surrounding it with ice. The sample holder inside the chamber is
filled with acetone, and the sample is placed inside the chamber carefully. The chamber is
sealed, and CO_2 is slowly added through the top valve, until the pressure reaches around
50 bar. Acetone is flushed slowly through the bottom valve, while the chamber pressure is
maintained at approximately 50 bar. Once all the acetone is removed all valves are sealed
and the chamber is taken slowly to above critical point of CO_2 by removing the surrounding
ice and flushing heated water through designated pipes in the chamber walls. Once above
the critical point for a certain amount of time, the CO_2 is vented into an exhaust, releasing
the pressure in the chamber. After the chamber is fully emptied and cooled down to room
temperature again, it is opened and the dried sample removed.
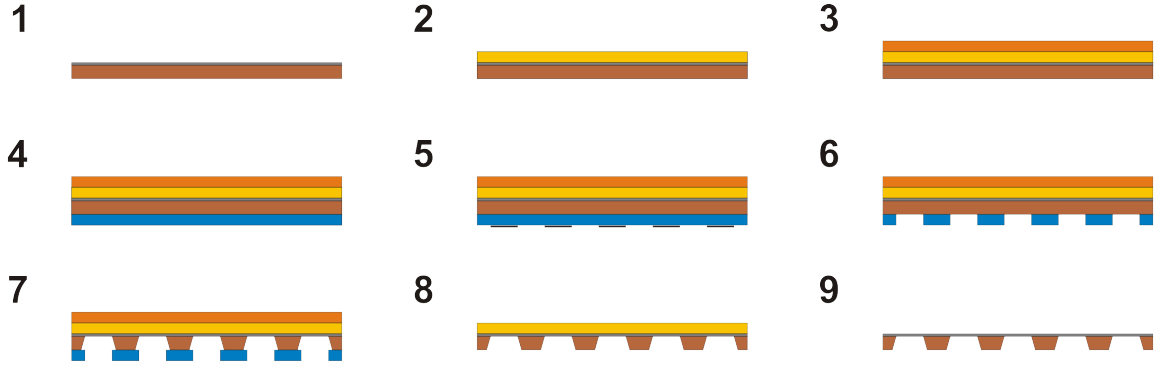
4.4 Direct etching of graphene substrate

Figure 4.3: Schematic of refined etching procedure to produce GEM-like meshes with suspended graphene membranes: Commercially available graphene on a copper substrate after removal of the bottom graphene layer (1) is covered with a layer of PMMA (2) and protected by an additional layer of *HIPR6512* liquid photo-resist (3). The bottom side of the sample is laminated with *FX 930* photo-resist (5). The UV-mask with holes of desired diameters is placed onto the laminate, yielding a mask with openings only at the desired hole positions after irradiation with UV light and the resist developed in Na_2CO_3 (6). The copper is then etched with $FeCl_3$ (7), with both the PMMA and the *HIPR6512* layer protecting the graphene layer from detaching during the process. Both photo-resists are stripped away with acetone (8) and the PMMA is removed inside a critical point drier as explained previously.

A second approach to producing graphene membranes suspended on GEM-like copper meshes was investigated. To reduce the stress on the graphene layers during transfer, the possibility of directly etching the copper substrate instead of transferring the graphene was studied. The method, originally developed for TEM grids [94] was modified as shown in figure 4.3. The first trials yielded coverage of the holes of about 70%, with even the covered holes featuring large damaged areas. No contamination with PMMA was found by Raman spectroscopy.
Even though the first results were promising, the technique was not refined more due to the studies being focused on the transmission through a membrane transferred onto the bottom electrode of a GEM.

4.5 Graphene quality assurance

The quality of the graphene transfer can already be assessed during the transfer process itself: PMMA creeping underneath the copper substrate during spin-coating will most probably lead to the copper not being fully etched. Stress on the layer when scooping it out of a beaker or obvious wrinkles in the graphene layer after the transfer already give a hint towards a faulty process. If the transfer was deemed successful, the quality of the graphene layer was checked by scanning electron microscopy (SEM) to assess the amount of defects and contaminations.

Additional Raman spectroscopy gave further information about defects, layer thickness and quality, and contaminations.

4.5.1   Scanning Electron Microscopy

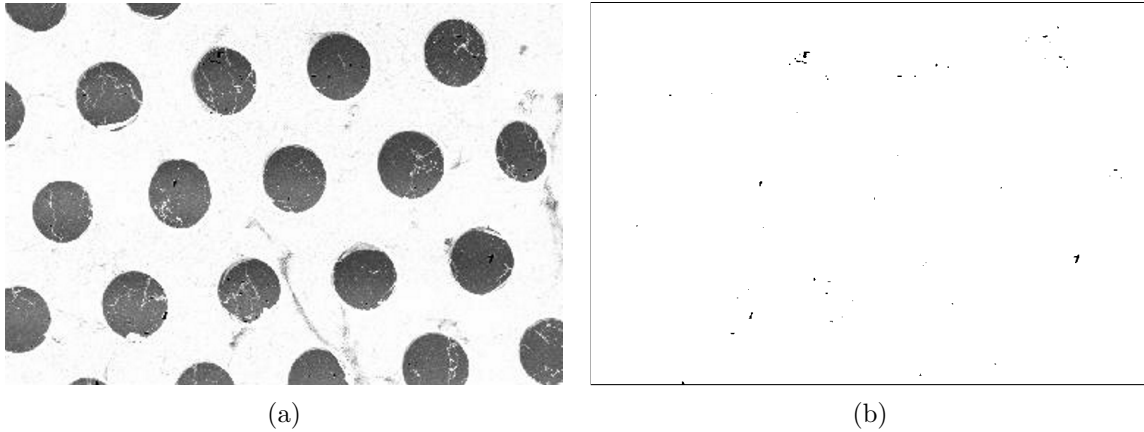|	
(a)	(b)

Figure 4.4: SEM image of single-layer graphene on a mesh (a) and assessment of the defects by image segmentation (b).

The first part of the quality assurance employs the use of a scanning electron microscope (SEM). The graphene-covered mesh is mounted inside the chamber of an SEM. Since the electrons of the SEM are accelerated in an electric field between the filament and the sample under investigation, the sample (graphene) and its support (mesh) have to be highly conductive. Using SEM as a method to investigate the number of defects in the sample additionally gives information about surface contaminations. PMMA is not conductive and will therefore appear as black smudges on the images acquired.

The amount of defects is investigated using image segmentation, as is shown in figure 4.4. The defects appear as black pixels in the image and can therefore be easily distinguished from graphene-covered holes or the surface of the mesh. A low contrast of the image might impede the correct separation of holes from sagging graphene layers, which appear in a darker shade than the ones perpendicular to the impinging electrons.

A full mapping of the sample surface is possible by scanning the full area and assembling the acquired pictures.

4.5.2   Raman spectroscopy

Raman spectroscopy has proven a versatile tool to assess the quality of graphene layers [99][100][101]. Each Raman spectrum shows a number of features which change with the number of layers and the stacking order between them. In addition to the evaluation of the number of layers, the Raman spectra are used to assess the number of defects in the graphene layers. A comprehensive summary of graphene assessment can be found in [101] and [102], with a short
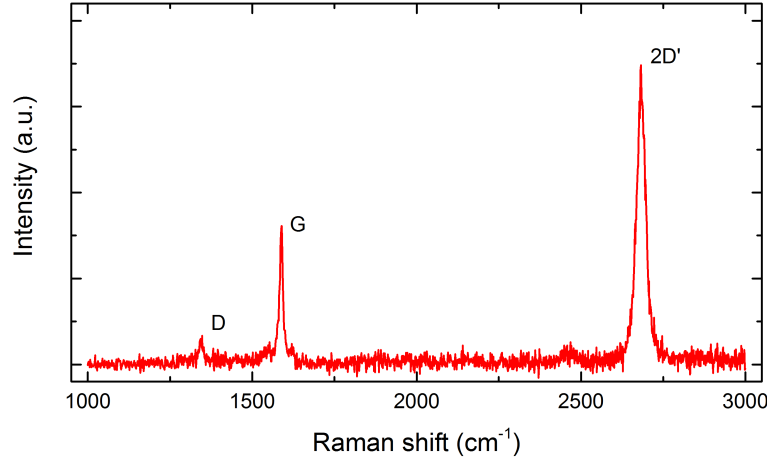
Figure 4.5: Typical Raman spectrum of single-layer graphene. For explanations see text.

overview given in the following paragraphs.

An example Raman spectrum is shown in figure 4.5. The most dominant features are the D band at $1350 \, \text{cm}^{-1}$, the G band at $1580 \, \text{cm}^{-1}$, and the second order of the D band, the so-called 2D band at $2700 \, \text{cm}^{-1}$. The positions of the bands are dependent on the excitation energy of the laser used. The listed values are for an energy of $2.33 \, \text{eV}$. All peaks show a change of shape, position, and relative intensity depending on the number of layers and defects.

The G band results from in-plane stretching vibrations. It becomes more intense for increasing number of layers due to the larger number of atoms contributing to the vibrations. The D band is only active if there are defects in the graphene layer. An absence of this band is therefore an indication for pristine graphene.

The 2D band at $2700 \, \text{cm}^{-1}$ is used to assess the number of layers. Even if the D band is absent in pristine graphene, its second order is present. The 2D band is perfectly symmetric for single-layer graphene. For bi-layer graphene the interaction of both graphene planes result in a widening of the peak. For three layers the interactions become more complex, thus giving rise to an increased broadening of the peak. Additionally, the peak positions are shifted in frequency depending on the number of layers. While this shift of frequency may also be due to unintended folding of layers, a change in intensity will reveal the differences of e.g. folded bi-layer graphene and four-layer graphene.

4.6 Experimental Setup

A sample of graphene is transferred onto a support structure. The support structure is either a GEM-like mesh consisting of only one electrode of a GEM, with the second electrode and the intermediate Kapton$^{\text{TM}}$ layer etched away, or an electrode of a GEM (for the sake of readabil-
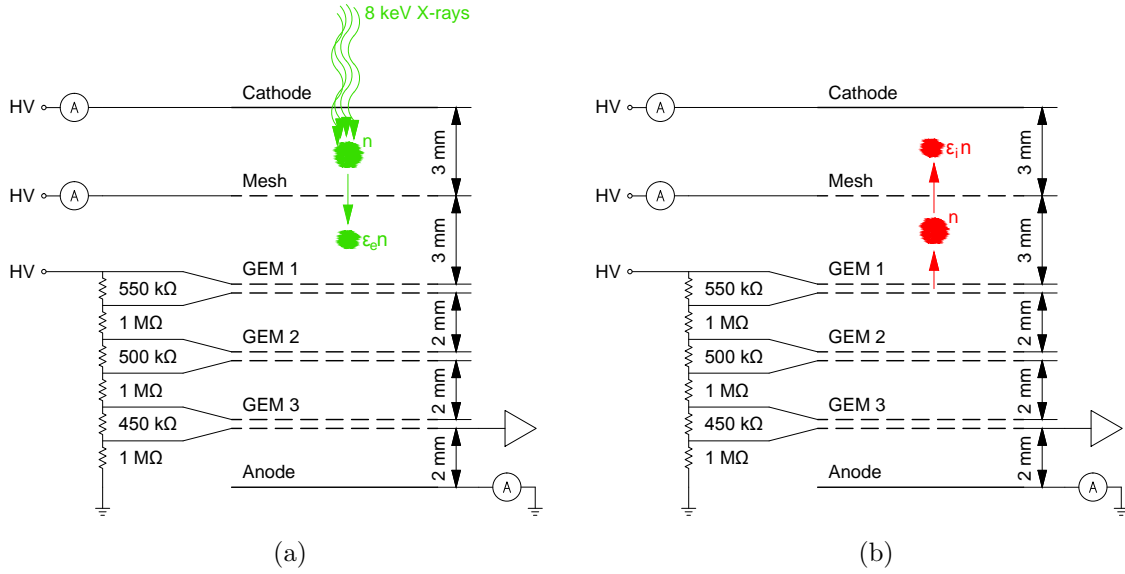
Figure 4.6: Schematic of the setup used to study charge transfer properties of graphene. Electron transmission (a): n primary electrons from X-rays converted in the first conversion volume drift into the second conversion volume. Depending on the electron transparency ϵ_e a fraction $\epsilon_e n$ reaches the second conversion volume. Ion transmission (b): n ions from the first GEM drift towards the cathode. A fraction $\epsilon_i n$ is collected on the cathode, depending on the ion transparency ϵ_i, the rest is collected on the mesh or graphene sample.

ity the term *mesh* refers to either a GEM-like mesh or GEM in the descriptions of sections 4.6 to 4.7.3). The mesh is inserted into the conversion volume of a *standard* triple-GEM detector, as shown in figure 4.6. The triple-GEM is powered via a resistor divider with a *CAEN N1470* high-voltage power-supply [103]. Both the drift cathode and the mesh are powered individually with a channel of a *CAEN NDT1470* high-voltage power-supply [104]. Currents were read from the cathode and mesh via the integrated ammeters of the power-supply. The anode current was read with a *Keithley Model 6487* Picoammeter [32]. Event-by-event signals were read from the bottom electrode of the third GEM via capacitive coupling to an *ORTEC®* *142PC* [33] pre-amplifier and ORTEC® 474 Timing Filter Amplifiers [105]. Pulse-height spectra were acquired with an *AMPTEK MCA-8000D Multi-Channel Analyser* [35].

As will be presented in sections 4.8 to 4.10 the detector was operated at different effective gains and with different fields in the two conversion volumes. Different Ar/CO_2 gas mixtures were used to flush the detector continuously at approximately $5\,L/h$.

The detector was irradiated with a collimated $8\,keV$ Copper X-ray beam of chosen beam diameters. The detector was mounted vertically on a back-plate in a distance of about $10\,cm$ to the X-ray generator, with the collimator touching the window of the GEM detector to minimize the spread of the X-ray beam. The X-ray flux was adjustable by changing the X-ray tube intensity and could be quickly turned on or off with an integrated shutter.

4.7 Measurements and methods

The electron transparency was measured with two different methods, of which the second one was only used for later samples. The methods are described in section 4.7.1. Which method was used for each individual sample is described in the description of each measurement within this chapter. The ion transparency was measured in the same way for all samples presented within this chapter and is described in detail in section 4.7.2.

The electron and ion transparencies of graphene were studied as a function of the fields applied above and below the mesh. With the transparency of the uncovered mesh already depending on those fields, the study of the charge transport properties through graphene were done by comparative measurements on the covered and uncovered mesh.

4.7.1 Electron transparency

The electron transparency is defined as the fraction of primary electrons passing from the first conversion volume to the second conversion volume, as depicted in figure 4.6 (a). The charge reaching the second conversion volume will be amplified and is read out either as current induced on the anode or event by event from the bottom of the third GEM. Additionally, the charge deposited in the second conversion volume will be equally amplified and read out simultaneously.

Electron transparency measurement by peak position

This method uses a chain of pre-amplifier, amplifier and multi-channel analyser connected to the bottom electrode of the third GEM via capacitive coupling. As explained before, the acquired pulse height spectra will show a higher-energetic full-energy peak and a lower-energetic escape peak. Since the charge is deposited in both conversion volumes at the same time, the spectrum will show two instances of each peak. The positions of the ones corresponding to the first conversion volume are reduced by a factor which equals the electron transparency of the mesh or graphene layer under investigation.

The electron transparency of a mesh is defined as

$$T_e = P_1/P_2 \; , \tag{4.1}$$

with the peak positions P_1 and P_2 corresponding to the centroid of the Gaussian fit onto the main peak (8 keV for the Cu X-ray tube used) of the first and second conversion volume respectively.

Since the conversion above and below the sample are equally affected by the amplification of the triple-GEM detector mounted below, any non-uniformities of the gain between two investigated positions on the XY-plane are cancelled out by calculating the ratios of the peak positions.
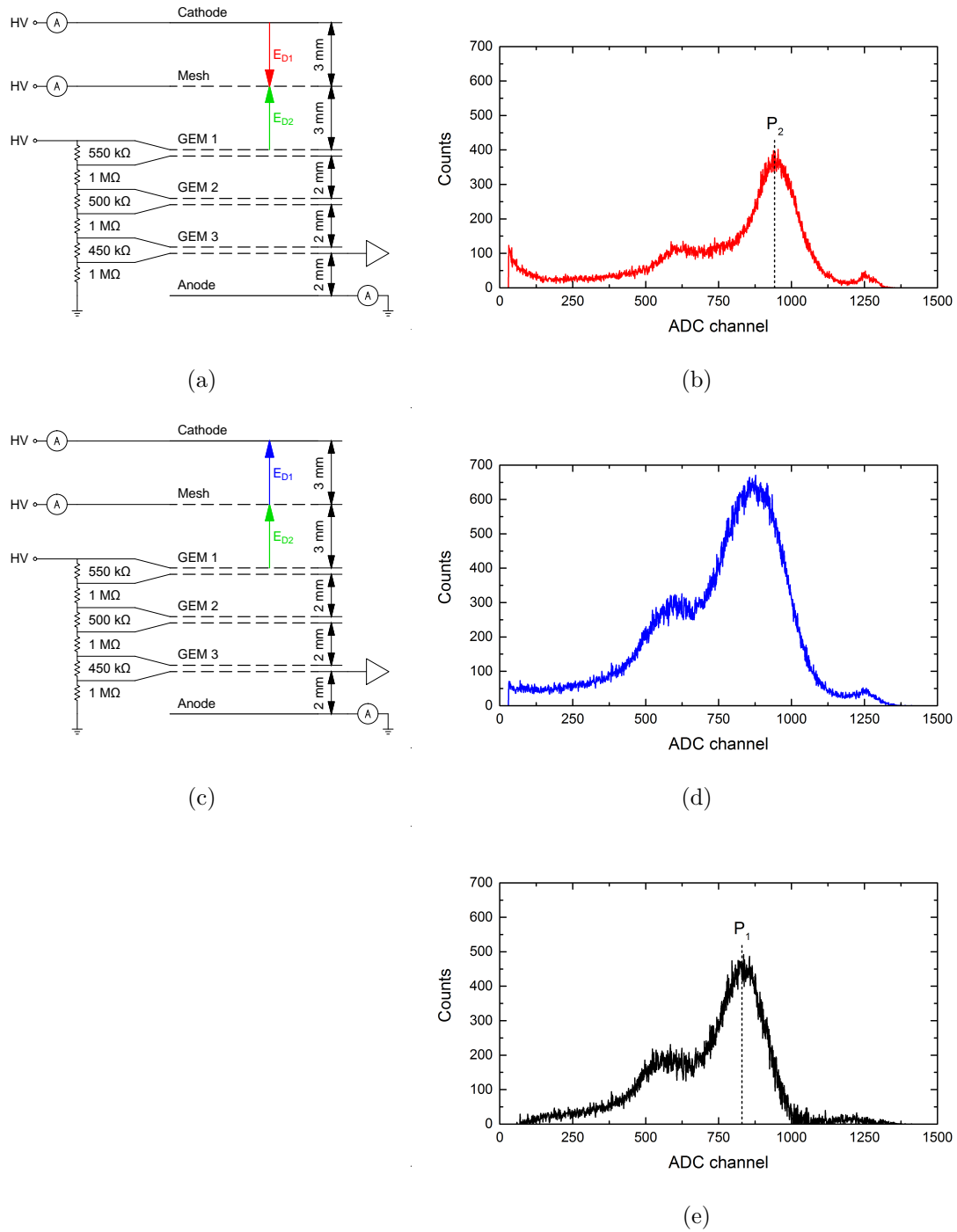
(a)

(b)

(c)

(d)

(e)

Figure 4.7: Measurement of electron transparency. Setup with inverted *Drift* field $E_{D1} < 0\,\text{V/cm}$ shown in figure (a). The corresponding pulse height spectrum in (b) shows the 8 keV copper peak and the argon escape peak from the second conversion volume. The setup with non-inverted field $E_{D1} \geq 0\,\text{V/cm}$ is shown in figure (c). An example spectrum acquired for non-inverted field shown in (d) shows the 8 keV peak and the escape peak of both conversion volumes overlapping. After subtracting the spectrum for non-inverted field from the one for inverted field the resulting spectrum is shown in (e).

Three problems might arise during this procedure:

1. For high electron transparencies, the two main peaks at P_1 and P_2 might overlap. If the transparency of the mesh is 100%, the counts of both main peaks will be summed at the correct position and the Gaussian fit will not be affected. If the transparency is less than 100%, the separation of peak P_1 from peak P_2 might not be possible.

2. For lower electron transparencies, the main peak at P_1 of the first conversion volume might be shifted towards the escape peak of the second conversion volume. In this case, the peak position calculated by Gaussian fit might be biased towards the position of this peak.

3. It has to be ensured that the full energy peak is well above the noise threshold to correctly estimate the peak position. Not being able to distinguish the escape peak of the first conversion volume from the noise doesn't affect the measurement, since only the position of the full energy peak is used to calculate the electron transparency. Keeping the noise low by adequate grounding of the detector or increasing the signal-to-noise ratio by changing the effective gain of the detector both define the minimum electron transparency still observable. A good balance of both methods is recommended. If the electron transparency can not be resolved by peak positions, the currents collected at the read-out anode have to be used. This method is described in the next section.

A procedure to overcome the first two problems is shown in figure 4.7: First the field E_{D1} above the mesh is inverted to about $E_{D1} \approx -100\,\text{V/cm}$ (Fig. 4.7)(a)). When the detector is irradiated, all primary electrons from the first conversion volume drift towards the cathode and are fully collected there. Primary electrons from the second conversion volume drift towards the triple GEM stack. The detector effectively behaves like a standard triple GEM detector with the second conversion volume acting as the *Drift* volume of the detector.
A reference pulse height spectrum is acquired (Fig. 4.7)(b)) and stored for the next step of the measurement. The spectrum only shows the main and escape peak of the second conversion volume.
The field E_{D1} is then changed according to the field ratio E_{D2}/E_{D1} desired, with the field E_{D2} below the mesh kept constant (Fig. 4.7)(c)) Again, a spectrum is acquired. Depending on the transparency of the mesh this spectrum now show up to four peaks, or two smeared out peaks as illustrated in figure 4.7)(d)). The reference spectrum acquired in the step before is now subtracted from this pulse height spectrum. The resulting spectrum (Fig. 4.7)(e)) only shows the main peak and escape peak from the first conversion volume, with both peaks shifted towards lower channel number according to the transparency of the mesh. The higher number of counts in the first conversion volume is due to the X-rays being additionally attenuated before reaching the second conversion volume. A Gaussian function is then fitted onto the main peak, as well as the main peak at lower energy corresponding to the primary

charge deposited in the first conversion volume. The electron transparency is then calculated from (4.1).

It is important to take both spectra within a reasonably short time interval of a few minutes, since the amplification of the triple GEM is changing with ambient parameters like pressure and temperature. This leads to a shift of the peak positions and therefore errors when subtracting one spectrum from another.

Electron transparency by anode current

Inverting the field E_{D1} will results in a behaviour of the detector similar to a standard triple GEM detector. The effective gain can therefore be written as

$$G_{eff} = \frac{I_A}{n_2 R_2 e} \; , \tag{4.2}$$

with the interaction rate R_2 and number of primary electrons n_2 in the second conversion volume. Similar, and assuming no conversion takes place in the second conversion volume, the effective gain for charge deposited within the first conversion volume is

$$G_{eff} = \frac{I_A}{T_e n_1 R_1 e} \; , \tag{4.3}$$

with only a fraction $T_e n_1$ drifting into the second conversion volume. Solving both equations for the electron transparency T_e results in

$$T_e = \frac{I_1/R_1}{I_2/R_2} \; . \tag{4.4}$$

For the transparency calculation by peak positions the fields need to be inverted to overcome the problem of overlapping peaks. The transparency on the covered side of the mesh can then be compared to the one on the uncovered side. To measure the electron transparency of the graphene sample, a measurement on the covered side, as well as one on the uncovered side is necessary. Preferably, a reference position on the uncovered side close to the position on the graphene layer should be used.

A spectrum has to be acquired on both hit positions, once for the inverted field and once for every field ratio E_D2/E_D1 investigated. At the same time, the current collected at the read-out anode, as well as the rate are recorded for each spectrum. Conveniently, the number of counts can be extracted from the pulse height spectra and can be used instead of the rate. First, the field E_{D1} is inverted to measure the currents I_2 and rates R_2 corresponding to the second conversion volume on both the covered and uncovered side of the mesh. After applying a non-inverted field E_{D1}, the sums of currents $I = I_1 + I_2$ and $R = R_1 + R_2$ for both conversion volumes are measured, allowing the calculation of the currents I_1 and rates R_1 related to the first conversion volume.

R_1 is taken from the uncovered mesh since the rate on the covered side additionally depends

on the transparency of the graphene sample. All other values are taken from the hit position on the graphene investigated. Formula (4.4) can then be re-written as

$$T_e = \frac{(I - I_1)/R_{1,unc}}{(I_2/R_2)} \tag{4.5}$$

to calculate the electron transparency T_e of the graphene sample.

4.7.2 Ion transparency

The electrons from both conversion volumes drift towards the triple-GEM mounted below the mesh, where they undergo charge amplification. The ions released in the ionization processes drift back towards the cathode. A part gets collected on the mesh, the rest will drift into the first conversion volume and will eventually be collected on the cathode (figure 4.6 (b)).
The ion transparency is then defined as

$$T_{ion} = \frac{I_C}{I_M + I_C} \ , \tag{4.6}$$

with the currents I_C and I_M read from cathode and mesh respectively. The contribution of ions from primary ionization in both conversion volumes is found to be negligible.
The graphene layer already blocks a fraction of the primary electrons from the first conversion volume, thus reducing the number of electrons available for amplification in the triple GEM. As a result, the number of ions drifting back into the conversion volumes will be reduced. To ensure the measurements on the covered and uncovered side of the mesh are comparable, it has to be checked that the sum of cathode and mesh currents normalized to the anode current $(I_C + I_M)/(I_A)$ is constant for both hit positions.
To achieve a current high enough to be read out with the ampere-meters of the power supply, the X-ray flux is increased to the order of a few kHz/mm^2 and the gain of the detector is set to the order of 2×10^4.
To favour the extraction of ions from the mesh the field ratio is set to $E_{D2}/E_{D1} < 1$. Due to limitations of the maximum voltage provided by the power supply, the field E_{D2} is set to a considerably lower value than for the electron transparency measurements, thus reducing the ion back-flow from the triple-GEM.

4.7.3 Electron transparency depending on electron energy

To investigate the transmission of electrons depending on their energy, there are several ways to change it. As shown in figure 4.8 there is a strong dependence of the electron energy on both the applied fields and the gas mixture used. While a change of electric field or gas mixture is a simple method to increase the energy of electrons impinging on the graphene layer, even at very high fields of several kV/cm the energies reached are restricted to a few electronvolt. With the length of first conversion volume typically in the order of a few millimetres the
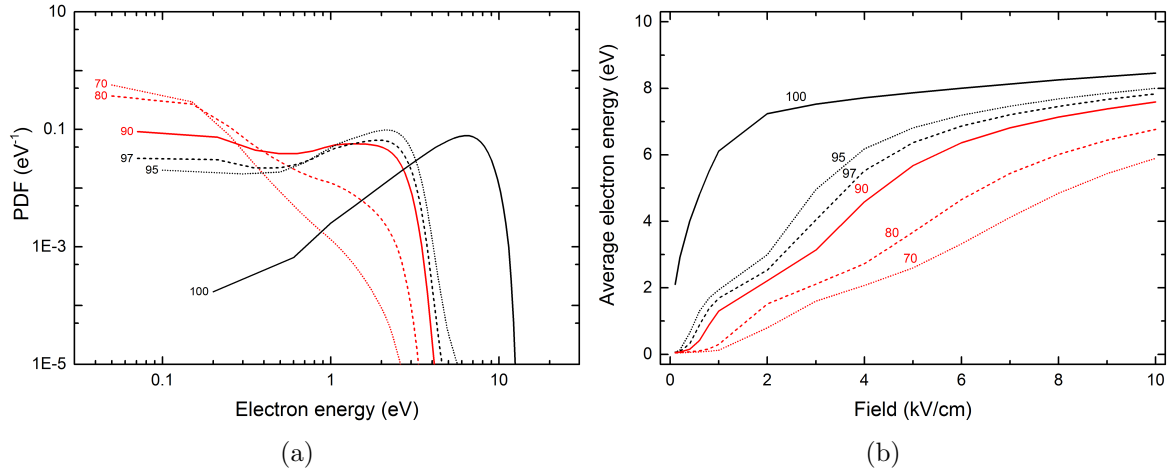
Figure 4.8: Distribution of electron energies in a field of $1\,kV/cm$ (a), and average electron energy depending on the applied electric field (b), for different Ar/CO_2 gas mixtures. The argon content is shown next to the lines. Data taken from [8].

maximum reachable field is restricted by the maximum voltage supplied by the power-supply. Using a sample which is either mounted on the bottom electrode of a GEM or reducing the distance between the GEM-like mesh and the cathode to a few hundred micrometers allows for larger fields in the GEM holes or in the short conversion volume respectively. The GEM would be the preferable setup, but is prone to defects during the transfer of the sample, which may result in a short between the two electrodes of the GEM. Using a short first conversion volume reduces the amount of charge deposited in it. An additional conversion volume on top of the first conversion volume increases the number of primary electrons available for the study. Depending on the mesh used to separate this conversion volume from the original first one will result in a loss of charge due to the low transparency, and additional complications in separating the peaks of the three conversion volumes.

The measurements on a GEM are similar to the ones performed with a graphene covered mesh. One of the electrodes is covered with a sample of graphene. Additionally to choosing fields E_{D1} and E_{D1} allowing for maximum transparency the voltage across the GEM $V_{GEM} \geq 0\,V$ is increased to study the charge transmission through the graphene sample. Taking into account the thickness of $50\,\mu m$ of the GEM a maximum voltage of $V_{GEM} = 100\,V$ has to be maintained to stay in a regime below charge amplification.

4.8 Single-layer graphene on a GEM-like mesh

4.8.1 Standard wet transfer with PMMA

A sample of single-layer graphene of about $3 \times 1\,cm^2$ was transferred onto a GEM-like mesh of $10 \times 10\,cm^2$ active area, with hole diameters of $30\,\mu m$ and a pitch of $60\,\mu m$. The mesh was inserted into the conversion volume of a *standard* triple-GEM detector, $2.5\,mm$ above
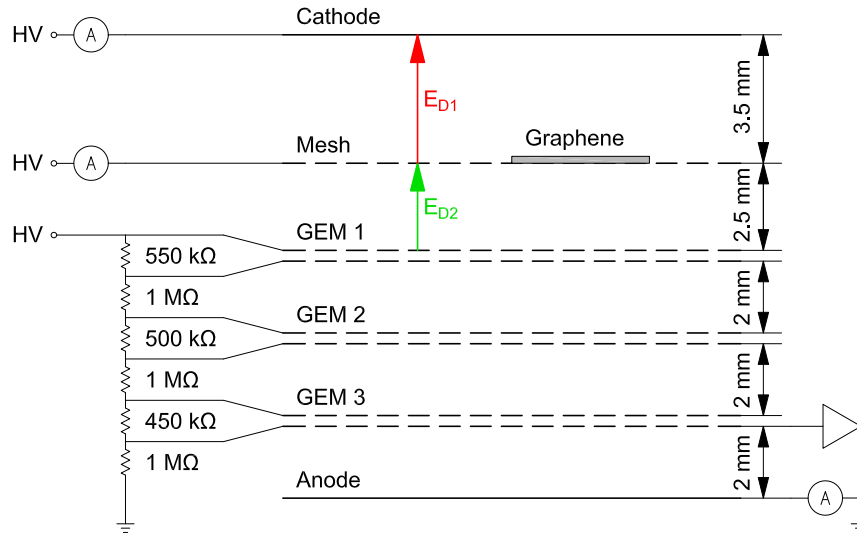
Figure 4.9: Setup of the first measurement of a single-layer graphene sheet on a GEM-like mesh. The field in the first conversion volume was $E_{D1} = 400\,\mathrm{V/cm}$, the second one was set to $E_{D2} = 800\,\mathrm{V/cm}$.

the topmost GEM, and with the drift cathode $3.5\,\mathrm{mm}$ above the mesh. The triple-GEM was powered by a resistor divider. Both the drift cathode and the mesh were powered individually with high current resolution power supplies. Pulse-height spectra were acquired from the bottom electrode of the third GEM, as shown in figure 4.9.

The detector was operated at an effective gain of about 3×10^3. The fields in the first and second conversion volumes were set to a field ratio of $E_{D2}/E_{D1} = 2$ with the field in the first conversion volume set to $E_{D1} = 400\,\mathrm{V/cm}$.

The detector was irradiated with a collimated $8\,\mathrm{keV}$ copper X-ray beam of about one millimetre beam diameter. The detector was scanned in horizontal direction in steps of five millimetres over the active area of the detector, with the x-axis crossing the centre of the graphene sample.

The electron transparency was estimated by measuring the ratio of the two peak positions at a given field ratio. The peak positions (dashed lines) of the full-energy peaks corresponding to both conversion volumes in figure 4.10 show a trend of increasing effective gain from left to right. This effect is most probably due to a sagging of the mesh resulting in changed fields due to modified distances between the mesh and the electrodes mounted above and below. The mesh shows a transparency in the order of 75% for all hit positions investigated.

The ion transparencies across the sample, as well as the currents collected on drift cathode and mesh are shown in figure 4.11. When comparing the mesh current with the peak position of the second conversion volume in figure 4.10 (dashed red lines in both figures) the sagging
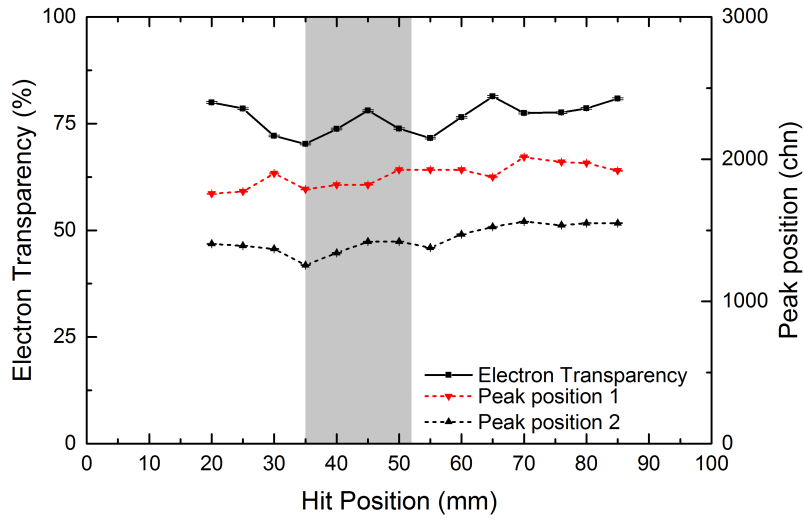
Figure 4.10: Electron transparency of the first mesh studied. Peak positions of the signal from the first conversion volume (black) and second conversion volume (red) shown as dashed lines. Estimated position of the graphene layer shown as grey background.
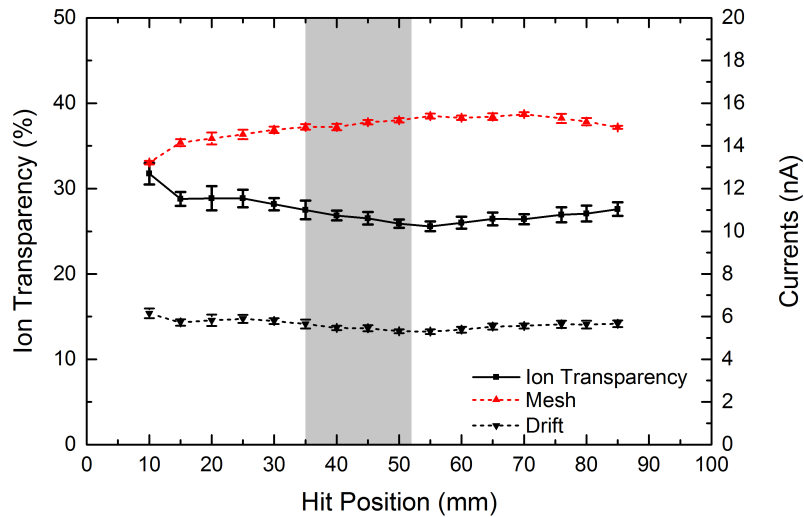

Figure 4.11: Ion transparency of the first mesh studied. Currents collected on the drift cathode (black) and the mesh (red) shown as dashed lines. Estimated position of the graphene layer shown as grey background.

of the mesh resulting in changing fields can be observed. Even though the ion transparency is changing over the area scanned with the X-ray beam, there is no correlation between ion transparency and graphene layer position.

Concluding from the measurements shown in figures 4.10 and 4.11, a heavily damaged graphene layer was assumed.

(a)   (b)
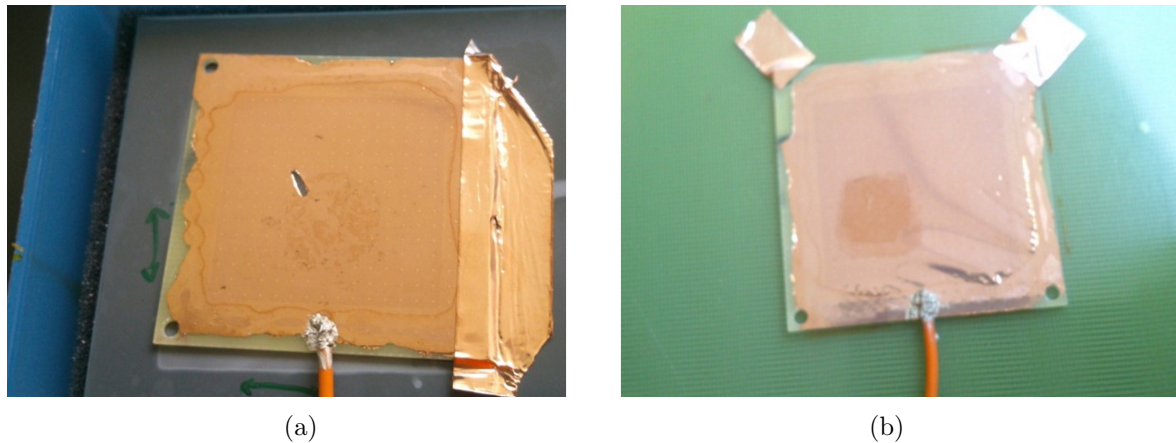
Figure 4.12: Images of samples on the supporting GEM-like mesh. The example on the left shows what is considered a bad transfer (a) and the one on the right a good transfer (b). While the quality of the layer cannot be judged in terms of uniformity and integrity, sample (a) only shows patches of graphene, while sample (b) shows a well defined square.

Several other samples were investigated, but showed similar results for electron and ion transparency, regardless of the fields applied above and below the mesh. Some samples already showed large damages during the transfer process, as is shown in figure 4.12. Concluding from the results acquired with samples of what was considered a good transfer, the ones which showed problems during the transfer were not mounted into the detector and investigated.

To assess the quality of the graphene transfer, the samples acquired in what was considered better transfers were dismounted after the measurements and SEM images were taken, as described in section 4.5.1.

Examples illustrating the state of the graphene layers on three samples are shown in figure 4.13. Apart from most holes partly covered by graphene "cobwebs" or heavily damaged layers, only small fractions of intact suspended graphene were found randomly distributed over the first sample in figure 4.13 (a) and (b). The quality of the second sample in figure 4.13 (c) and 4.13 (d) is worse: only a small fraction of holes are covered, with most of the graphene only covering parts of the supporting mesh. An example of SEM images acquired after a bad transfer is shown in figures 4.13 (e) and (f). The holes are not covered and barely any graphene is visible on the surface of the mesh.
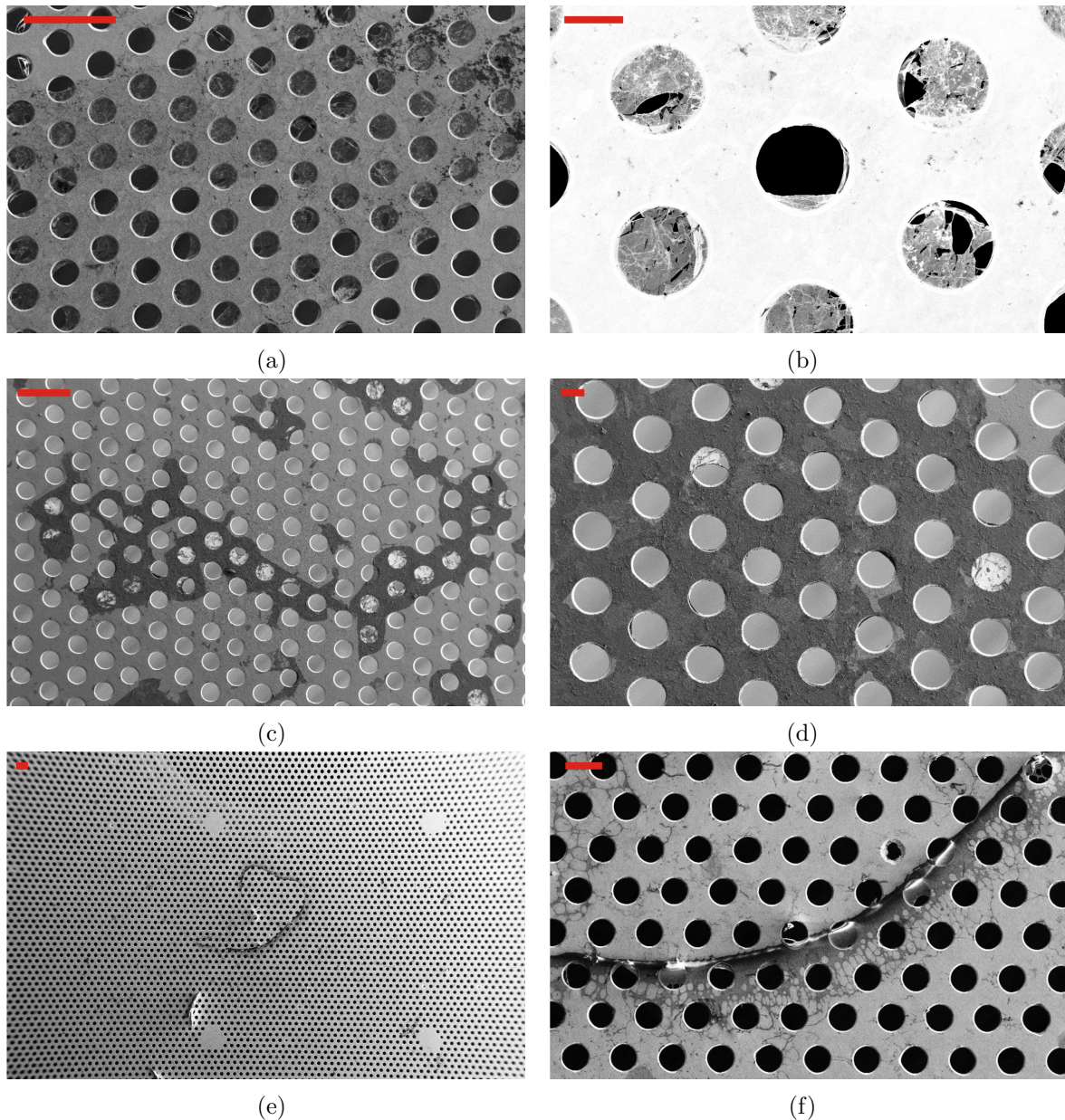
Figure 4.13: SEM images of a fraction of three samples (left side) and images of holes in further detail (right side). Scale bars are $100\,\mu$m and $40\,\mu$m for left and right side respectively. The meshes have a hole diameter of $30\,\mu$m and pitch of $60\,\mu$m. The layer is clearly visible on the left image, as well as defects ranging from cracks in the holes to completely broken layers. Black smudges are considered contamination with residual PMMA due to insufficient cleaning. The detailed picture on the right side reveals heavily damaged graphene layers suspended in the holes. The first two samples were considered the ones with the most successful transfer. The images were acquired after mounting the meshes in the detector and studying the transparencies of the layer.
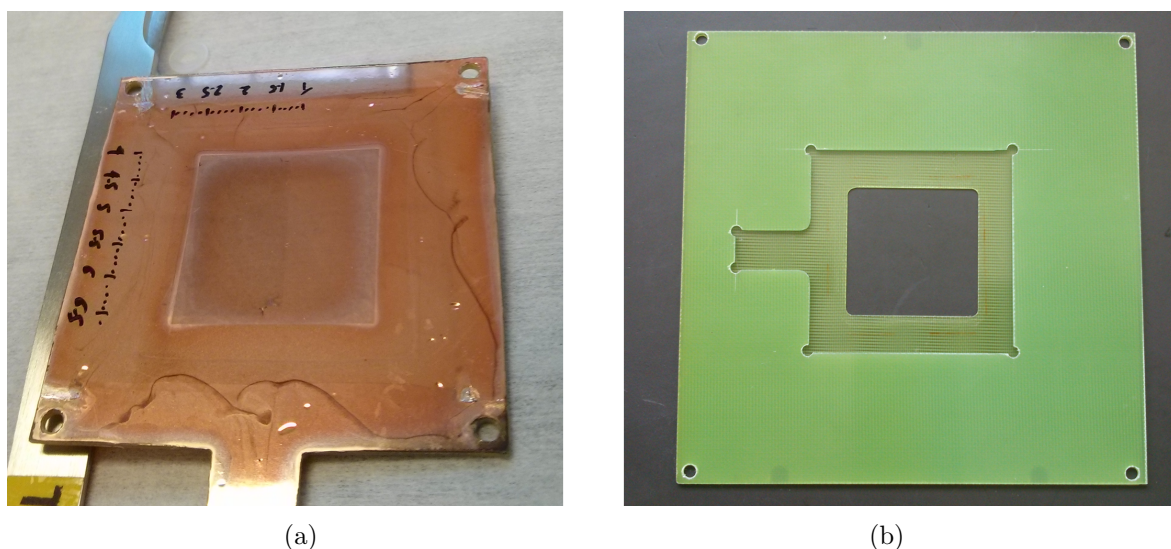
Figure 4.14: Example picture of a new mesh (a) with an active area of $2.5{\times}2.5\,\text{cm}^2$ and sturdier frame. The image shows a graphene layer transferred at UCL, as described in 4.9.1. The support structure (b) holds the mesh in place.

4.8.2 PMMA-free transfer

New GEM-like meshes of $2.5{\times}2.5\,\text{cm}^2$ active area were produced. The thickness of the meshes was $5\,\mu\text{m}$, with holes of $30\,\mu\text{m}$ diameter. Four different versions were produced: copper meshes with pitches of $60\,\mu\text{m}$ and $120\,\mu\text{m}$ and copper meshes with a $1\,\mu\text{m}$ gold layer on top and the same dimensions. An example of a copper mesh with a pitch of $60\,\mu\text{m}$ is shown in figure 4.14 (a).
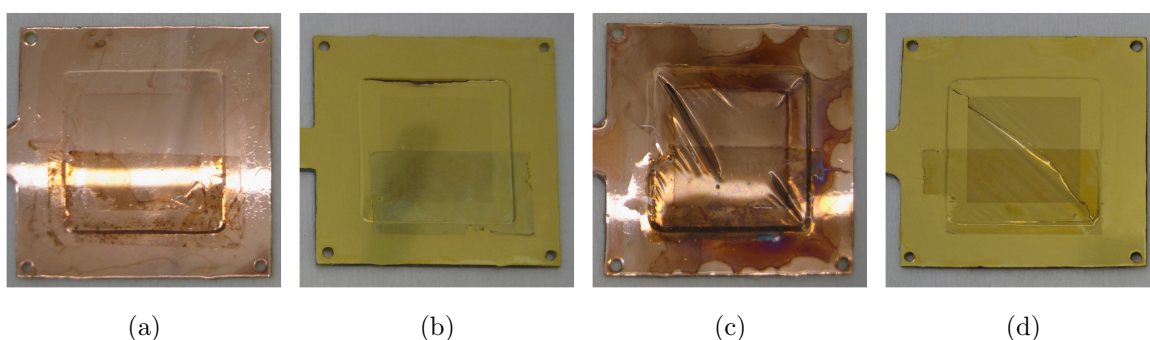
Figure 4.15: Pictures of the meshes covered by an external contractor after unpacking them. Half of the active area of $2.5{\times}2.5\,\text{cm}^2$ is covered with a single layer of graphene. The copper mesh (c) and the mesh with gold finish (d), both with pitches of $60\,\mu\text{m}$, are severely damaged throughout the active area. The gold-covered mesh (c) with a pitch of $120\,\mu\text{m}$ is only damaged on the uncovered side, leading to a non-uniform transparency. Even though requested, neither SEM images nor Raman spectra were supplied by the contractor.

Due to concerns about unavoidable damages to the graphene layer during the transfer process and contaminations with residual PMMA, a second approach to achieve pristine graphene layers was started in parallel. An external contractor, claiming to reach the quality of the layer specified with a PMMA-free transfer process, covered four meshes, one of each type described above. Figure 4.15 shows pictures of all four meshes after the transfer. As can be seen, additionally to severe damage of the meshes themselves, the layer quality is not very uniform. Especially for the copper meshes without a gold finish lots of patches and colour-gradients can be observed all over the graphene layer. The best result, considering the integrity of the supporting mesh, was expected of the copper mesh with a pitch of $120\,\mu$m. The golden mesh with the same pitch was expected to show non-uniformities of transparency due to a crack over one side of the effective area, resulting in the mesh bending towards the conversion volume with the higher field applied.

The meshes were mounted onto a support structure consisting of the support with an opening of $3\times3\,\mathrm{cm}^2$ and a frame with the exact dimensions of the meshes, as is shown in figure 4.14 (b). Holes at the same positions as for the GEM's and drift cathode's frames fixed their position inside the detector with respect to the x- and y-axis.
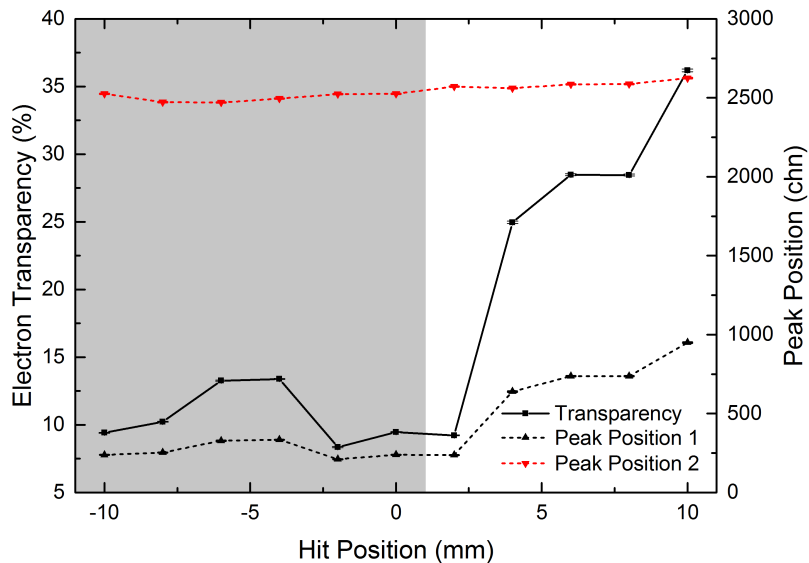
Figure 4.16: Electron transparency of the fourth sample. Peak positions of the signal from the first conversion volume (black) and second conversion volume (red) shown as dashed lines. Estimated position of the graphene layer shown as grey background.

The electron and ion transparencies of the copper mesh with hole diameters of $30\,\mu$m and a pitch of $120\,\mu$m were investigated. Approximately half of the active area of the mesh was covered with a single layer of graphene. The mesh was scanned in horizontal direction from the graphene-covered side to the uncovered side, with the vertical position kept at the centre of the detector. The mesh was irradiated in steps of two millimetres, using a collimated beam
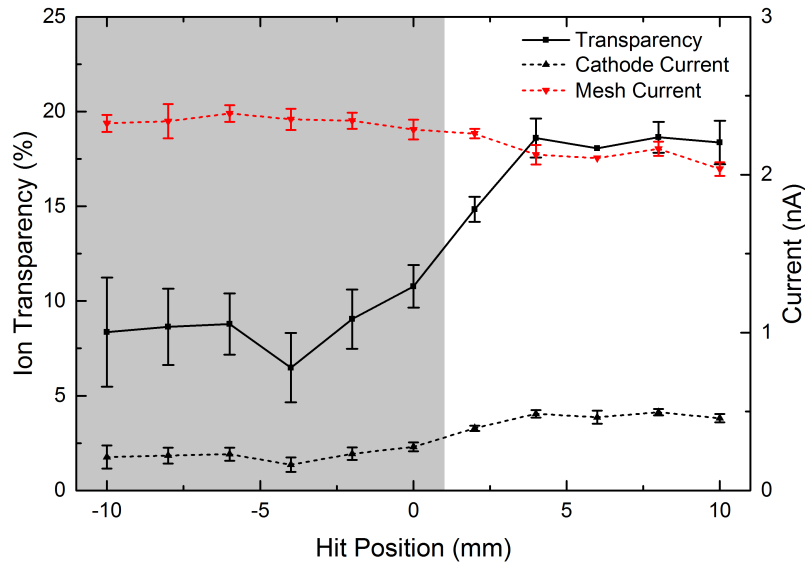
Figure 4.17: Ion transparency of the fourth sample. Currents collected on the cathode (black) and mesh (red) are shown as dashed lines. Estimated position of the graphene layer shown as grey background.

of one millimetre beam diameter. First the electron transparencies were measured, followed by another scan of the ion transparencies. For the electron transparency the fields applied to the two conversion volumes were $20\,\mathrm{V/cm}$ and $800\,\mathrm{V/cm}$, with the detector irradiated with a flux of $2\,\mathrm{kHz/mm}$. The ion transparency was studied using fields of $2400\,\mathrm{V/cm}$ and $400\,\mathrm{V/cm}$ and a flux of $30\,\mathrm{kHz/mm}$.

As is shown in figure 4.16, there is a distinct difference of electron transparency between the covered and uncovered side of the mesh. While the transparency of the uncovered side is about 30% it is reduced to about 10% on the side covered with the graphene layer. The jump in transparency on the layer is due to non-uniform coverage or holes in the layer. The reason for the increased transparency on the last hit position of the uncovered side could not be conclusively determined. The ion transparency, as shown in figure 4.17, was reduced from about 20% to less than 10% on the graphene-covered side.

Measurements on the mesh have proven that there is a difference of both electron and ion transparency of the single-layer graphene as compared to the blank mesh. The transparency of the graphene sample was further investigated as a function of the electron energy by changing the fields applied above and below the mesh, as well as reducing the amount of quencher in the gas mixture.

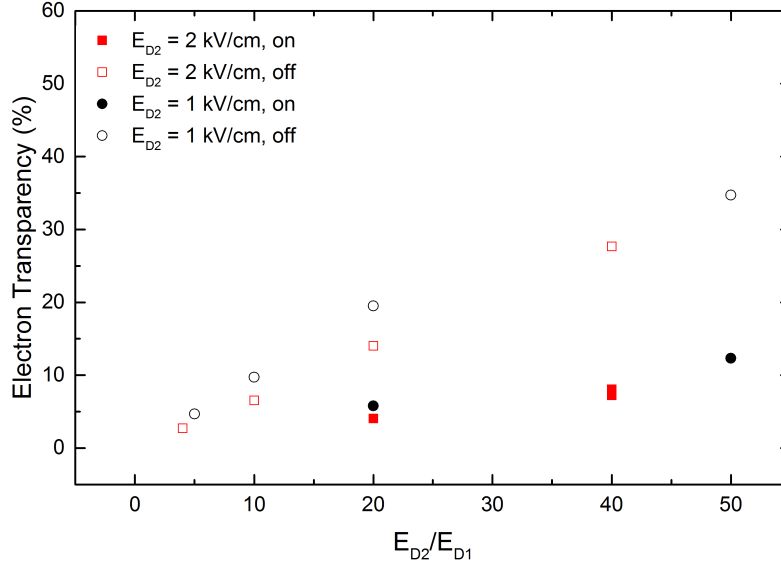**Dependence on electron energy: field ratio**

Figure 4.18: Electron transparency of a copper mesh for different field ratios E_{D2}/E_{D1} and different values of E_{D2}. The mesh had $30\,\mu$m and $120\,\mu$m hole diameter and pitch. The detector was continuously flushed with an Ar/CO_2 90/10 gas mixture at $5\,$L/h. Transparencies of the mesh and graphene layer are shown as open and filled symbols respectively.

As explained in section 4.7.3, the drifting electron energy depends on the electric field applied, with higher energies at larger fields. The field E_{D1} in the first conversion volume was varied to study the electron transmission as a function of the electron energy.

While the drifting electron energy is increased with increasing E_{D1} at a constant field E_{D2} below the mesh, the transparency of the mesh is mostly governed by the field ratio E_{D2}/E_{D1}. Assuming graphene as a perfectly flat conducting plane, the transparency of the mesh covered with the graphene layer on the other hand should not depend on the field ratio E_{D2}/E_{D1}, but only on the electron energy as a function of E_{D1}.

Two hit positions were studied, one on the graphene layer and one on the mesh. Two settings were studied, one with the *Drift* field in the second conversion volume at $E_{D2} = 1\,$kV/cm and one with $E_{D2} = 2\,$kV/cm. The dependence of the mesh and graphene transparency on the field ratio is shown in figure 4.18. For decreasing field ratio the transparency of the uncovered mesh is reduced, caused by a loss of electrons in the first conversion volumes due to attachment at low fields. The transparency for fields $E_{D2} = 1\,$kV/cm is lower compared to those with $E_{D2} = 2\,$kV/cm at the same field ratios E_{D2}/E_{D1} due to the higher probability of attachment at very low fields E_{D1}.

The electron transparency of the graphene layer was found to behave like the uncovered mesh, with the transparency slightly reduced.

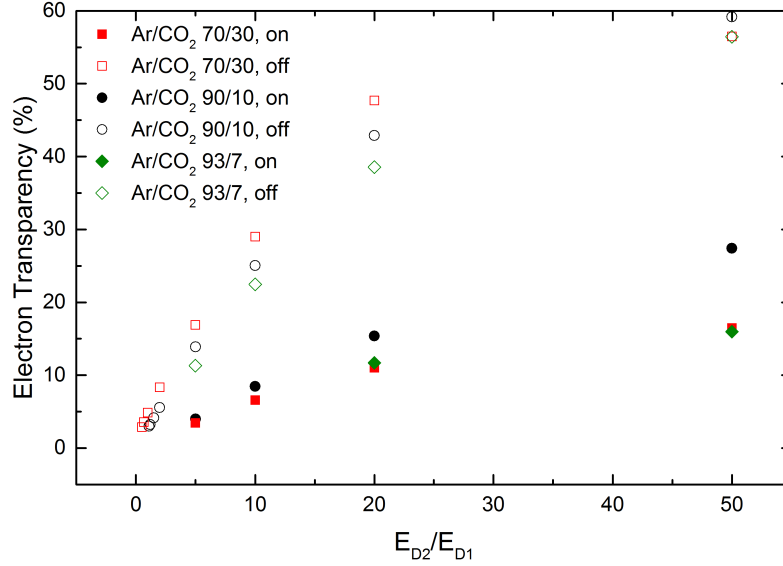**Dependence on electron energy: gas mixture**

Figure 4.19: Electron transparency of a copper mesh for different field ratios of E_{D2}/E_{D1} for constant E_{D2} of $1\,\mathrm{kV/cm}$. The mesh had $30\,\mu\mathrm{m}$ and $120\,\mu\mathrm{m}$ hole diameter and pitch. The detector was continuously flushed with gas mixtures of $\mathrm{Ar/CO_2}$ 70/30 (red), 90/10 (black) or 93/7 (green) at $5\,\mathrm{L/h}$. Transparencies of the mesh and graphene layer are shown as open and filled symbols respectively.

Reducing the amount of quencher in the gas mixture increases the average energy of the drifting electrons, as shown in figure 4.8. Additionally, the diffusion of the electrons in the detector is affected. Two hit positions were studied, one on the graphene layer and one on the mesh. The curves in figure 4.18 show electron transparencies for a gas mixture of $\mathrm{Ar/CO_2}$ in a mass ratio of 90:10. Figure 4.19 shows the transparencies of the mesh and the graphene layers for three different percentages of quencher in the gas mixture. Again, and independent of the gas used, the transparency of the side covered with a graphene layer shows the same behaviour as the uncovered mesh, but with transparencies of decreased values. The transparencies of the mesh decrease with higher contents of argon, owing to the electron diffusion. The $\mathrm{Ar/CO_2}$ mixture of 90/10 yields the best results in terms of electron transparency of the graphene layer, followed by a mixture of 70/30 and 93/7. Since this behaviour is contrary to the one observed on the uncovered mesh it is assumed that damages and non-uniformities of the graphene layer play a role here. Using a collimated beam of half a millimetre diameter and a setup only capable of resolving the hit position with some micrometres accuracy leads to the assumption that not the same position of the graphene layer got irradiated for all curves measured.
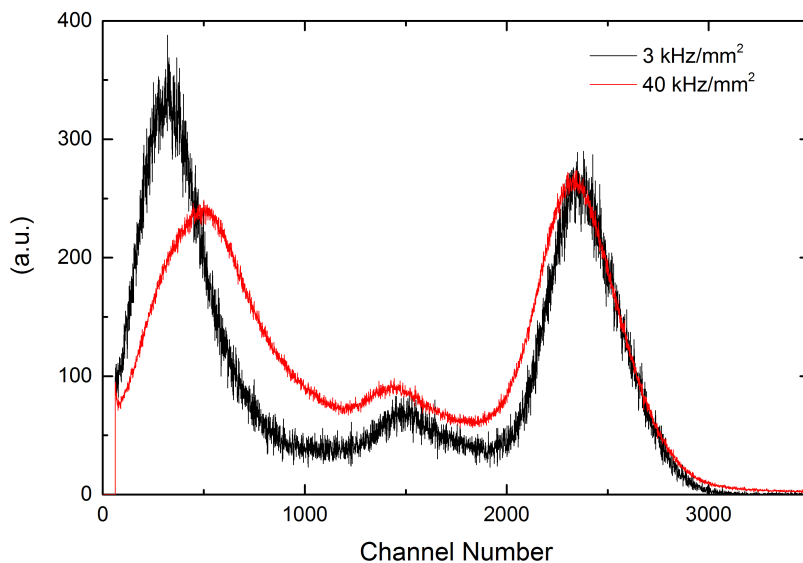
Figure 4.20: Spectra for X-ray fluxes of $3\,kHz/mm^2$ and $40\,kHz/mm^2$ in Ar/CO_2 90/10 gas mixture. Spectra rescaled to equal amplitudes of the full energy peak of the second conversion volume to allow easier comparison of the peak positions. The peak position corresponding to the first conversion volume is increased and the one for the second conversion volume slightly decreased.

Dependence on X-ray flux

A peculiar effect was observed when investigating the electron transparency of the graphene layers. As explained before, to measure the ion transparency, high X-ray fluxes had to be used to achieve observable currents on both the drift cathode and the mesh, uncovered as well as covered with the single layer graphene. The fluxes used to study the ion transparency could not be utilised for the electron transparency measurements due to pile-up of the event by event measurements. Even though the flux was significantly reduced, a strong dependence of the electron transparency on the X-ray flux was observed. As seen in figure 4.20, depicting two pulse height spectra acquired at different fluxes, for a higher flux the transparency of the uncovered mesh increases. The origin of this effect was found to be field distortion in the vicinity of the mesh related to ion space-charge, as is explained in great detail in chapter 3. As is shown in figure 4.21, the field focussing effect, as a function of the X-ray flux increases, bending more field lines into the holes of the mesh. This leads to some restrictions when comparing electron and ion transparencies: while different field configurations are already used to investigate the electron and ion transparencies, the ion transparency measurements are additionally affected by space-charge effects. Results obtained during the electron transparency measurements have to be handled with caution when they are included in the data acquired for ion transparency measurements. Additionally, the comparison of electron transparencies can not be compared when different X-ray fluxes are used in different measurements.
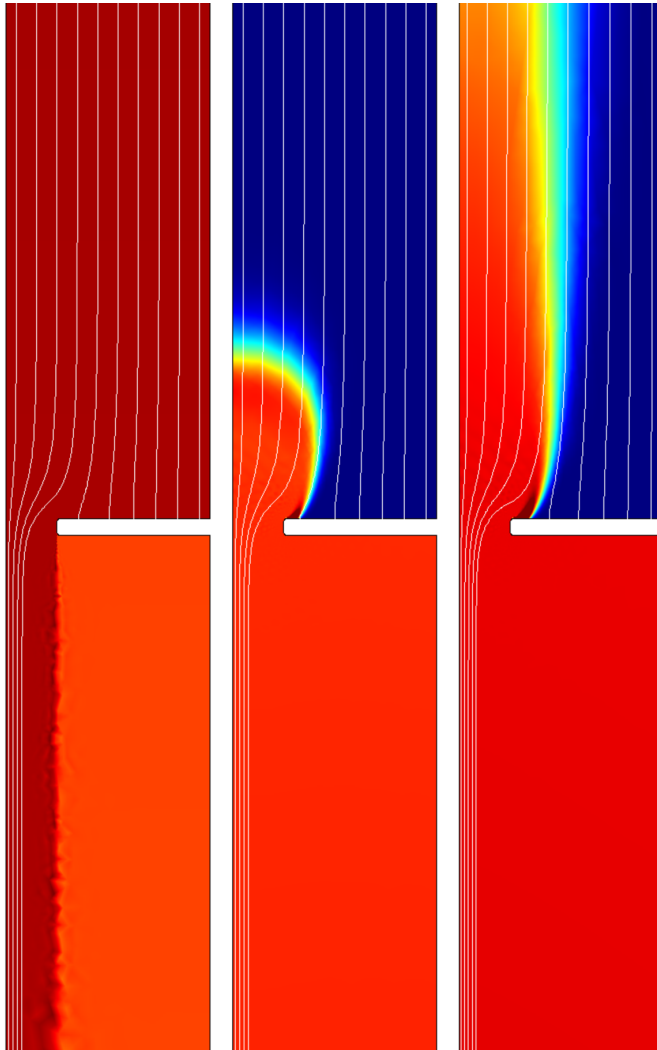
Figure 4.21: COMSOL Multiphysics® simulation of ion densities in the two conversion volumes. The simulations are done with an axial-symmetric 2D model, with the hole of the mesh and those of the three GEMs underneath perfectly aligned. Only a fraction of the two conversion volumes close to the mesh is shown. The fluxes used for the three figures are $0.1\,\mathrm{kHz/mm^2}$, $1\,\mathrm{kHz/mm^2}$ and $10\,\mathrm{kHz/mm^2}$. A detailed description of the model and the computations is found in chapter 3. The field lines get focused into the hole of the mesh (left) due to the fields of $20\,\mathrm{V/cm}$ and $1000\,\mathrm{V/cm}$ applied above and below the mesh. With increasing space-charge due to positive ions accumulating in the volumes, the focusing effect increases (middle) until field lines initially ending up on the mesh are bent into the holes (right). This leads to an increased transparency of the mesh with higher X-ray fluxes, as shown in figure 4.20.

Optical transparency of the mesh

While the electron transparency of a mesh is governed both by the field applied above and below, as well as the diffusion due to the gas mixture used, the ion transparency depends mostly on the fields applied. As shown in figure 4.22 there is a small dependence of the transparency on the gas mixture - generally less transparent for lower amounts of quencher - but the effect is not as strong as the one for electron transparencies shown in figure 4.19. In figure 4.22 two things are observable: first, the ion transparency of the graphene layer is greater than zero for all fields applied, and second, the ion transparencies of both the uncovered mesh and the single layer graphene show a strong dependence on the field ratio. Concluding from the characteristics of graphene in terms of impermeability to ions, these effects seem to be due to small damages of the graphene layer. This assumption is reinforced
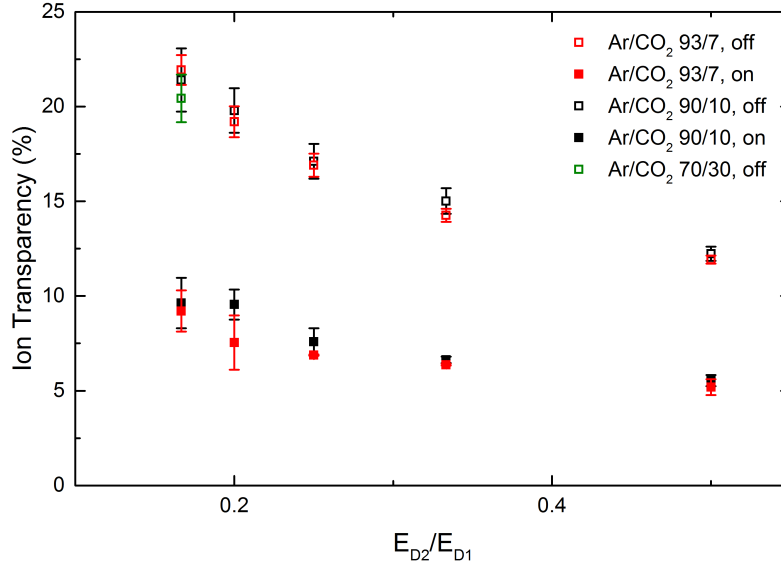
Figure 4.22: Ion transparencies of a copper mesh for different field ratios of E_{D2}/E_{D1} for constant E_{D1} of $2.4\,\mathrm{kV/cm}$. The mesh had $30\,\mu\mathrm{m}$ and $120\,\mu\mathrm{m}$ hole diameter and pitch. The detector was continuously flushed with gas mixtures of $\mathrm{Ar/CO_2}$ 70/30 (green), 90/10 (black) or 93/7 (red) at $5\,\mathrm{L/h}$. Transparencies of the mesh and graphene layer are shown as open and filled symbols respectively.

when looking at the values of electron and ion transparencies achieved: figure 4.19 shows electron transparencies from less than 5% to almost 30% for an $\mathrm{Ar/CO_2}$ 90/10 gas mixture, and figure 4.22 gives ion transparencies from $5\,\%$ to $10\,\%$. Acknowledging graphene as a perfectly flat conductor spanning over all holes of the mesh, there should be no field focussing effect as shown in figure 4.21. The upper limit for the electron and ion transparency should therefore equal the optical transparency of the mesh. With a hole diameter of $30\,\mu\mathrm{m}$ and pitch of $120\,\mu\mathrm{m}$ the optical transparency of the mesh studied was approximately $5.7\,\%$. This value was surpassed both by electrons and ions for almost all values of E_{D2}/E_{D1} in the gas mixtures and fields studied.

4.9   Multi-layer graphene on a GEM-like mesh

Further tests were made to improve the quality of the graphene transfer. After suggesting the use of a critical point dryer [90] to reduce the stress on the layer during the removal of PMMA, results comparable to the ones shown in the previous section were achieved. Since the transfer of charge was still mostly governed by defects in the layer, as shown in figure 4.23, the coverage of the holes by multi-layer graphene instead of single-layer graphene was studied. First trials were done with bi-layer graphene by transferring a second sample of single-layer graphene onto a layer already attached to the mesh. It was demonstrated with several samples that the second graphene layer exhibits defects at the same positions as the supporting
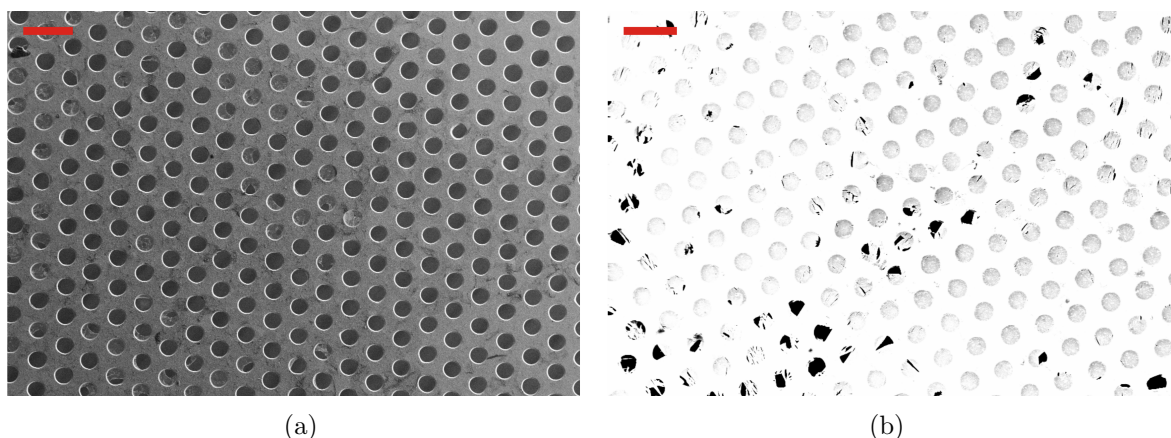
(a)   (b)

Figure 4.23: SEM images of single-layer graphene on copper meshes. Scale bars are $100\,\mu$m. The meshes have a hole diameter of $30\,\mu$m and pitch of $60\,\mu$m. Sample (a) was achieved by by drying the sample in air after removal of the PMMA with acetone, for sample (b) the removal of PMMA was done in a controlled way in a critical point dryer.
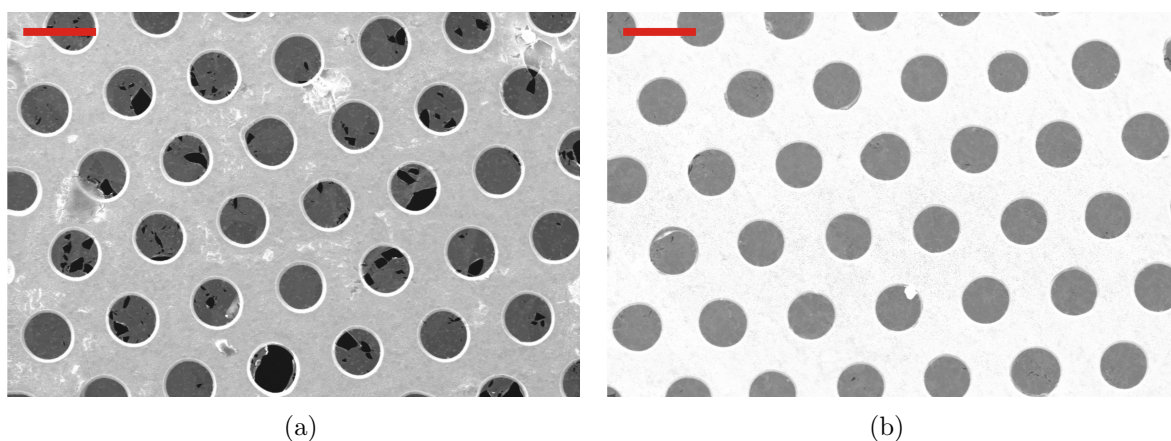

(a)   (b)

Figure 4.24: SEM images of bi-layer graphene on copper meshes. Scale bars are $50\,\mu$m. The meshes have a hole diameter of $30\,\mu$m and pitch of $60\,\mu$m. Sample (a) was achieved by transferring single-layer graphene onto a copper mesh covered with damaged single-layer graphene. Sample (b) was done by transferring single-layer graphene onto a sample of CVD graphene on a copper foil and then transferring both layers at once onto a clean copper mesh.

graphene layer or even damages it further, thus creating additional defects, as shown in figure 4.24 (a). A change of procedure improved the quality of the double-layer: a single layer of graphene was transferred onto the single-layer graphene on its original substrate as purchased by a supplier, and then the two layers were transferred onto a copper mesh in one single step. While the coverage improved drastically, still defects of a few percent of the suspended graphene area persisted, as can be seen in figure 4.24 (b).

(a)	(b)
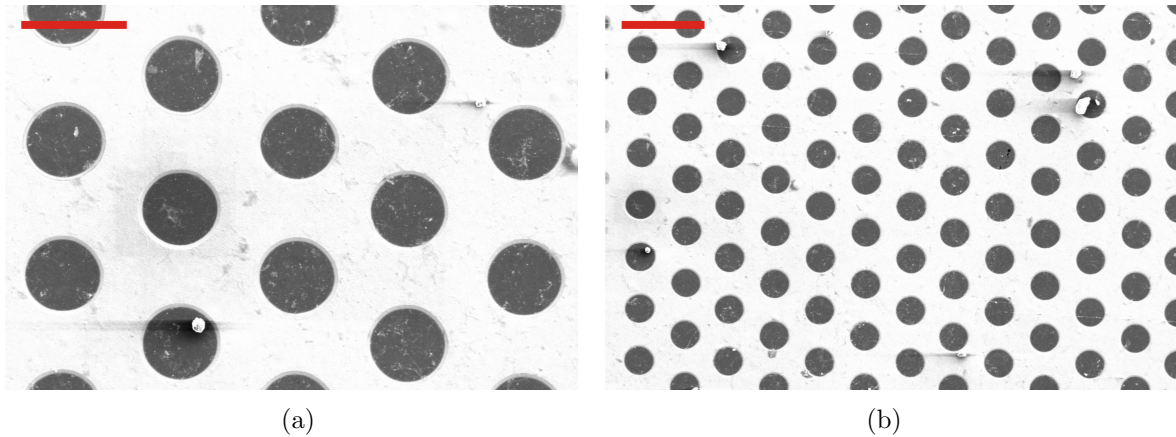
Figure 4.25: SEM images of triple-layer graphene on copper meshes. Scale bars are $50\,\mu$m and $100\,\mu$m. The meshes have a hole diameter of $30\,\mu$m and pitch of $60\,\mu$m. The sample was done by transferring two individual pieces of single-layer graphene onto a sample of CVD graphene on a copper foil and then transferring all three layers at once onto a clean copper mesh.

4.9.1   Triple-layer graphene on a GEM-like mesh

The previously described method of transferring several layers in one step onto a clean copper mesh was used to achieve coverage of a mesh with $30\,\mu$m and $60\,\mu$m hole diameter and pitch with a triple-layer of graphene. Using three layers on a mesh with these dimensions aimed at achieving two things: the optical transparency of the mesh was more than tripled when compared to the previously used meshes, and with three layers of graphene the number of holes in the suspended graphene sheets should be reduced to zero. This allows the investigation of the actual properties of charge transfer through the graphene layers and not through micro-fractures. As can be seen in figure 4.25 an almost perfect coverage with graphene was achieved. The aim of the measurements was to find opaqueness to ions and then change the parameters of the setup to allow electrons to pass through the layers.

The electron transparency was investigated at two different points of the graphene triple-layer. When comparing the uncovered mesh in figure 4.26 with the ones for the meshes previously studied, the higher electron transparency is evident. This is due to the higher optical transparency of about 21% compared to less than 6% in earlier measurements. The electron transparency for both points studied was below the optical transparency of the mesh. While the graphene layer showed some transparency to electrons, the points for lower ratios of E_{D2}/E_{D1} are omitted since a fitting of a Gaussian was not possible. The transparencies were further decreased with decreasing ratio E_{D2}/E_{D1}, being distinguishable as the higher-energetic flank of the Gaussian moving towards lower channel numbers.

The ion transparencies for both the uncovered mesh and triple-layer graphene are shown in figure 4.27. A detail of the graphene transparencies is shown in figure 4.28. Even though the
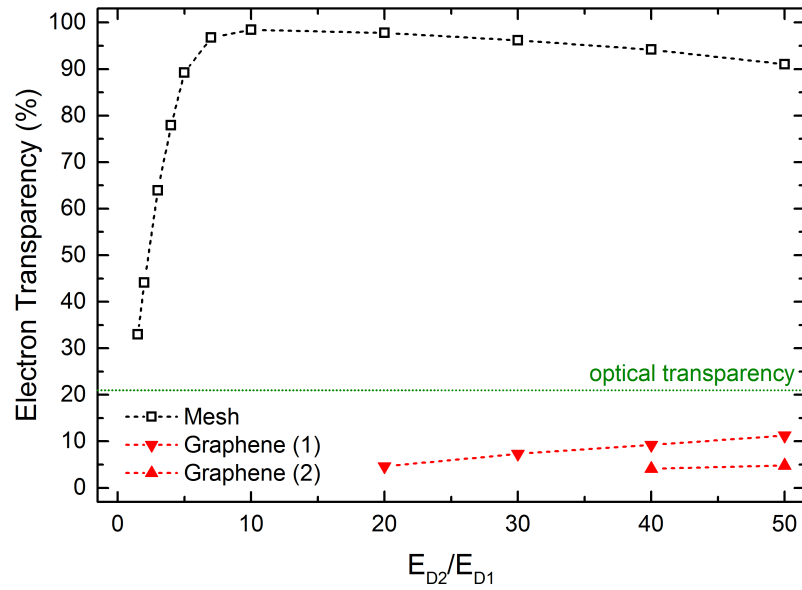
Figure 4.26: Electron transparency of a mesh covered with a triple-layer of graphene for different field ratios of E_{D2}/E_{D1} for a constant E_{D2} of $2\,kV/cm$. The mesh had $30\,\mu m$ and $60\,\mu m$ hole diameter and pitch. The detector was continuously flushed with an Ar/CO_2 70/30 gas mixture at $5\,L/h$. Transparencies of the mesh and graphene layer are shown as contours and filled symbols respectively.
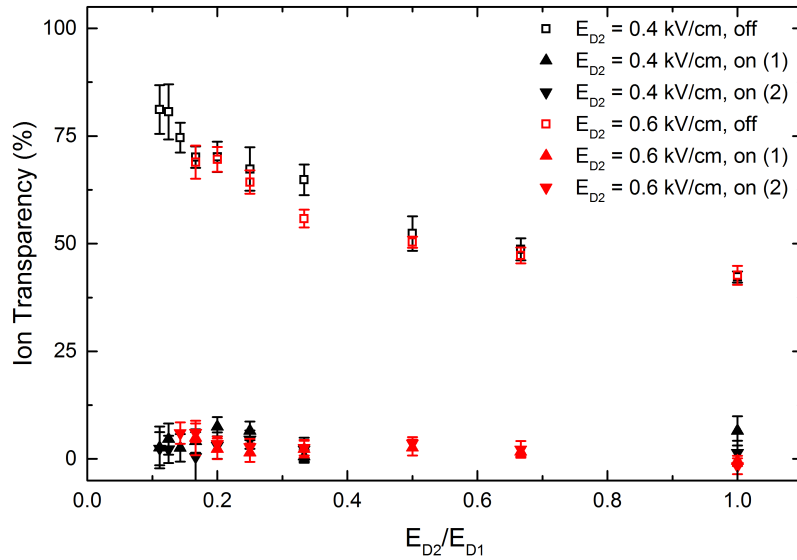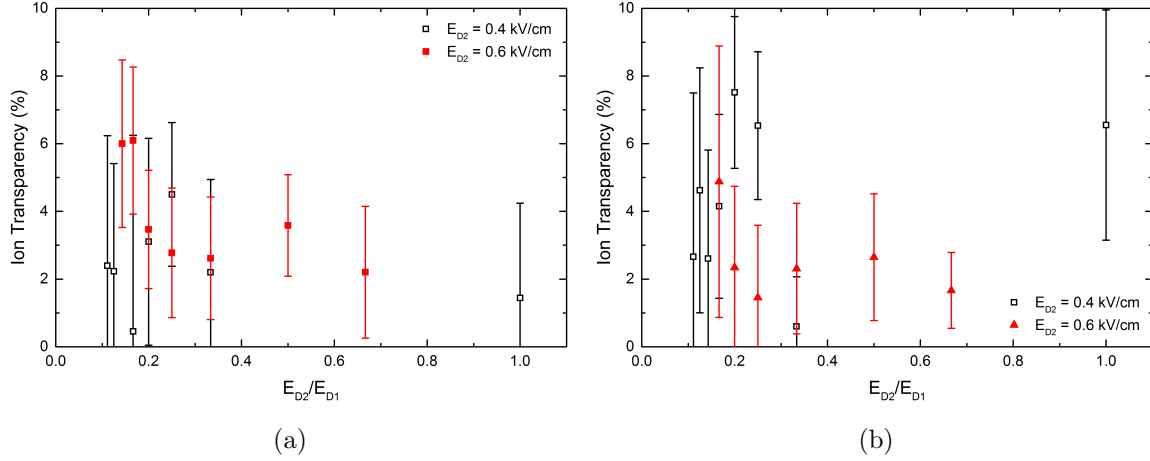

Figure 4.27: Ion transparency of a mesh covered with a triple-layer of graphene for different field ratios of E_{D2}/E_{D1} for a constant E_{D2} of $0.4\,kV/cm$ and $0.6\,kV/cm$. The mesh had $30\,\mu m$ and $60\,\mu m$ hole diameter and pitch. The detector was continuously flushed with an Ar/CO_2 70/30 gas mixture at $5\,L/h$. Transparencies of the mesh and graphene layer are shown as contours and filled symbols (upward for $0.6\,kV/cm$ and downward for $0.4\,kV/cm$) respectively.

(a)

(b)

Figure 4.28: Ion transparency of a mesh covered with a triple-layer of graphene for different field ratios of E_{D2}/E_{D1} for a constant E_{D2} of $0.4\,\mathrm{kV/cm}$ and $0.6\,\mathrm{kV/cm}$. The mesh had $30\,\mu\mathrm{m}$ and $60\,\mu\mathrm{m}$ hole diameter and pitch. The detector was continuously flushed with an Ar/CO_2 70/30 gas mixture at $5\,\mathrm{L/h}$.

ion transparency on the uncovered mesh reached approximately 80% for low ratios E_{D2}/E_{D1}, the ion transparency of the graphene sample was about two or three percent, with large errors. Judging from the changes in both electron and ion transparencies at the two hit positions investigated, non-uniformities in the graphene layers were assumed.

4.9.2   Triple-layer graphene at reduced conversion volume length

To allow higher fields in the first conversion volume, the length of the first conversion volume had to be reduced.

A graphene double layer of about one by two centimetre square was deposited onto a mesh with a hole diameter of $30\,\mu\mathrm{m}$ and pitch of $60\,\mu\mathrm{m}$. The mesh was inserted into the drift volume of a standard triple GEM detector, with the mesh three millimetres above the top electrode of the first GEM. A second mesh with the same hole diameter and a pitch of $120\,\mu\mathrm{m}$ was mounted one millimetre above the graphene covered mesh acting as a drift cathode. The active area of both meshes was $2.5{\times}2.5\,\mathrm{cm}^2$.

To investigate the durability of the setup, aiming at fields of about $10\,\mathrm{kV/cm}$ applied between the drift cathode and the mesh, the double mesh structure was tested prior to being mounted into the detector. The two meshes were assembled with a distance of one millimetre apart and mounted into a test chamber flushed with dry nitrogen (as used for the initial GEM quality assurance explained in section 2.5.2):

1. The graphene mesh was kept at ground potential while applying $1000\,\mathrm{V}$ to the top mesh. The voltage was ramped up in steps of $50\,\mathrm{V}$ and kept constant for about one minute before increasing the voltage by another $50\,\mathrm{V}$. This test made sure that the meshes and

graphene layers can withstand fields of about $10\,\text{kV/cm}$ applied in the *Drift* volume of the triple-GEM detector.

2. Both meshes were powered individually, with an initial voltage of $3900\,\text{V}$ supplied to each of them. While the graphene covered mesh was kept at this voltage, the voltage on the top mesh was again increased in steps of $50\,\text{V}$ to a maximum potential difference of $1000\,\text{V}$. This check ensured that the voltages supplied to both meshes would not damage the setup when the sample was mounted above the triple-GEM operated at an effective gain of about 10^4.
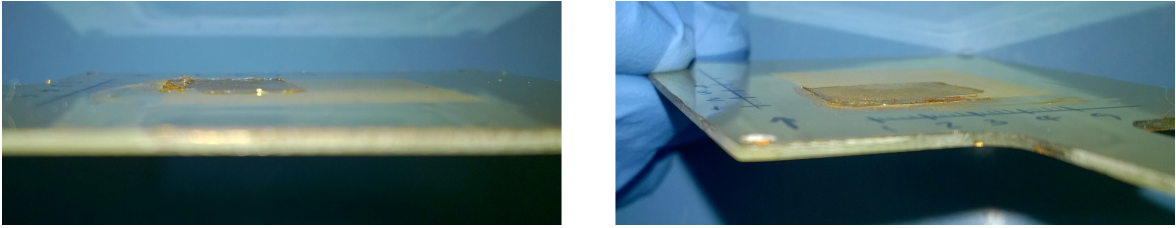
Figure 4.29: Detailed images of the defects surrounding the triple-layer graphene sample. The defects are either damaged graphene, not properly etched copper, or both.

It was found that after applying a voltage difference of about $900\,\text{V}$ a small fraction of the graphene layer detached, leading to a short between the cathode and the mesh. The bad adhesion resulted from a faulty transfer, with parts of the copper support not being fully etched. As can be seen in figure 4.29 the border regions of the graphene layer show additional inhomogeneities. A layer of Kapton$^{\text{TM}}$ was placed on top of the mesh, which covered the defective parts of the graphene layer. The resulting increased gap length was accounted for in an additional stability test for the fields applied, which showed no further problems.

The electron transparency as a function of the field E_{D1} applied between the meshes is shown in figure 4.30. The electron transparency for the mesh was calculated by the peak ratios of the full-energy peaks corresponding to the first and second conversion volume. The peak positions on the graphene-covered side were below what could be resolved by the setup. The transparencies were estimated by the currents collected on the first and second mesh for both the uncovered and the covered part of the mesh, as described in section 4.7.1. For fields up to about $4\,\text{kV/cm}$ in the second conversion volume the electron transparencies calculated with both methods match. For higher fields, it is assumed that the mismatch originates from the fields extending through the holes of the mesh, thus leading to a wrong estimation of the interaction rates in both conversion volumes. The graphene layer shows an increased transparency for low fields E_{D1}.

The ion transparencies are shown in figure 4.31. The transparency of the uncovered side is depending on the fields applied. The transparency of the graphene triple-layer shows a small dependence on the field for $E_{D1} \geq 5\,\text{kV/cm}$. Comparing the behaviour of both the electron
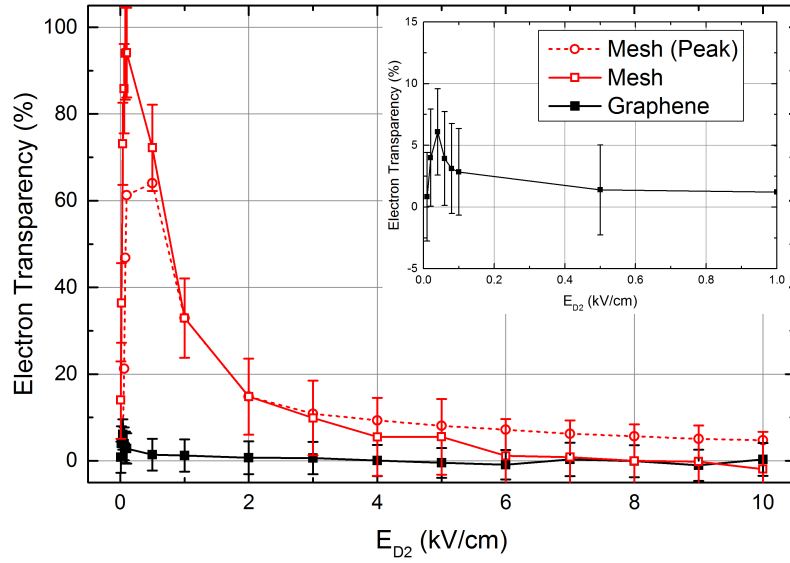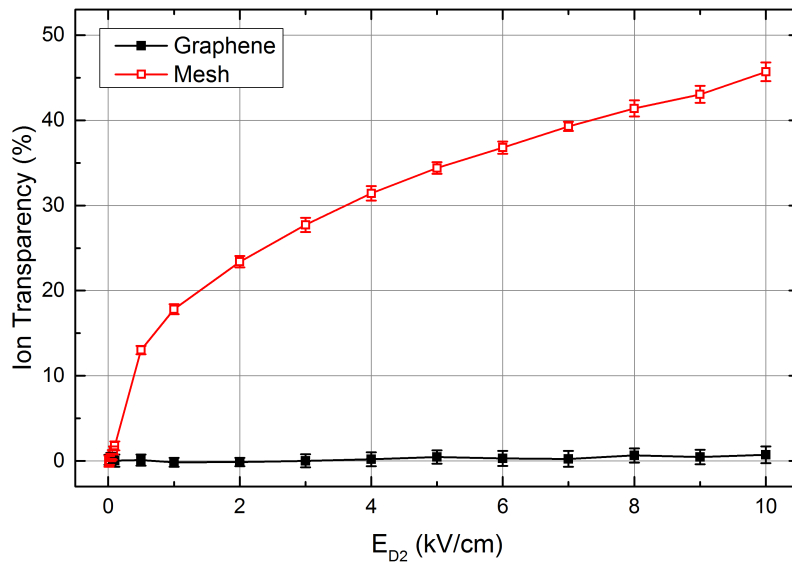
Figure 4.30: Electron transparency of a GEM-like mesh with $30\,\mu m$ hole diameter and pitch of $60\,\mu m$ partly covered with a triple-layer of graphene. The field E_{D2} was kept constant at $2\,kV/cm$, the field E_{D1} was varied between $0.1\,kV/cm$ and $10\,kV/cm$. The detector was continuously flushed with an Ar/CO_2 70/30 gas mixture at $5\,L/h$. The transparencies of the mesh and graphene layer are shown as contours and filled symbols respectively. The transparency of the mesh was additionally calculated by peak ratios.

Figure 4.31: Ion transparency of a GEM-like mesh with $30\,\mu m$ hole diameter and pitch of $60\,\mu m$ partly covered with a triple-layer of graphene. The field E_{D2} was kept constant at $2\,kV/cm$, the field E_{D1} was varied between $0.1\,kV/cm$ and $10\,kV/cm$. The detector was continuously flushed with an Ar/CO_2 70/30 gas mixture at $5\,L/h$. The transparencies of the mesh and graphene layer are shown as contours and filled symbols respectively.

and ion transparency leads to the assumption of small defects which were not visible with the fields reached before.

4.10 Measurements on a GEM

Even though the ion back-flow through the layer was favoured by the field configuration used, the layer was assumed to block ions efficiently. On the other hand, even at very high field ratios E_{D2}/E_{D1} almost no electrons were passing through the layer. Since the electron energy could not be increased further with the setup used, additional tests were conducted with graphene layers suspended over the holes of the *bottom* electrode of a GEM. As explained before, with the field above a mesh increased too much, the transparency suffers a significant loss. The fields in the GEM holes of an order of $10\,\mathrm{kV/cm}$ would increase the electron energy while at the same time still keeping a good transparency of the device due to the field lines being focused into the holes of the GEM.

4.10.1 Experimental setup
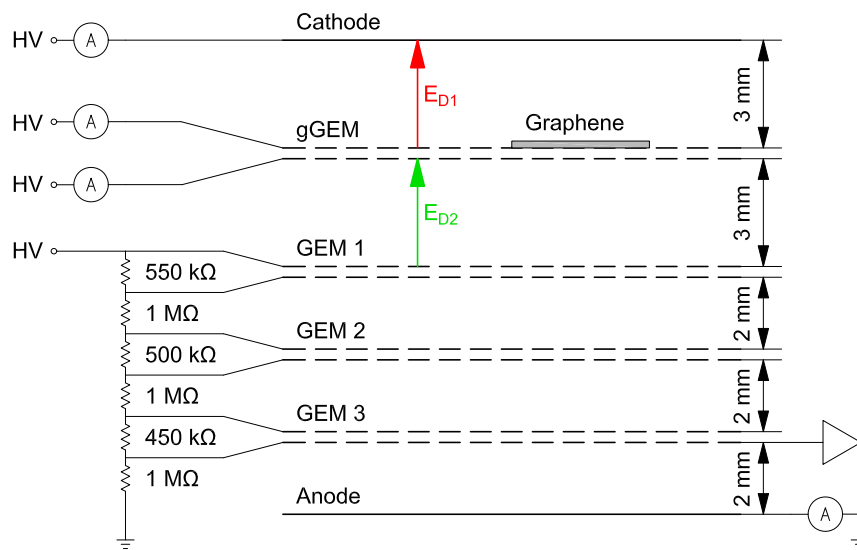
Figure 4.32: Setup for the measurements on a graphene-covered GEM (gGEM). The graphene layer is transferred onto the top or bottom electrode of the gGEM. The setup shows the graphene layer on the top electrode of the gGEM. The voltages on cathode and both electrodes of the gGEM are powered individually. The triple-GEM is powered via a resistor divider.

The setup previously used was modified to comprise a GEM instead of the mesh, as shown in figure 4.32. Both electrodes of the GEM were powered individually, to allow a selection

of the potential difference between the electrodes. The currents of the electrodes were read
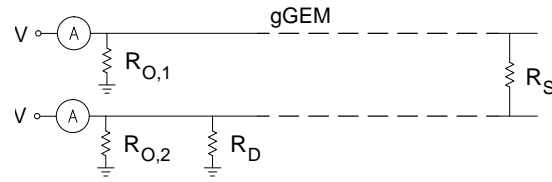with the high current resolution ammeters of the high-voltage power supply.

Figure 4.33: Detail of the powering scheme for a gGEM with a short (R_S) between the
GEM electrodes. Both gGEM electrodes are connected to ground with a resistor of $R_{O,i}$ of
approximately $5\,G\Omega$ to supply an offset in the current monitor. An additional resistor R_D is
added to the bottom electrode to drain most of the current from the short to ground. R_D is
chosen to operate the power supply within the current and power output limits.
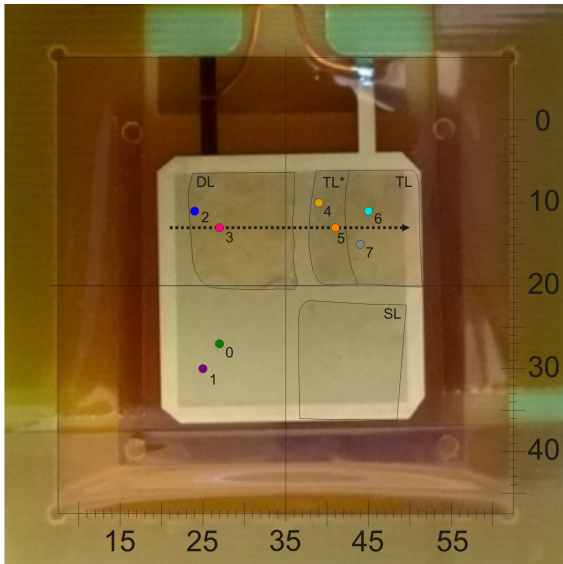
Figure 4.34: The gGEM after mount-
ing it in the detector. The positions of
the single-layer (SL), double-layer (DL)
and triple-layer (TL), and the part of the
triple-layer damaged during the transfer
process (TL*) are marked by black bor-
ders. The coloured circles show the es-
timated size and hit-positions of the X-ray
beam and refer to figures 4.35 and 4.36.
A scan over the double- and triple-layer
graphene was done where indicated by the
dashed line. Scale in millimetres and with
respect to the detector support.

Single-layer, double-layer and triple-layer graphene, one sample with an area of $1{\times}1\,cm^2$
each, was transferred onto a *standard* GEM with an active area of $3{\times}3\,cm^2$. The GEM with
the graphene layers deposited on its surface (gGEM) are shown in figure 4.34. Inspection of
the layers both by optical and electron microscopy after the transfer showed a coverage with
single-layer graphene of less than 70%, the coverage of the other two samples was better than
99%. A fraction of the triple-layer was damaged during the transfer process.

Before mounting the gGEM in the detector it was observed that a short of $200\,k\Omega$ occurred
between the two electrodes. To achieve sufficient potential differences in the gGEM the bot-
tom electrode was connected to ground with $1.6\,M\Omega$ to operate the detector within the limits
of the power supply (figure 4.33, resistor R_D). Due to the higher consumption of current
and therefore lowered current resolution of $50\,nA$ no ion transparency measurements could
be conducted.

Previous measurements lead to the assumption that already damaged graphene sheets might

get loose during discharges and damage the triple-GEMs underneath the sample under investigation. To reduce this risk, the samples were first to be assessed with the graphene-covered electrode facing towards the drift cathode. After successful operation the gGEM was to be flipped upside down, with the covered electrode now facing the triple-GEM and read-out board.

The electron transparency of the gGEM was measured at voltage differences of 0 V to 90 V applied between the electrodes. The fields were not further increased to only study the transparency of the gGEM wihout the occurance of electron multiplication. The detector was operated at an effective gain of approximately $12{\times}10^3$, with fields of 50 V/cm and 1000 V/cm applied above and below the gGEM. Two positions on the uncovered gGEM, the triple-layer and the double-layer graphene were investigated. Additional two points on the damaged triple-layer were studied, one close to the sample border and one centred in the damaged part. The single-layer was not studied due to its bad coverage. The selected positions were irradiated with a collimated beam of about one millimetre diameter from a copper X-ray tube.
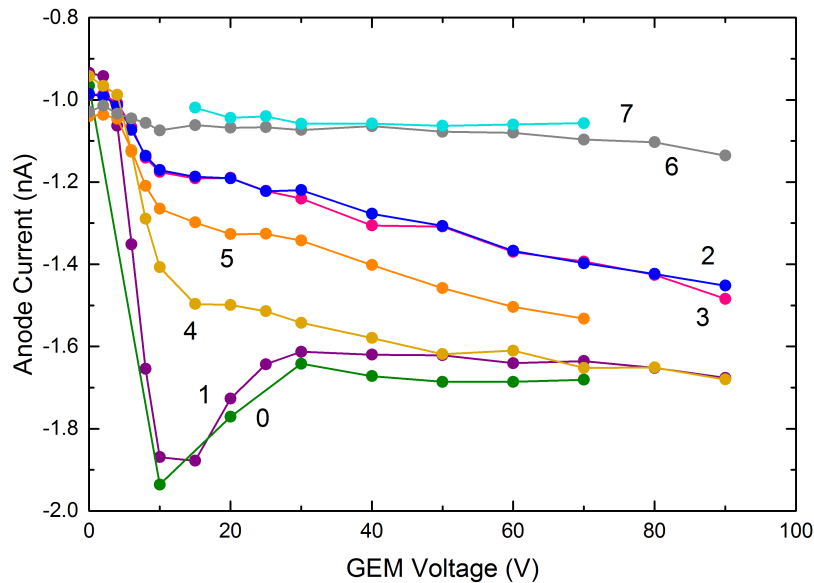
4.10.2 Results

Figure 4.35: Currents collected on the read-out anode for the hit positions investigated. Colours and numbers refer to figure 4.34. All curves show a steep increase of collected current above a voltage of 5 V applied across the GEM. The two curves acquired for each number of (undamaged) layers show similar behaviour, with the ones on the uncovered gGEM haveing the greatest deviations from one another.

Figure 4.36 shows an overlap of both curves recorded for each number of layers, with the curves of the damaged triple-layer graphene either showing a strong resemblance to the
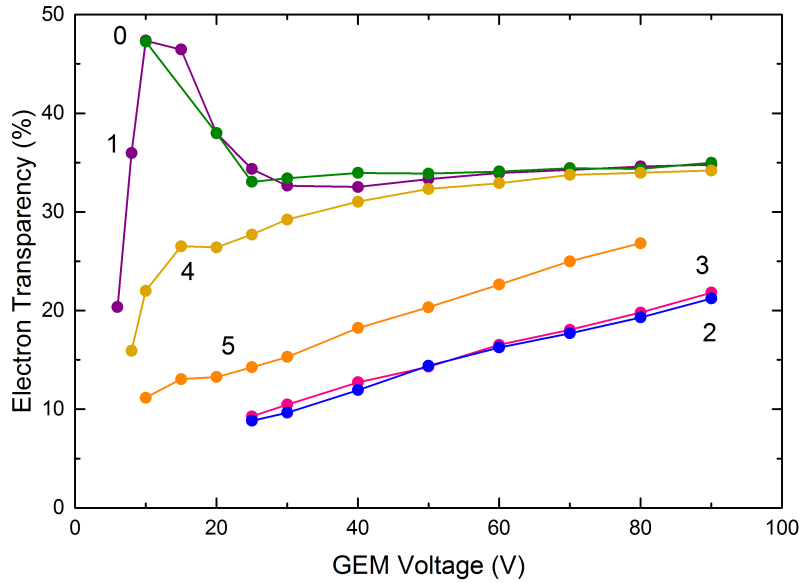
Figure 4.36: Electron transparency of the hit positions investigated. Colours and numbers refer to figure 4.34. The reference positions *1* and *2* show highest transparency between 10 V and 20 V potential difference between the gGEM electrodes. Curves *6* and *7*, acquired on the triple-layer are omitted since their transparency is below what could be resolved.

uncovered gGEM or slightly higher transparency than the double-layer. The two hit positions on the undamaged triple-layer showed no transparency to electrons in the pulse-height spectra acquired. Judging from the currents read on the anode in figure 4.35, hit position *6* shows a small increase in transparency at very high fields, which could not be recognised in the pulse-height spectrum. The other curves taken on the same graphene sample are again overlapping, with only the damaged triple-layer showing resemblance to the uncovered gGEM or the double-layer graphene. For some curves the data acquisition was stopped before reaching a value of 90 V due to the occurrence of discharges.

After two arbitrary points on each number of layers showed approximately the same electron transparency, it was investigated if a uniform coverage with graphene layers was achieved. A voltage difference of 50 V was selected for a one-dimensional scan over both the double-layer and triple-layer graphene. Figure 4.37 shows the electron transparencies acquired in steps of one millimetre each, with the transparencies of the double-layer graphene and the uncovered gGEM as references. The electron transparencies on the double layer show equal or less transparency to electrons compared to the reference point. Between the hit position of 29 mm and the border of the graphene sample an increased transparency attributed to defects was observed. The damaged triple-layer shows higher transparency than the double-layer, with the undamaged part showing less electron transparency than what could be resolved with the setup used.

In addition to the one-dimensional scan, a full map of the transparency was acquired.
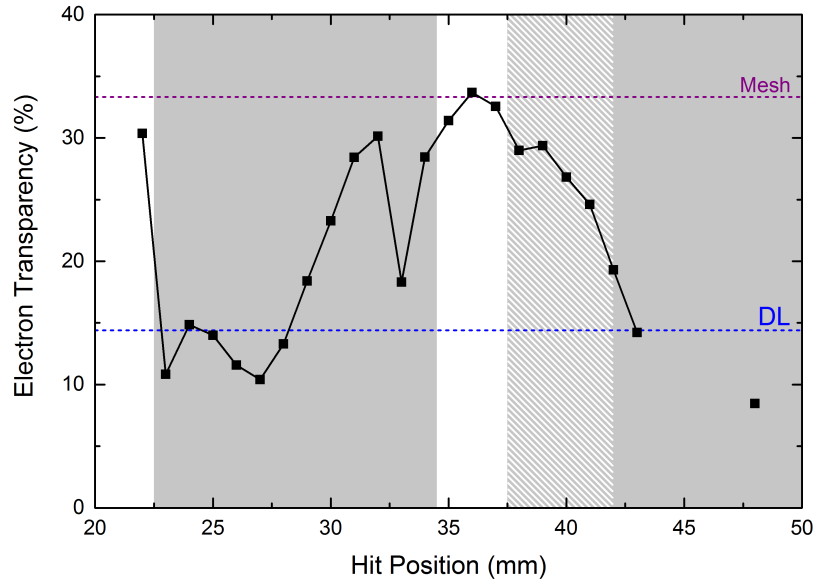
Figure 4.37: Electron transparency scan over the line indicated in figure 4.34. Transparencies of points *1* (Mesh) and *2* (DL) shown for reference. Positions of the graphene layers shown as grey background, with the damaged part of the triple layer as a striped pattern.
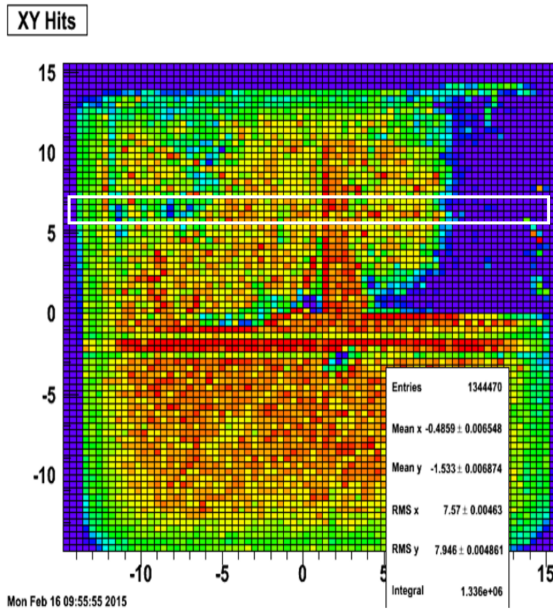

Figure 4.38: Two-dimensional study of the electron transparency of the gGEM operated at 50 V potential difference between the two electrodes. Signals from both conversion volumes are plotted, resulting in the appearance of the inactive area of the gGEM as a green border around the area studied. The scanned area of figure 4.37 is shown as a white rectangle. Scale in millimetres and with respect to the centre of the detector.

The detector was operated at a gain of about 3×10^3, with fields of 50 V/cm and 1000 V/cm in the first and second conversion volume, and a voltage difference of 50 V applied across the gGEM. The gGEM was fully irradiated with an uncollimated X-ray beam of 8 keV and a two-dimensional image acquired with each strip read individually. Figure 4.38 shows a two-dimensional histogram of counts acquired per strip. The method proves that the layers again are not uniform, and the reference positions picked for a point-wise investigation by chance were of better quality than most of the layer. For the fields applied it is shown that without

accelerating the electrons prior to reaching the graphene membrane there is no transparency achievable by using three layers of graphene. The double-layer showed reduced transparency in some parts of the sample, but judging from the dependence on the field applied below the graphene these were most likely due to defects.

Due to a terminal failure of the detector prior to turning the gGEM no further results could be achieved to clarify the subject with the current sample.
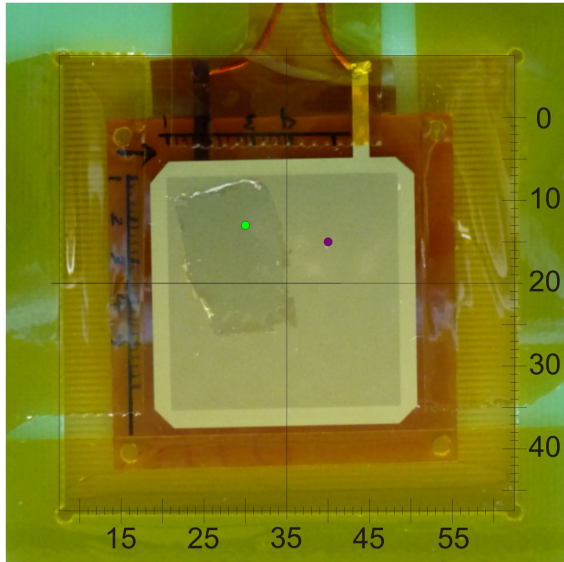

Figure 4.39: Hit positions on the second gGEM. The position of the triple-layer graphene is evident, mostly due to folded graphene layers (top and left) and bad graphene transfer (bottom and bottom right). Two arbitrary positions were investigated, one on the graphene layer and one on the uncovered GEM electrode. Scale in millimetres and with respect to the detector support.

Triple-layer graphene was transferred onto another GEM with the same specifications as before. The gGEM with the graphene layers deposited on its surface is shown in figure 4.39. The gGEM was mounted in the detector with the graphene layer facing towards the read-out anode. During initial tests on two hit positions, one on the uncovered gGEM and one on the graphene layer, it was found that the transparency of the uncovered gGEM was highest at 80 V applied between the two electrodes, deviating from the expected value of about 20 V as shown in figure 4.36. The graphene layer showed a transparency of less than 3% for this value. It was found that the voltages applied to the GEM were deviating from the ones attempted due to a short of about $30\,\mathrm{M\Omega}$ across the gGEM, which only occurred after mounting the gGEM into the detector. After returning to the setup with an additional resistor connected to ground to drain current from the short, further tests were conducted. The curve acquired for the uncovered side again resembled the one already shown. During several discharges while investigating the transparency of the graphene layer both the gGEM and the triple-GEM were severely damaged. The gGEM was shorted with $5\,\mathrm{k\Omega}$ between the electrodes and the triple-GEM was discharging continuously. Trying to recover the gGEM failed.

As is evident from figure 4.39 there were defects on the borders of the graphene layer. Concluding from previous measurements and unsuccessful transfers done before these damaged parts of the graphene sample are creating a conductive bridge between the electrodes of the gGEM, rendering it useless for most of the measurements. To bypass this problem,
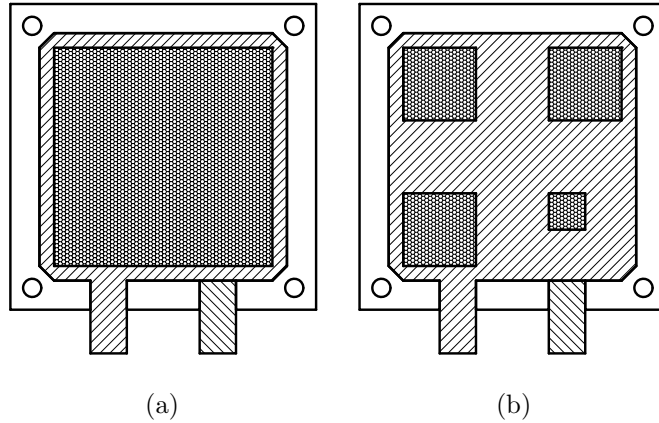
Figure 4.40: Layout of a standard 3×3 cm^2 GEM (left) and the modified version for graphene transfer (right). The honeycomb pattern represents active area with double conical holes, the electrodes are shown as a striped pattern.

the layout of the gGEM was changed to have one centimetre of inactive area between the holes covered by the graphene and the ones used for reference measurements, as shown in figure 4.40. This is supposed to make sure that any defects on the border of the sample stay attached to one side of the gGEM and thus reducing the risk of damages before and during operation.

The measurements on these new gGEMs are not part of this work due to delays in both the manufacturing process of the new gGEMs and the supply of additional graphene samples.

4.11 Conclusions and outlook

For the first time graphene layers were used in combination with micro-pattern gaseous detectors to measure its permeability to electrons and ions at low energies. Methods were developed to measure the transport properties through graphene layers of various area and thickness, freely suspended within a gas-filled detector volume.

Well-known graphene transfer techniques were adapted to create freely suspended graphene sheets of sizes more than an order of magnitude larger than what is commonly used in other applications, as for example transfer electron microscopy. Additionally, a transfer-less method was developed to create suspended graphene sheets on a copper support structure. First results were promising, but need further refinement before being used in gaseous detectors.

Measurements on single-layer graphene samples showed a not negligible amount of defects, giving rise to transfer properties mainly due to the defects and not due to charge transfer properties through pristine graphene. Graphene double-layers and triple-layers were produced, stacking individual sheets of single-layer graphene on top of each other, and effectively transferred, achieving a very high overall coverage of the holes. The studies performed prove the methods developed are suitable even though the evaluation of the graphene transparency is

complicated by sample defects. The results obtained for the produced multi-layer graphene, suspended freely in the holes, hint towards a non-permeability to electrons and ions at the energy ranges typically occurring in the transfer regions of gaseous detectors. The reason for this is most probably found in the increased spacing between the layers and random misalignment with respect to each other, resulting from the transfer of artificially stacked graphene multi-layers. This leads to the graphene samples not behaving as theoretically described graphene and thus blocking the electrons from effectively tunnelling through the layers. Directly grown samples of multi-layer graphene might solve the problem.

Graphene layers were successfully transferred onto the electrodes of a GEM. Problems arising during operation result in graphene patches shorting the electrodes, thus rendering the samples useless. A refinement of the setup has been done to overcome these challenges. Transferring multi-layer graphene onto the refined GEM electrodes will allow a conclusive study of the transfer properties over a wider range of electron energies.

Appendix A

Additional results

Figures A.1 and A.4 show pulse height spectra acquired at *nominal* effective gains of $5{\times}10^3$ and $10{\times}10^3$, as explained in section 3.4.2.

Figures A.2 and A.3, and figures A.5 and A.6 show 2D histograms of the pulse height spectra depicted in figure A.1 and A.4. For easier comparison with the data shown in figures 3.33 and 3.34 the respective histograms acquired at the same X-ray fluxes are shown with grey squares.
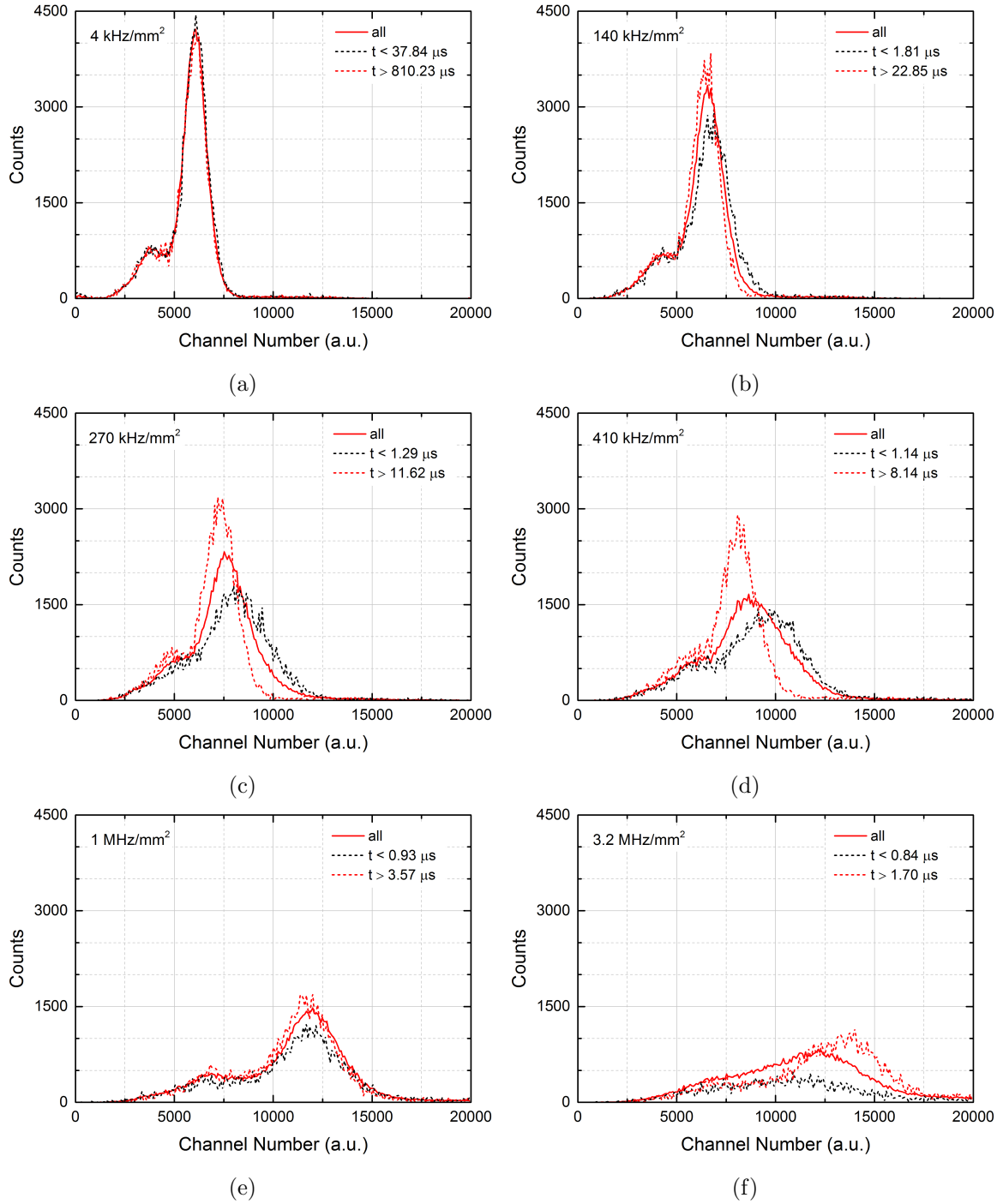
Figure A.1: Pulse height spectra for different X-ray fluxes (solid) and fractions of pulse height spectra depending on the time to the previous trigger (dashed). Dashed spectra are scaled by a factor of 10 for easier comparison. For explanations see section 3.4. The detector was operated at a *nominal* effective gain of 5×10^3. Spectra were acquired for X-ray fluxes of $4\,\mathrm{kHz/mm^2}$ (a), $140\,\mathrm{kHz/mm^2}$ (b), $270\,\mathrm{kHz/mm^2}$ (c), $410\,\mathrm{kHz/mm^2}$ (d), $1\,\mathrm{MHz/mm^2}$ (e), and $3.2\,\mathrm{MHz/mm^2}$ (f).
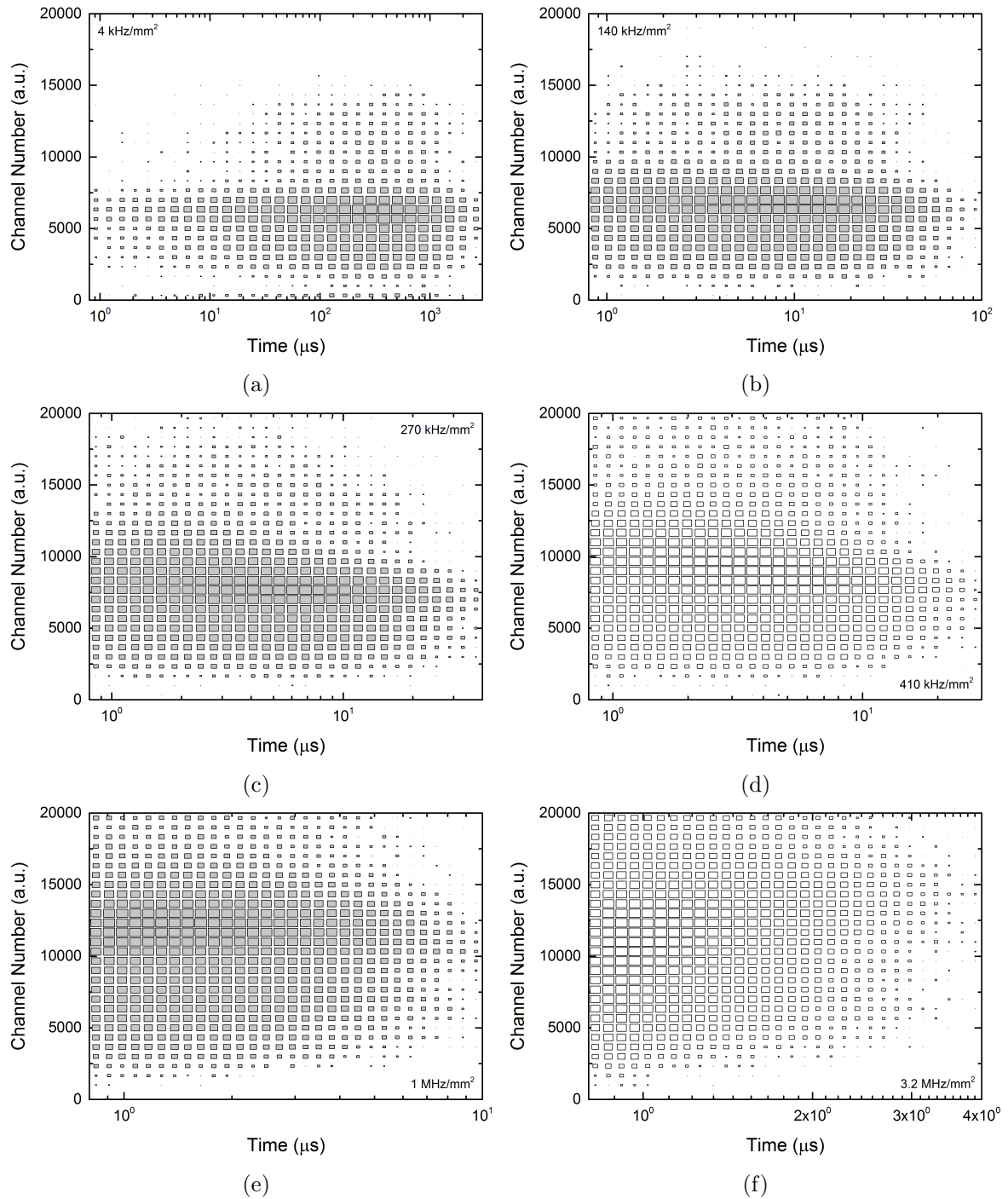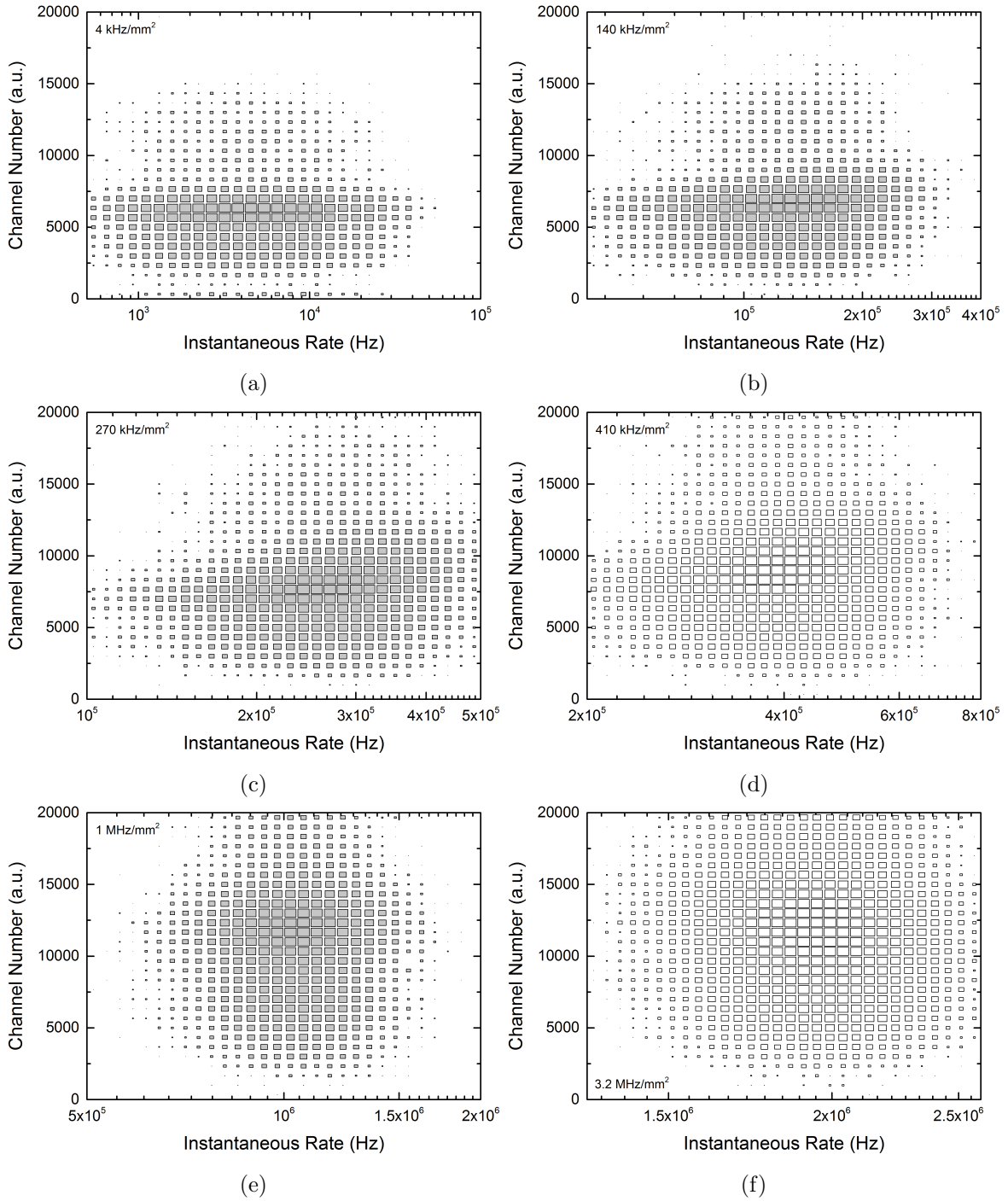
Figure A.2: Dependence of charge integral on the time to previous trigger. The plot shows a 2D histogram of the pulses acquired for figure A.1. The area of each rectangle represents the squared counts per bin and is normalized to the largest number of counts. The detector was operated at a *nominal* effective gain of 5×10^3. Plots were acquired for particle fluxes of $4 \, \text{kHz/mm}^2$ (a), $140 \, \text{kHz/mm}^2$ (b), $270 \, \text{kHz/mm}^2$ (c), $410 \, \text{kHz/mm}^2$ (d), $1 \, \text{MHz/mm}^2$ (e), and $3.2 \, \text{MHz/mm}^2$ (f).
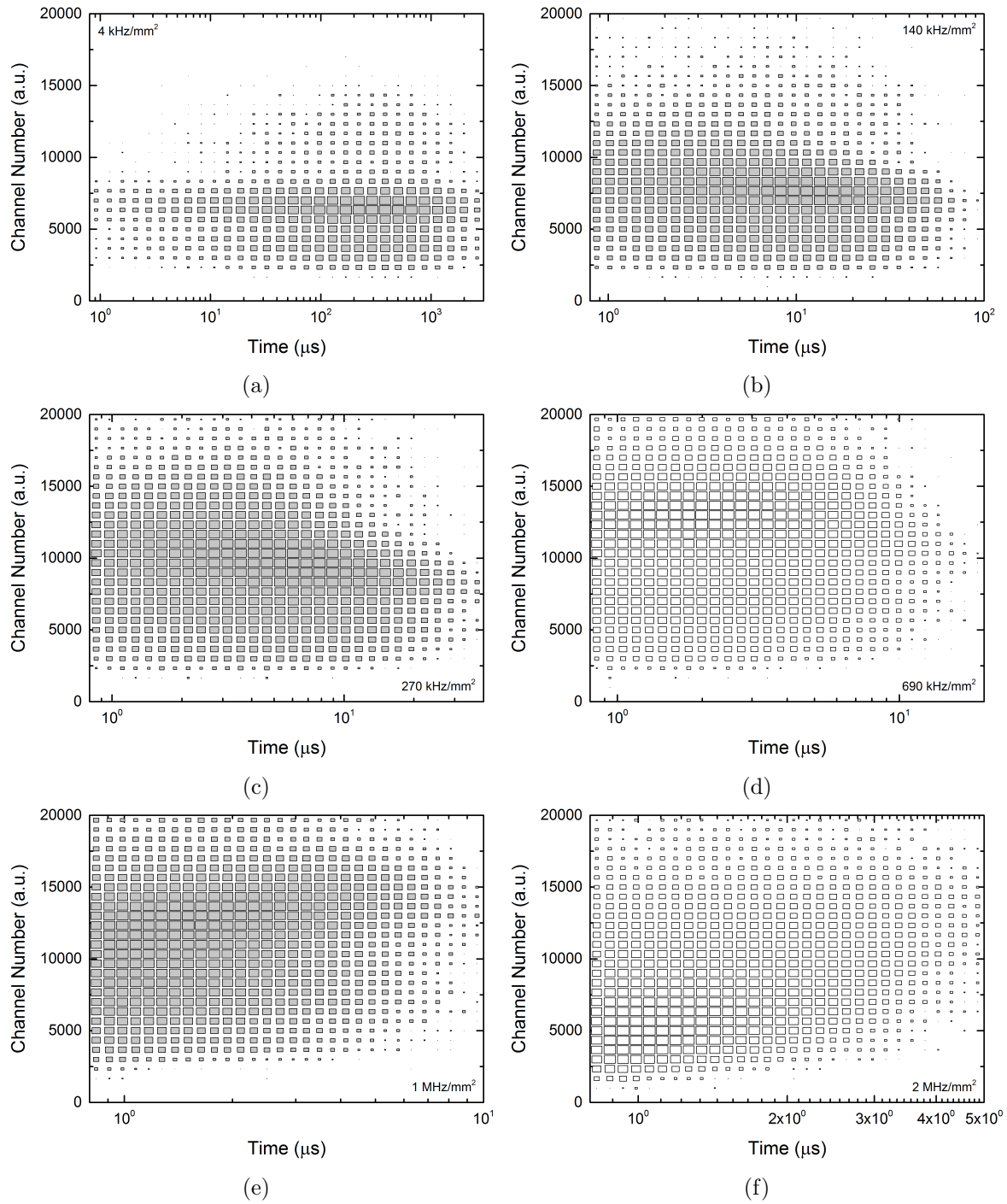
Figure A.3: Dependence of the charge integral on the instantaneous rate. The plot shows a 2D histogram of the pulses acquired for figure A.1. The area of each rectangle represents the squared counts per bin and is normalized to the largest number of counts. The detector was operated at a *nominal* effective gain of $5{\times}10^3$. Plots were acquired for particle fluxes of $4\,\mathrm{kHz/mm^2}$ (a), $140\,\mathrm{kHz/mm^2}$ (b), $270\,\mathrm{kHz/mm^2}$ (c), $410\,\mathrm{kHz/mm^2}$ (d), $1\,\mathrm{MHz/mm^2}$ (e), and $3.2\,\mathrm{MHz/mm^2}$ (f).
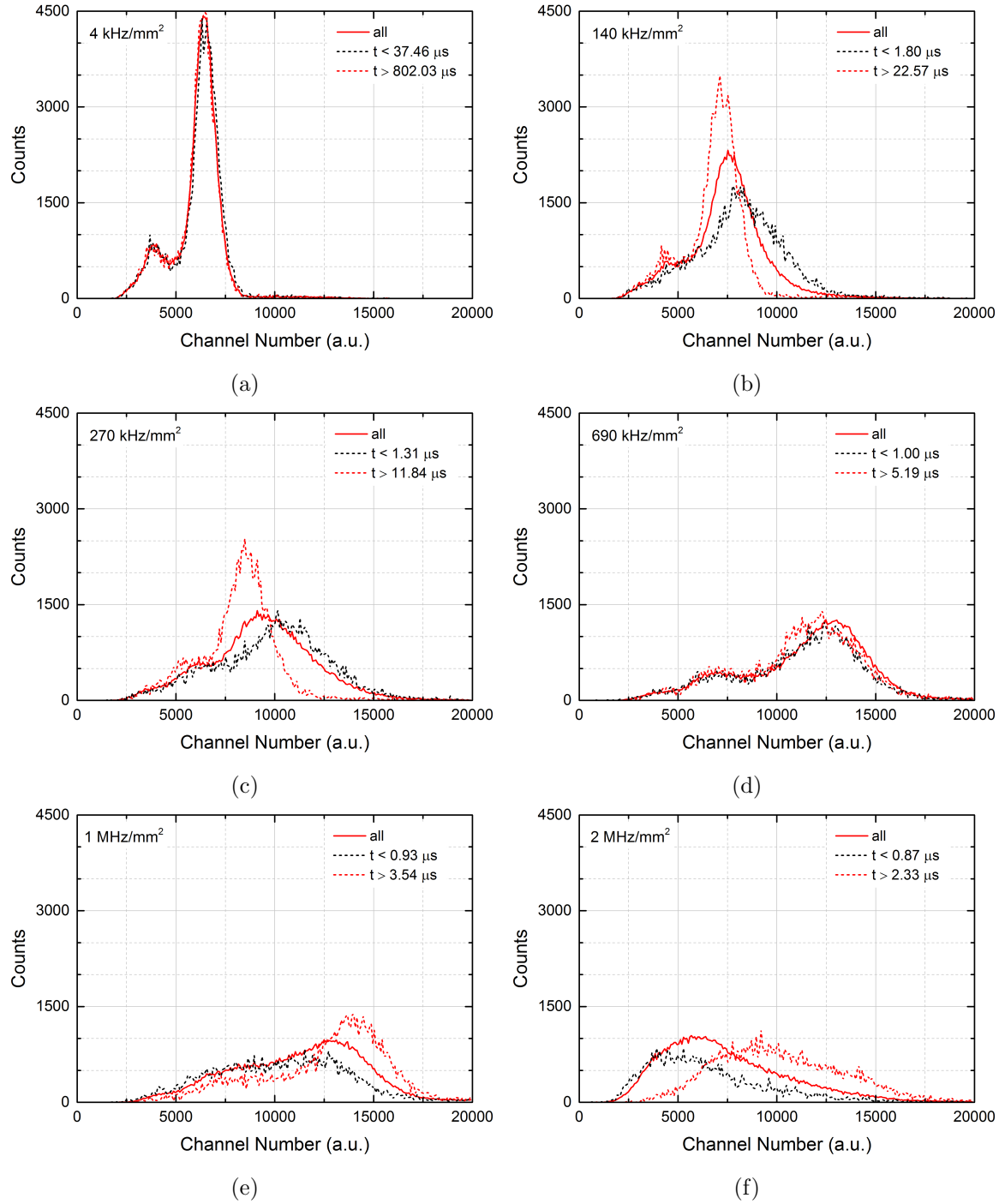
Figure A.4: Pulse height spectra for different X-ray fluxes (solid) and fractions of pulse height spectra depending on the time to the previous trigger (dashed). Dashed spectra are scaled by a factor of 10 for easier comparison. For explanations see section 3.4. The detector was operated at a *nominal* effective gain of 10×10^3. Spectra were acquired for X-ray fluxes of $4\,\mathrm{kHz/mm^2}$ (a), $140\,\mathrm{kHz/mm^2}$ (b), $270\,\mathrm{kHz/mm^2}$ (c), $690\,\mathrm{kHz/mm^2}$ (d), $1\,\mathrm{MHz/mm^2}$ (e), and $2\,\mathrm{MHz/mm^2}$ (f).
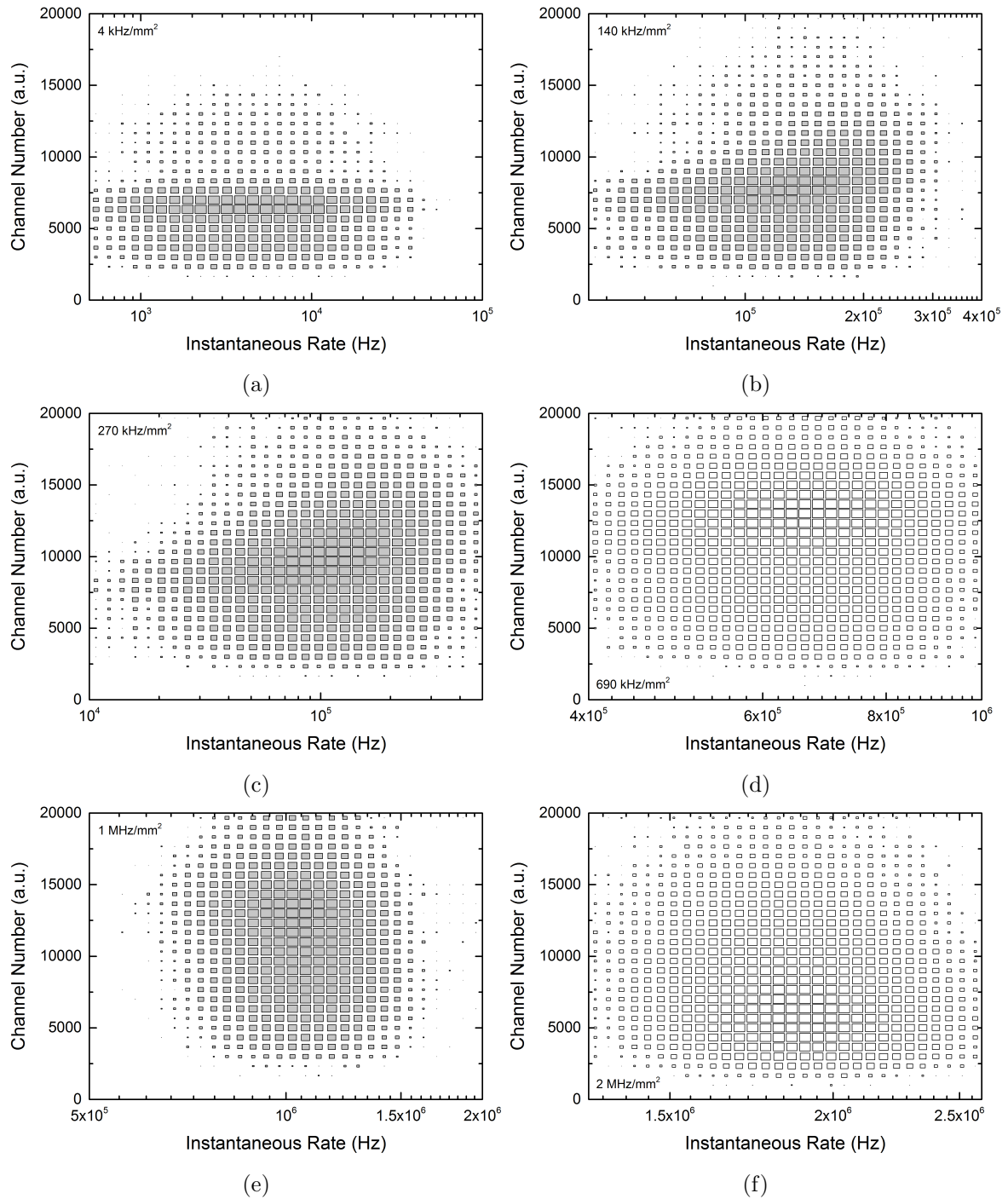
Figure A.5: Dependence of charge integral on the time to previous trigger. The plot shows a 2D histogram of the pulses acquired for figure A.4. The area of each rectangle represents the squared counts per bin and is normalized to the largest number of counts. The detector was operated at a *nominal* effective gain of 10×10^3. Plots were acquired for particle fluxes of $4 \, \text{kHz/mm}^2$ (a), $140 \, \text{kHz/mm}^2$ (b), $270 \, \text{kHz/mm}^2$ (c), $690 \, \text{kHz/mm}^2$ (d), $1 \, \text{MHz/mm}^2$ (e), and $2 \, \text{MHz/mm}^2$ (f).

Figure A.6: Dependence of the charge integral on the instantaneous rate. The plot shows a 2D histogram of the pulses acquired for figure A.4. The area of each rectangle represents the squared counts per bin and is normalized to the largest number of counts. The detector was operated at a *nominal* effective gain of 10×10^3. Plots were acquired for particle fluxes of $4\,\mathrm{kHz/mm^2}$ (a), $140\,\mathrm{kHz/mm^2}$ (b), $270\,\mathrm{kHz/mm^2}$ (c), $690\,\mathrm{kHz/mm^2}$ (d), $1\,\mathrm{MHz/mm^2}$ (e), and $2\,\mathrm{MHz/mm^2}$ (f).

Bibliography

[1] Fabio Sauli. Principles of operation of multiwire proportional and drift chambers. page 92 p, Geneva, 1977. CERN, CERN. CERN, Geneva, 1975 - 1976.

[2] F. Sauli. *Gaseous Radiation Detectors: Fundamentals and Applications.* Cambridge University Press, Cambridge, UK, first edition, 2014.

[3] G. F. Knoll. *Radiation Detection and Measurement.* John Wiley & Sons, Inc., Hoboken, NJ, USA, third edition, 2000.

[4] M. J. Berger et al. XCOM: Photon Cross Section Database (version 1.5). `http://physics.nist.gov/xcom`, 2000. Accessed: 2016-01-28.

[5] J. H. Hubbell and S. M. Seltzer. Tables of X-Ray Mass Attenuation Coefficients and Mass Energy-Absorption Coefficients from 1 keV to 20 MeV for Elements Z = 1 to 92 and 48 Additional Substances of Dosimetric Interest. `http://www.nist.gov/pml/data/xraycoef/`, 2009. Accessed: 2016-06-18.

[6] G. R. Gilmore. *Practical Gamma-ray Spectrometry.* John Wiley & Sons Ltd, Chichester, UK, second edition, 2008.

[7] F. Sauli. The gas electron multiplier (GEM): Operating principles and applications. *Nucl. Instr. Meth. A*, 805:2 – 24, 2016. Special Issue in memory of Glenn F. Knoll.

[8] S. Biagi. Magboltz - transport of electrons in gas mixtures. `http://cern.ch/magboltz`, 1995. Accessed: 2016-02-02.

[9] A. Deisting et al. Measurements of ion mobility in argon and neon based gas mixtures. *Nucl. Instr. Meth. A*, 2016.

[10] M. Suzuki and S. Kubota. Mechanism of proportional scintillation in argon, krypton and xenon. *Nuclear Instruments and Methods*, 164(1):197 – 199, 1979.

[11] G. Charpak et al. The use of multiwire proportional counters to select and localize charged particles. *Nuclear Instruments and Methods*, 62(3):262 – 268, 1968.

[12] The Nobel Prize in Physics 1992. `http://www.nobelprize.org/nobel_prizes/physics/laureates/1992/`. Accessed: 2016-03-02.

[13] F. Sauli and A. Sharma. Micropattern gaseous detectors. *Annual Review of Nuclear and Particle Science*, 49(1):341–388, 1999.

[14] A. Oed. Position-sensitive detector with microstrip anode for electron multiplication with gases. *Nucl. Instr. Meth. A*, 263(2–3):351 – 359, 1988.

[15] F. Sauli. GEM: A new concept for electron amplification in gas detectors. *Nucl. Instr. Meth. A*, 386(2–3):531 – 534, 1997.

[16] C. Altunbas et al. Construction, test and commissioning of the triple-GEM tracking detector for COMPASS. *Nucl. Instr. Meth. A*, 490(1–2):177 – 203, 2002.

[17] R. Bouclier et al. New observations with the gas electron multiplier (GEM). *Nucl. Instr. Meth. A*, 396(1–2):50 – 66, 1997.

[18] C. Büttner et al. Progress with the gas electron multiplier. *Nucl. Instr. Meth. A*, 409(1–3):79 – 83, 1998.

[19] Scalable Readout System (SRS). `https://espace.cern.ch/rd51-wg5/srs/default.aspx`. Accessed: 2016-02-23.

[20] Comsol multiphysics®. `http://www.comsol.com`. Accessed: 2016-02-22.

[21] S. Bachmann et al. Charge amplification and transfer processes in the gas electron multiplier. *Nucl. Instr. Meth. A*, 438(2–3):376 – 408, 1999.

[22] F. Sauli, L. Ropelewski, and P. Everaerts. Ion feedback suppression in time projection chambers. *Nucl. Instr. Meth. A*, 560(2):269–277, 2006.

[23] M. Abi Akl et al. Uniformity studies in large area triple-GEM based detectors. *Nucl. Instr. Meth. A*, pages –, 2016.

[24] J. Benlloch et al. Development of the gas electron multiplier (GEM). *IEEE Trans. Nucl. Sci.*, 45:234–243, 1998.

[25] A. Bressan et al. Beam tests of the gas electron multiplier. *Nucl. Instr. Meth. A*, 425(1–2):262 – 276, 1999.

[26] P. Everaerts. Rate capability and ion feedback in GEM-detectors. Master's thesis, Universiteit Gent, Ghent, (BE), 2006.

[27] A. Breskin et al. Ion-induced effects in GEM and GEM/MHSP gaseous photomultipliers for the UV and the visible spectral range. *Nucl. Instr. Meth. A*, 553(1–2):46 – 52, 2005. Fifth International Workshop on Ring Imaging Detectors.

[28] S. Lotze. *Ion backdrift minimisation in a GEM-based TPC readout*. PhD thesis, Technische Hochschule Aachen, Aachen, 2006.

[29] M. Ball, K. Eckstein, and T. Gunji. Ion backflow studies for the ALICE TPC upgrade with GEMs. *Journal of Instrumentation*, 9(04):C04025, 2014.

[30] N. Majumdar. Characterization of Triple-GEM in Argon-based Gas Mixtures. In *RD51 Mini Week*, June 2014.

[31] CAEN N1471H User's Manual. `http://www.caen.it/servlet/checkCaenManualFile?Id=11022`. Accessed: 2016-02-22.

[32] Keithley Model 6487 Picoammeter/Voltage Source data sheet. `http://www.tek.com/sites/tek.com/files/media/media/resources/6487.pdf`. Accessed: 2016-02-22.

[33] ORTEC® 142PC Preamplifier. `http://ortec-online.com/download/142PC.pdf`. Accessed: 2016-02-22.

[34] ORTEC® 672 Spectroscopy Amplifier. `http://ortec-online.com/download/672.pdf`. Accessed: 2016-02-22.

[35] AMPTEK MCA-8000D Specifications. `http://www.amptek.com/pdf/mca8000d.pdf`. Accessed: 2016-02-22.

[36] M. Alfonsi et al. Simulation of the dielectric charging-up effect in a GEM detector. *Nucl. Instr. Meth. A*, 671:6 – 9, 2012.

[37] S.F. Biagi. Monte carlo simulation of electron drift and diffusion in counting gases under the influence of electric and magnetic fields. *Nucl. Instr. Meth. A*, 421(1–2):234 – 240, 1999.

[38] Ö. Şahin, T. Z. Kowalski, and R. Veenhof. High-precision gas gain and energy transfer measurements in Ar–CO2 mixtures. *Nucl. Instr. Meth. A*, 768:104 – 111, 2014.

[39] H. W. Ellis et al. Transport properties of gaseous ions over a wide energy range. *Atom. Data and Nucl. Data Tables*, 17:177–210, 1976.

[40] F. Resnati. *Modeling, design and first operation of the novel double phase LAr LEM-TPC detector*. PhD thesis, Eidgenössische Technische Hochschule ETH Zürich, Zürich, 2012.

[41] Mini-Circuits® ZKL-1R5+ Amplifier data sheet. `http://www.minicircuits.com/pdfs/ZKL-1R5.pdf`. Accessed: 2016-02-23.

[42] LeCroy WaveRunner® Xi series oscilloscopes operator's manual. `http://cdn.teledynelecroy.com/files/manuals/wrxi_om_revc.pdf`. Accessed: 2016-02-22.

[43] G. Schultz, G. Charpak, and F. Sauli. Mobilities of positive ions in some gas mixtures used in proportional and drift chambers. *Rev. Phys. Appl.*, 12:67–70, 1977.

[44] A M F Trindade et al. Experimental study on ion mobility in Ar-CH$_4$ mixtures. *Journal of Instrumentation*, 9(06):P06003, 2014.

[45] John A. Hornbeck. The drift velocities of molecular and atomic ions in helium, neon, and argon. *Phys. Rev.*, 84:615–620, Nov 1951.

[46] A. Buzulutskov et al. Further studies of the GEM photomultiplier. *Nucl. Instr. Meth. A*, 442(1–3):68 – 73, 2000.

[47] Upgrade of the ALICE Time Projection Chamber. Technical Report CERN-LHCC-2013-020. ALICE-TDR-016, CERN, Geneva, Oct 2013.

[48] Addendum to the Technical Design Report for the Upgrade of the ALICE Time Projection Chamber. Technical Report CERN-LHCC-2015-002. ALICE-TDR-016-ADD-1, CERN, Geneva, Feb 2015.

[49] A. Bondar et al. Study of ion feedback in multi-GEM structures. *Nucl. Instr. Meth. A*, 496(2–3):325 – 332, 2003.

[50] D. Mörmann et al. Evaluation and reduction of ion back-flow in multi-GEM detectors. *Nucl. Instr. Meth. A*, 516(2–3):315 – 326, 2004.

[51] V. Berry. Impermeability of graphene and its applications. *Carbon*, 62:1 – 10, 2013.

[52] J. C. Meyer et al. The structure of suspended graphene sheets. *Nature*, 446(7131):60–63, 2007.

[53] J. C. Meyer et al. Imaging and dynamics of light atoms and molecules on graphene. *Nature*, 454(7202):319–322, Jul 2008.

[54] Z. Lee et al. Direct imaging of soft-hard interfaces enabled by graphene. *Nano Letters*, 9(9):3365–3369, 2009. PMID: 19591495.

[55] E. Mikmekova et al. Very low energy electron microscopy of graphene flakes. *Journal of Microscopy*, 251(2):123–127, 2013.

[56] R. M. Feenstra et al. Low-energy electron reflectivity from graphene. *Phys. Rev. B*, 87:041406, Jan 2013.

[57] S. Nie et al. Growth from below: bilayer graphene on copper by chemical vapor deposition. *New Journal of Physics*, 14(9):093028, 2012.

[58] J.-A. Yan et al. Time-domain simulation of electron diffraction in crystals. *Phys. Rev. B*, 84:224117, Dec 2011.

[59] J.-N. Longchamp et al. Low-energy electron transmission imaging of clusters on free-standing graphene. *Applied Physics Letters*, 101(11), 2012.

[60] J. Y. Mutus et al. Low-energy electron point projection microscopy of suspended graphene, the ultimate 'microscope slide'. *New Journal of Physics*, 13(6):063011, 2011.

[61] G. Hassink et al. Transparency of graphene for low-energy electrons measured in a vacuum-triode setup. *APL Mater.*, 3(7), 2015.

[62] F. Schedin et al. Detection of individual gas molecules adsorbed on graphene. *Nat Mater*, 6:652 – 655, 2007.

[63] A. Morin et al. FIB carving of nanopores into suspended graphene films. *Microelectronic Engineering*, 97:311 – 316, 2012. Micro- and Nano-Engineering (MNE) 2011, selected contributions: Part I.

[64] J. S. Bunch et al. Impermeable atomic membranes from graphene sheets. *Nano Lett.*, 8:2458 – 2462, 2008.

[65] K. S. Novoselov et al. Electric field effect in atomically thin carbon films. *Science*, 306(5696):666–669, 2004.

[66] A. K. Geim and K. S. Novoselov. The rise of graphene. *Nat Mater*, 6(3):183–191, Mar 2007.

[67] Jr. Hummers, W. S. and R. E. E. Offeman. Preparation of graphitic oxide. *Journal of the American Chemical Society*, 80(6):1339–1339, 1958.

[68] G. Wang et al. Facile synthesis and characterization of graphene nanosheets. *The Journal of Physical Chemistry C*, 112(22):8192–8195, 2008.

[69] S. Park et al. Colloidal suspensions of highly reduced graphene oxide in a wide variety of organic solvents. *Nano Letters*, 9(4):1593–1597, 2009. PMID: 19265429.

[70] V. C. Tung et al. High-throughput solution processing of large-scale graphene. *Nat Nano*, 4(1):25–29, Jan 2009.

[71] M. Lotya et al. Liquid phase production of graphene by exfoliation of graphite in surfactant/water solutions. *Journal of the American Chemical Society*, 131(10):3611–3620, 2009. PMID: 19227978.

[72] U. Khan et al. Solvent-exfoliated graphene at extremely high concentration. *Langmuir*, 27(15):9077–9082, 2011. PMID: 21675749.

[73] Z. G. Cambaz et al. Noncatalytic synthesis of carbon nanotubes, graphene and graphite on SiC. *Carbon*, 46(6):841 – 849, 2008.

[74] P. W. Sutter, J.-I. Flege, and E. A. Sutter. Epitaxial graphene on ruthenium. *Nat Mater*, 7(5):406–411, May 2008.

[75] Q. Yu et al. Graphene segregated on Ni surfaces and transferred to insulators. *Applied Physics Letters*, 93(11), 2008.

[76] X. Li et al. Large-area synthesis of high-quality and uniform graphene films on copper foils. *Science*, 324(5932):1312–1314, 2009.

[77] X. Li et al. Large-area graphene single crystals grown by low-pressure chemical vapor deposition of methane on copper. *Journal of the American Chemical Society*, 133(9):2816–2819, 2011. PMID: 21309560.

[78] M. Regmi, M. F. Chisholm, and G. Eres. The effect of growth parameters on the intrinsic properties of large-area single layer graphene grown by chemical vapor deposition on Cu. *Carbon*, 50(1):134 – 141, 2012.

[79] Y. Hao et al. The role of surface oxygen in the growth of large single-crystal graphene on copper. *Science*, 342(6159):720–723, 2013.

[80] B. Hu et al. Epitaxial growth of large-area single-layer graphene over Cu(1 1 1)/sapphire by atmospheric pressure CVD. *Carbon*, 50(1):57 – 65, 2012.

[81] L. Zhao et al. Influence of copper crystal surface on the CVD growth of large area monolayer graphene. *Solid State Communications*, 151(7):509 – 513, 2011.

[82] H. I. Rasool et al. Continuity of graphene on polycrystalline copper. *Nano Letters*, 11(1):251–256, 2011. PMID: 21117698.

[83] P. Kula et al. The growth of a polycrystalline graphene from a liquid phase. *Nanotech 2013*, 1:210–212, 2013.

[84] P. Kula et al. Method of producing graphene from liquid metal. U.S. Patent Application No. 2015/0122659 A1, issued May 7 2015.

[85] Graphenea Inc. `http://www.graphenea.com/`. Accessed: 2015-11-17.

[86] ACS Material, LLC. `http://www.acsmaterial.com/`. Accessed: 2015-11-17.

[87] Graphene Laboratories Inc. `http://graphene-supermarket.com/`. Accessed: 2015-11-17.

[88] Advanced Graphene Products Sp. z o.o. `http://advancedgrapheneproducts.com/`. Accessed: 2015-11-17.

[89] J. W. Suk et al. Transfer of CVD-Grown Monolayer Graphene onto Arbitrary Substrates. *ACS Nano*, 5(9):6916–6924, 2011. PMID: 21894965.

[90] K. S. Novoselov. private communication, 12 2013.

[91] H. J. Jeong et al. Improved transfer of chemical-vapor-deposited graphene through modification of intermolecular interactions and solubility of poly(methylmethacrylate) layers. *Carbon*, 66:612 – 618, 2014.

[92] T. J. Booth et al. Macroscopic graphene membranes and their extraordinary stiffness. *Nano Letters*, 8(8):2442–2446, 2008.

[93] P. Waduge et al. Programmed synthesis of freestanding graphene nanomembrane arrays. *Small*, 11(5):597–603, 2015.

[94] B. Alemán et al. Transfer-free batch fabrication of large-area suspended graphene membranes. *ACS Nano*, 4(8):4762–4768, 2010. PMID: 20604526.

[95] A. Fasolino, J. H. Los, and M. I. Katsnelson. Intrinsic ripples in graphene. *Nat Mater*, 6(11):858 – 861, 2007.

[96] Y. Liu and B. I. Yakobson. Cones, pringles, and grain boundary landscapes in graphene topology. *Nano Lett.*, 10(6):2178 – 2183, 2010.

[97] J. Guo et al. Topological defects: Origin of nanopores and enhanced adsorption performance in nanoporous carbon. *Small*, 8(21):3283–3288, 2012.

[98] T. Nguyen et al. Large-area transfer of suspended monolayer, bilayer, and trilayer graphene with high coverage. *ACS Nano*, submitted.

[99] A. C. Ferrari et al. Raman spectrum of graphene and graphene layers. *Physical Review Letters*, 97(18):0, 2006.

[100] M. A. Pimenta et al. Studying disorder in graphite-based systems by Raman spectroscopy. *Phys. Chem. Chem. Phys.*, 9:1276–1290, 2007.

[101] Y. Hao et al. Probing layer number and stacking order of few-layer graphene by Raman spectroscopy. *Small*, 6(2):195–200, 2010.

[102] A. Gupta et al. Raman Scattering from High-Frequency Phonons in Supported n-Graphene Layer Films. *Nano Letters*, 6(12):2667–2673, 2006. PMID: 17163685.

[103] CAEN N1470 User's Manual. `http://www.caen.it/servlet/checkCaenManualFile?Id=11016`. Accessed: 2016-02-22.

[104] CAEN NDT14xx User's Manual. `http://www.caen.it/servlet/checkCaenManualFile?Id=11289`. Accessed: 2016-02-22.

[105] ORTEC® 474 Timing Filter Amplifier. `http://ortec-online.com/download/474.pdf`. Accessed: 2016-02-22.

Acknowledgements

There are a lot people without whom this work would not have been possible.

First I would like to thank you, *Christina Streli*, for accepting me as your doctoral student and supervising my thesis. Thank you for helping me handling my work at CERN while pursuing my studies in Vienna.

I am especially thankful to you, *Leszek Ropelewski*, for giving me the opportunity of working in your group and supervising my thesis at CERN. Thank you for your guidance during the last years, for the possibilities to present my work all over the world and, most importantly, for your help when I was stuck with a really difficult problem.

I am also very thankful to you, *Werner Riegler*, for agreeing to both assess my thesis and join the examination committee at my doctoral defense. Thank you, *João Veloso*, for taking up the task of assessing my thesis - on a very short notice - and also to you, *Fabio Sauli*, for being part of the examination committee - on even much shorter notice. Thank you very much.

I want to thank you, *Eraldo Oliveri* and *Filippo Resnati*, for teaching me everything I know about gaseous detectors, and especially for helping and supporting me each day and also every other night. I am very grateful for what the two of you have contributed to the success of this thesis.

I would also like to thank my many other colleagues who work and worked in the Gaseous Detector Development facilities at CERN:

I am most thankful to you, *Alejandro Puig-Barañac* and *Jérémie Merlin*, whom I call my dearest friends, for all the time I could enjoy working with you - at CERN - and especially the times when we were desperately trying to forget about all the tasks still ahead of us - which happened everywhere else.
Thank you, *Dorothea Pfeiffer*, for your support, for cheering me up when it was needed and generally for sharing the office with me. I am more than happy that our journey goes on for another few years. The same is true for you, *Silvia Franchino*, *Brian Dorney*, *Ourania Sidiropoulou*, *Florian Brunbauer* and *Michael Lupberger*, and also to you I am thankful for everything you have done so far.
Special thanks go to you, *Miranda van Stenis*, because you never got tired of answering "just a question" and manufacturing almost every part I had to use during the last three years.
A big thank you also to you, *Rui de Oliveira*, and your team at the MPT workshop for the

Curriculum Vitae

Personal data		Address
Name:	Patrik Thuiner	247, Rue Lucie Aubrac
Date of Birth:	10.01.1985	F-01630 Saint-Genis-Pouilly
Nationality:	Austrian	patrik@thuiner.at

Education

08/2012 - 11/2016	**Doctoral programme in Technical Sciences**, Specialisation: Technical Physics, *Technische Universität Wien, Wien, Austria* Doctoral thesis "Ion space-charge effects in multi-GEM detectors: challenges and possible solutions for future applications"
10/2005 - 06/2012	**Bachelor / Master studies in technical physics**, Specialisation: Applied physics, *Technische Universität Wien, Wien, Austria*. Master thesis "Development and validation of software for the measurement of gamma rays"
10/2009 - 01/2010	**Erasmus programme**, *Univerzita Pavla Jozefa Šafárika v Košiciach, Prírodovedecká fakulta, Košice, Slovakia*
09/1995 - 06/2004	**High school diploma**, *HTBL Hollabrunn, Hollabrunn, Austria*. Technical high school for business engineering, specialisation in business informatics

Work experience

02/2016 - ongoing	**CERN fellow**, *CERN, Genève, Switzerland*. Detector R&D for the NMX macromolecular diffractometer at the European Spallation Source (ESS), Lund, Sweden
02/2013 - 01/2016	**CERN doctoral student**, *CERN, Genève, Switzerland* Doctoral thesis "Ion space-charge effects in multi-GEM detectors: challenges and possible solutions for future applications"
06/2011 - 01/2012	**Seibersdorf Labor GmbH**, *Seibersdorf, Austria*. Master thesis "Development and validation of software for the measurement of gamma rays"
05/2009 - 05/2012	**ARGE Physikmobil**, *Wien, Austria*. Science communications
10/2007 - 02/2012	**Technische Universität Wien**, *Wien, Austria*. Tutor / Teaching Assistant
10/2008	**Austrian Research Centers GmbH - ARC**, *Seibersdorf, Austria*. Software development
07/2008	**Austrian Research Centers GmbH - ARC**, *Seibersdorf, Austria*. Software development